The Pennsylvania State University

The Graduate School

College of Earth and Mineral Sciences

ELECTROMECHANICAL CHARACTERIZATION OF LEAD MAGNESIUM

NIOBATE BASED THIN FILMS

A Dissertation in

Materials Science and Engineering

by

Smitha Shetty

Submitted in Partial Fulfillment
of the Requirements
for the Degree of

Doctor of Philosophy

May 2019

The dissertation of Smitha Shetty was reviewed and approved* by the following:

Susan Trolier-McKinstry
Professor of Ceramic Science and Engineering and Electrical Engineering
Dissertation Adviser
Chair of Committee

Clive A. Randall
Professor of Materials Science and Engineering

Venkatraman Gopalan
Professor, Materials Science and Engineering and Engineering Science and
Mechanics

Chris Giebink
Assistant Professor of Electrical Engineering

Tom Shaw
IBM
Special Member

Suzanne Mohney
Professor of Materials Science and Engineering and Electrical Engineering Chair,
Intercollege Graduate Degree Program in Materials Science and Engineering

*Signatures are on file in the Graduate School

ABSTRACT

Lead Magnesium Niobate (PMN) is the most studied relaxor ferroelectric compound with cation order intimately interacting with nanoscale polar heterogeneities. In undoped bulk PMN, the cation order can hardly be changed, while the polar order is quite responsive to external stimuli (electric field and temperature). Moreover, PMN-based oxides are of technological importance, displaying strong piezoelectric effects, high electrostrictive strains, and unusually high dielectric permittivity. The local compositional heterogeneity associated with short-range ordering of Mg and Nb in $PbMg_{1/3}Nb_{2/3}O_3$ (PMN) is correlated with its characteristic relaxor ferroelectric behavior. Fully-ordered PMN has not been prepared as a bulk material.

This work reports the growth and characterization of thin film PMN heterostructures with long-range cation order. These films were grown at temperatures below 1073 K by artificially reducing the degree of disorder via synthesis of heterostructures with alternate layers of $Pb(Mg_{2/3}Nb_{1/3})O_3$ and $PbNbO_3$, as suggested by the random-site model. 100-nm-thick, phase-pure films were grown epitaxially on (111) $SrTiO_3$ substrates using alternate target timed pulsed-laser deposition of $Pb(Mg_{2/3}Nb_{1/3})O_3$ and $PbNbO_3$ targets with 20% excess Pb. Selected area electron diffraction confirmed the emergence of (1/2, 1/2, 1/2) superlattice spots with randomly distributed ordered domains as large as ~150 nm. These heterostructures exhibited a dielectric constant of 800, loss tangents of ~0.03 and 2 x remanent polarization of ~11 $\mu C/cm^2$ at room temperature. Polarization-electric field hysteresis loops, Rayleigh data, and optical second-harmonic generation measurements are consistent with the development of ferroelectric domains below 140 K. Temperature-dependent permittivity measurements demonstrate reduced frequency dispersion compared to short range ordered PMN films. Although perfectly layered heterostructures could not be grown, the novelty of this work lies in achieving the highest cation order in PMN. Further, these engineered films exhibit a continuum between normal and relaxor ferroelectric behavior as a

function of temperature.

The dynamic nonlinear dielectric responses were also studied as a function of temperature and electric field for the PMN thin films with long- and short-range ordering. It was found that long-range ordering decreased the dispersion in the first and third harmonic displacement current relative to short-range ordered films. For both sets of films, a second harmonic component of the dielectric response was also detected. The phase angles of the higher harmonic responses were used to probe the continuum in ferroelectric- relaxor behavior in these films. At high temperatures (e.g. above the freezing temperature), the presence of nanopolar clusters is believed to cause the strong dispersion in the third harmonic response in both long range and short-range films. However, at lower temperatures, changes in the sign of χ_3 suggest long-range ferroelectric ordering, such that the response of mobile interfaces (believed to be domain walls) dominate the response.

Additionally, miniaturization of PMN based ferroelectric films for actuator applications necessitates quantification of piezoelectric properties with scaling. A single beam laser interferometer based on a modified Mirau detection scheme with a vertical resolution of $\sim 5\,\text{pm}$ was developed for localized d_{33} measurements on patterned piezoelectric films. The tool provides high spatial resolution ($\sim 2\,\mu\text{m}$), essential for understanding scaling and processing effects in piezoelectric materials. This approach enables quantitative information on d_{33}, currently difficult in local measurement techniques such as piezoresponse force microscopy. The interferometer is built in a custom microscope and employs a phase lock-in technique in order to detect sub-Angstrom displacements. d_{33} measurements on single crystal $0.67\text{PbMg}_{0.33}\text{Nb}_{0.67}\text{O}_3$-$0.33\text{PbTiO}_3$ and bulk PbZrTiO_3-5A ceramics demonstrated agreement within $<3\%$ with measurements using a double beam laser interferometer. Substrate bending contributions to out-of-plane strain, observed in thin continuous $\text{PbZr}_{0.52}\text{Ti}_{0.48}\text{O}_3$ films grown on Si substrates is reduced for electrode diameters smaller than $100\,\mu\text{m}$. Direct scanning across $5\,\mu\text{m}$ and $10\,\mu\text{m}$

features etched in $0.5\,\mu$m thick $PbZr_{0.52}Ti_{0.48}O_3$ films doped with 1% Nb poled at either room temperature or 150 °C confirmed minimal substrate contributions to the effective $d_{33,f}$. Furthermore, enhanced $d_{33,f}$ values were observed along the feature edges due to partial declamping from the substrate, thus validating the application of single beam interferometry on finely patterned electrodes.

TABLE OF CONTENTS

LIST OF FIGURES

LIST OF TABLES

ACKNOWLEDGEMENTS

acknowledge the help of Beth Jones and Jeff Long in target preparation and electrical characterization setup.

On the personal front, I want to acknowledge the hard work and sacrifice on the part of my loving family. My mom has always been my biggest pillar of strength and wisdom. Last but not the least, I want to thank my two-year-old toddler Romila, for her love to get me through the writing phase of this dissertation.

Chapter 1

Introduction and thesis organization

1.1 Introduction

Ferroelectric oxide films are becoming increasingly attractive in micro- and nano-scale sensing and actuating applications relative to their electrostatic or electrothermal counterparts due to their low power requirements, large displacements, fast responses, and linear operating regimes[1]. Relaxors are a special variant of the ferroelectric material family, with characteristic structural and polar inhomogeneities at the nanoscale level that enable their unusual electromechanical properties[2–4]. This class of materials finds applications in capacitors, energy-storage devices, electrostrictive actuators used in non-linear optics, etc.[2,5,6]. Despite their widespread applications, the origin of these extraordinary characteristics is incompletely understood. This limits the design and exploration of new relaxor based materials. With increasing need for miniaturization of devices and availability of advanced material synthesis tools like molecular beam epitaxy, the fundamental structure-property relationships in this technologically important family of materials should be further studied and exploited.

The complex perovskite lead magnesium niobate ($PbMg_{1/3}Nb_{2/3}O_3$), PMN is a model relaxor ferroelectric. PMN is interesting from a fundamental point of view since there exists a nanoscale short range ordering of Mg^{2+} and Nb^{5+} ions in bulk ceramics, which remains unchanged by any reported annealing processes[7]. There are several open-ended questions about the origin of dielectric dispersion as a function of temperature in PMN and its relationship to the prevalent short-range ordering. The present work investigates the impact of B-site ordering on the

dispersion and non-linear dielectric properties of PMN thin films. Experimental study of the non-linear properties of relaxor can be helpful to understand the behavior of PMN at low temperatures-if the material diverges into a glassy state or becomes more "ferroelectric" with increased ordering.

Additionally, it is also imperative to understand how these physical properties evolve with lateral scaling in PMN-based piezoelectric thin films. This can have a significant impact in the development of the piezoelectronic transistor (PET)[8,9]- a post-CMOS technology, proposed to overcome the saturation of clock speeds (~ 2 GHz) with device scaling. The PET as shown in Figure 1-1 is a low power and fast switching device in which piezoelectric and piezoresistive materials are stacked within a stiff shell. Electric field applied across the piezoelectric layer (between common and gate electrodes) actuates the piezoresistor and induces a continuous insulator-to-metal transition. This causes the switch to turn on, enabling current to flow from the common to the sense electrode. In order to enable power savings relative to CMOS technology, the bulk, unclamped piezoelectric properties are needed[10]. The challenge is that there is currently a lack of high spatial resolution metrology enabling accurate measurement of piezoelectric $d_{33,f}$ in thin films. This work includes the development of a quantitative single beam laser interferometry-based microscopy for thin films that enables piezoelectric measurements at the micron length scale.
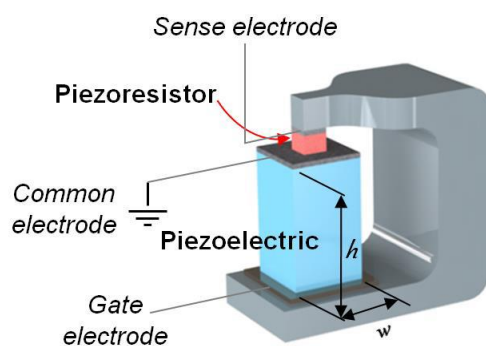
Figure 1-1 Schematic of piezoelectronic transistor proposed by IBM[11]

1.2 Thesis Organization

This thesis is primarily divided into two sections: 1. Relaxor behavior and nonlinearity in engineered PMN heterostructures and 2. Evolution of piezoelectric properties in PZT and PMN-PT thin films as a function of lateral scaling.

Chapter 2 provides a review of relevant background literature. First, a brief introduction to relaxor ferroelectricity, in comparison with normal ferroelectricity, is provided. Second, several models proposed in the literature to explain dielectric dispersion are reviewed. Next, Rayleigh analysis is discussed in detail to probe the relaxor-ferroelectric continuum in engineered films. Finally, the role of substrate clamping is discussed in thin films, with emphasis on evolution of piezoelectric properties in perovskite films.

Chapter 3 discusses the growth and structural characterization of long-range-ordered PMN heterostructures as per the random-site model using timed pulsed laser deposition technique. Selected area electron diffraction as well as dark field imaging of the superlattice spots are presented in comparison with short-range-ordered films. Relationships between the ordering and the ferroelectric/ relaxor properties were examined as a function of temperature via electrical characterization and second harmonic generation measurements. Parts of this chapter have been published in Advanced Functional Materials[12]. Chapter 4 studies the impact of ordering on the nonlinearity in PMN thin films. This includes the analysis of third harmonic susceptibility as a function of function of temperature, electric field and frequency. This data further corroborates the co-existence of relaxor and ferroelectric behavior in long-range-ordered PMN films.

Chapter 5 includes the design and development of spatially resolved single beam laser interferometer and piezoelectric d_{33} characterization on bulk and thin film. This chapter also validates the use of single beam interferometry for d_{33} quantification on partially declamped structures etched in PZT thin films. Parts of this chapter have been published in the Journal of

Applied Physics[13].

      Chapter 6 summarizes the primary contributions from this work and discusses possible future work on the impact of cation ordering in relaxor ferroelectrics on flexoelectricity.

Chapter 2

Literature Review

2.1 Introduction to lead magnesium niobate (PMN) and relaxor ferroelectricity

In 1958, Smolensky et al. discovered unusual dielectric properties in a complex perovskite material, namely lead magnesium niobate $Pb(Mg_{1/3}Nb_{2/3})O_3$, or PMN[14]; materials in this family were later termed relaxor ferroelectrics[15–18]. Relaxor ferroelectrics differ from normal ferroelectrics in several ways, as summarized in Figure 0-1. They demonstrate broad dielectric dispersion below the maximum in permittivity as a function of temperature (T_{max}), followed by collapse of that dispersion at higher temperatures. Other differences[4,19] include: (1) relaxors have slim hysteresis loops just below dielectric maximum T_{max}; (2) they exhibit some switchable polarization above T_{max}; (3) relaxors show no evidence of structural macroscopic symmetry breaking at T_{max} and no spontaneous polarization just below T_{max} - in contrast, in normal ferroelectrics, T_{max} occurs at the Curie temperature, below which the material exhibits a stable, spontaneous reorientable polarization; (4) relaxors do not show sudden anomalies in properties such as birefringence, index of refraction, or volume at T_{max}; (5) relaxor ferroelectrics also show a large deviation from Curie–Weiss behavior in the dielectric permittivity above T_{max}. At much higher temperatures, however, the inverse permittivity does follow Curie–Weiss behavior. The temperature at which there is a departure from Curie–Weiss behavior is termed the Burns temperature. In the temperature range, $T_{max} < T < T_{Burns}$, the dielectric response is sometimes described with a $(T–\theta)^\gamma$ relationship, where the parameter γ ($1 < \gamma < 2$), can be empirically determined, but no single value uniquely describes the dependence.

Normal Ferroelectric		Relaxors
• Macro-size FE domains	(a)	• Nano-size polar domains
• No polar domains above T_c	(b)	• Nano-size polar domains persist well above T_m
•sharp narrow transitions •$\varepsilon'(T)$ follows Curie-Weiss law •No frequency dispersion	(c)	• very broad $\varepsilon'(T)$ peaks • strong deviation from Curie-Weiss law • strong frequency dispersion
• 1st - or 2nd - order phase transition with macroscopic symmetry change at T_c • Strong optical anisotropy across T_c		• No structural phase transition across T_m • Critical slowing down of dipolar motion below T_m • No optical anisotropy across T_m

Figure 0-2: Comparison between normal and relaxor ferroelectrics[19].

Bulk Lead magnesium niobate ($PbMg_{1/3}Nb_{2/3}O_3$) is known for its exceptional dielectric (exceeding 12,000 at room temperature and 100 Hz) and electrostrictive properties, and is valued for use in the actuators employed to control the corrector mirror tip and tilt in the Hubble telescope[3,14]. Furthermore, domain engineered PMN relaxor-$PbTiO_3$ single crystals possess strong piezoelectricity ($d_{33} > 2000$ pC/N) and electromechanical coupling coefficients ($k_{33} > 0.9$)[20]. Recent work by Li *et al.*[21,22] demonstrated that up to 80% of these exceptional properties are due to the alignment and rotation of nanoscale inhomogeneities, known as polar nanoregions (PNRs), which are found in relaxors and arise due to intermediate range cation order. However, the exact role of cation order in PMN has been the subject of considerable debate. The compositional heterogeneity associated with the lack of long-range ordering of the *B* cation sites in $Pb(B_{1/3}B'_{2/3})O_3$ is correlated with its characteristic relaxor behavior[4,15,23]. From a structural point of view, the average symmetry of PMN, when probed by conventional X-ray or neutron diffraction, appears to be cubic (*Pm3m*) down to 5K in zero field[24–26] with no evidence of a macroscopic structural-phase transition taking place through or below the temperature of maximum permittivity (T_{max} = 265 K, at 1 kHz). However, diffuse scattering about the Bragg peaks has been observed below the Burns temperature T_d (or T_B) $\approx$ 620 K, indicating the presence of local PNR with rhombohedral *R3m* symmetry dispersed in a non-polar matrix. The volume fraction of PNRs is reported to increase upon cooling to reach about 25 vol% at 5 K[4]. Such an evolution of ergodic local structure is in agreement with deviations from linearity of the temperature dependence of the refractive index, the lattice parameters, the thermal expansion, and the deviation of the dielectric permittivity from the Curie-Weiss law below T_d[15]. The mechanism responsible for dispersion in the relative permittivity is yet to be understood completely, though it is widely attributed to the dynamics of the PNRs. The size of the PNRs in bulk PMN has been found to increase near a characteristic freezing temperature T_f (220 K), below which the material freezes into a static "glassy" state (a pseudocubic non-ergodic state with isotropic properties) without long-range polar order in the absence of an electric field.

However, it has been reported that a dc electric field (>$E_{critical}$ = 1.7 kV/cm) can induce a ferroelectric transition from the glassy state in field-cooled[27,28] bulk PMN. In the same way, application of a dc bias field induces long range ferroelectric order in a zero-field-cooled sample, at 200 K, albeit in a longer time[29]. The corresponding electric field – temperature phase diagram for (111)-oriented field cooled PMN single crystals is illustrated in Figure 2-2. Once formed after field cooling at E> $E_{critical}$, the ferroelectric phase is stable, without field, up to a critical temperature ~213 K (indicated by the arrow in Figure 0-3). The properties of zero-field cooled (ZFC) PMN, including the phase diagram, are sample history dependent. This is an important characteristic of relaxors which distinguishes them from typical dipole glasses.
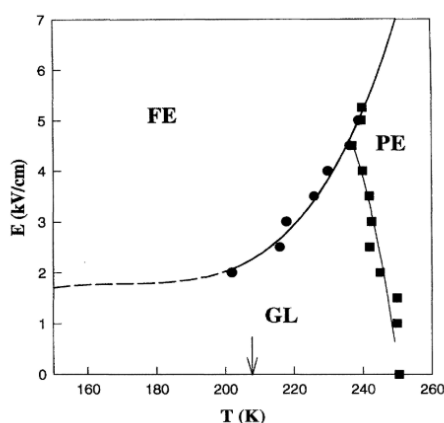
Figure 0-4: Electric-field —temperature phase diagram for PMN obtained in the FC regime (E parallel to <111>[29]) where FE: ferroelectric phase, GL: glassy phase and PE: paraelectric phase in PMN.

Several models have been proposed to explain relaxor phenomena: the compositional fluctuation model by Smolensky[14], super-paraelectric[3], dipolar glass[30,31], domain-like interface breathing[17,32,33], random-field[34], spherical-random-field, random-bond models[35], etc. Early works on relaxors (e.g. the composition fluctuations model by Smolensky and the super- paraelectric model by Cross) considered the PNRs to act as non-interacting entities, independent of each other. Smolensky's[14] model attributed the diffusiveness of the dielectric peak to the compositional

disorder inherent in PMN (spatial fluctuations of the Mg^{2+} and Nb^{5+} ion concentrations). Upon cooling, the local ferroelectric phase transitions occur in regions with higher Curie temperature, with the remaining regions in the paraelectric phase. However, the compositional disorder model does not describe the frequency dispersion of the dielectric permittivity. Cross's superparaelectric model[15] considered the PNRs to be local regions with rhombohedral distortion, having polarization fluctuations/reorientations among equivalent <111> with anisotropic activation energies comparable to k_bT at high temperature (where k_b is Boltzmann's constant and T is temperature). A distribution of the polar region volume directly implies a distribution of relaxation times. As the temperature decreases, the frequency of the fluctuations also decreases, leading the observed dispersion in the permittivity response. Thus, the dispersive behavior of the low-field permittivity could originate from a difference in the residence times of various polar orientations. Since the super-paraelectric model assumes no interaction between the local polar nanoregions, the frequency dependence T_{max} should be governed by a simple Debye relationship. However, fitting the Debye equation to the dielectric maxima yields physically unrealistic values for thermally activated polarization fluctuations (7 eV and 10^{40} s^{-1} for the activation energy and pre-exponential factor)[30].

Furthermore, relaxors are characterized by the presence of compositionally-ordered regions (CORs) with short ordering lengths[36], as summarized in Figure 0-5.   In contrast to PNRs, however, the morphology of CORs (their dimensions and the degree of compositional order) differs in different material systems with varying *B* site cations. Setter *et al*.[23] demonstrated that long-range ordering could be achieved in $PbSc_{1/2}Ta_{1/2}O_3$ (PST) ceramics (1:1 Sc:Ta order) by annealing at 1273 K for 24 hrs. Well-ordered samples showed a normal ferroelectric transition, while short-range-ordered samples were relaxor ferroelectrics, as shown in Figure 0-6. TEM analysis by Randall *et al*.[37] confirmed the increase in size of CORs from 2 nm in disordered as-sintered samples to ~200 nm in fully-ordered ceramics. A fully-ordered state has not been achieved in PMN bulk ceramics or crystals. Long range 1:1 ordered domains have been coarsened in either $PbMg_{1/3}Ta_{2/3}O_3$

or doped-PMN ceramics, via heat treatments in the range of 1523-1623 K[38–41]. However, it was found that the ordering length in PMN was restricted to 2-6 nm, irrespective of extended thermal annealing times. Akbas *et al.*[42,43] proposed that PMN undergoes a thermodynamic order-to-disorder transition at temperatures below 1073 K. Thus, the short-range ordering in PMN may be a quenched representation of the high-temperature, disordered phase. This low ordering temperature kinetically restricts the development of the thermodynamically-stable, ordered phase as the material is cooled. Compared to $PbMg_{1/3}Ta_{2/3}O_3$ (where $T_{disorder} = 1648$ K), the lower transition temperature for PMN was attributed to higher covalency/polarizability of Nb^{5+} compared to Ta^{5+}, and hence a reduced Coulombic driving force for order.
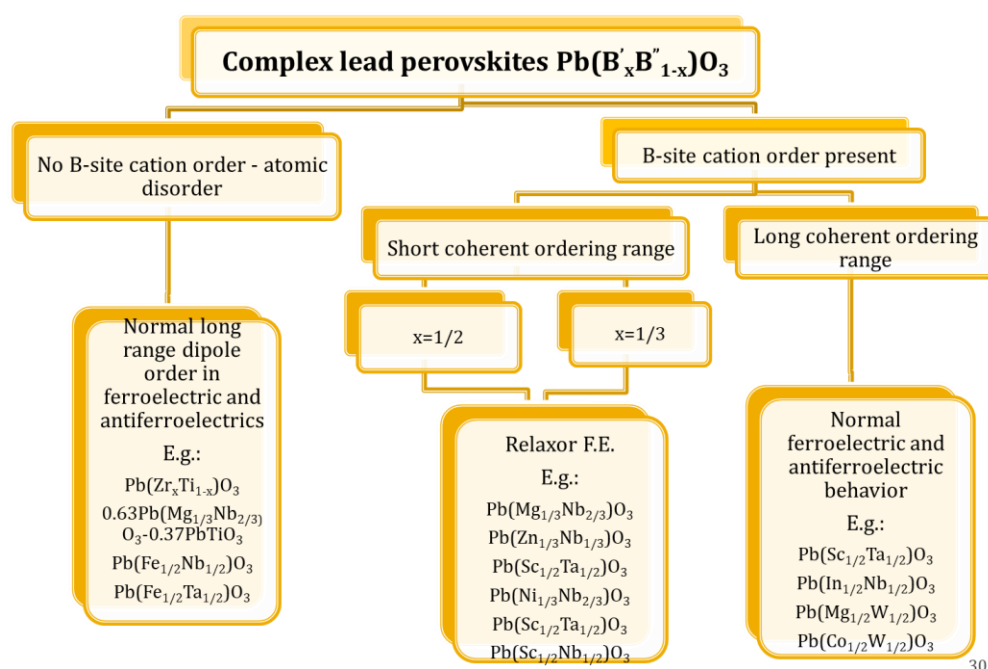
Figure 0-7: Classification of complex lead based perovskites on the basis of B-site ordering and dielectric behavior[36].
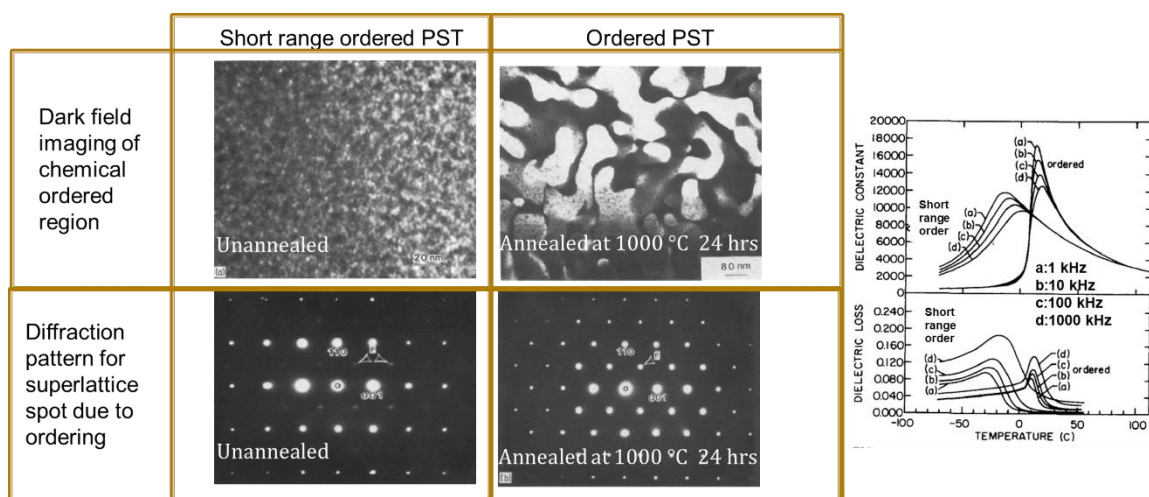
Figure 0-8: Influence of long range ordering in PST obtained after annealing on (a) size of chemically ordered regions and (b) dielectric behavior[37,44].

Akbas and Davies[43] interpreted the short-range ordering using the charge-balanced "random-site" model.[45] This model suggests stacking of two sublattices in the CORs (Pbβ'β''O_3) along [111]; the β''sublattice (which contains only Nb^{5+}) alternates with the β' plane (a 2:1 random mixture of Mg^{2+} and Nb^{5+}cations) for charge balance. This gives rise to doubling of the unit-cell size and an *Fm3m* space group inside the CORs. The net 1:2 Mg:Nb ratio in the CORs proposed by this model was experimentally confirmed by atomic resolution Z contrast imaging[46], and X-ray energy dispersive spectroscopy[47].

However, unlike PST, dielectric measurements showed the retention of relaxor behavior in thermally-coarsened domains in PbMg$_{1/3}$Ta$_{2/3}$O$_3$ and doped PMN. Two possible mechanisms can explain this anomaly: "random" fields[17,48] arising from chemical disorder either by charged defects like lead and oxygen vacancies and/or inherent disorder existing on the β' sublattice of the random-site model. Chu *et al.*[44,49] demonstrated a spontaneous relaxor to normal transition in *stoichiometric* short range ordered PST samples, while similar samples with < 3.5% lead vacancies retained relaxor characteristics. It is believed that the lead vacancies frustrate cooperative displacements of

the sublattices. Interestingly, the CORs in short range ordered-PST samples with lead vacancies (<

3.5%) were larger than those in stoichiometric samples. This work suggests the possibility that PbO

loss during long ordering anneals at 1473-1673 K in $PbMg_{1/3}Ta_{2/3}O_3$ or doped PMN can promote

relaxor behavior, despite simultaneous coarsening of the CORs. Alternately, it can be hypothesized

that the relaxor characteristics can be correlated to the atomic disorder[42] introduced by the random

distribution of the Mg^{2+} and Ta^{5+}/Nb^{5+} ions on the β' lattice in the CORs in PMT/PMN systems.

Chen *et al.*[44,50] modelled the influence of the size of *B*-site cations (Mg vs. Nb) on the β' sublattice

on strengthening the long range order – ferroelectric coupling. 1:1 order in adjacent sublattices was

reported to promote increased long-range coupling in the lattice, facilitating a relaxor-to-

ferroelectric transition due to increased displacement of the Pb^{2+} ion along the <111> towards the

β' position[42]. This implies that relaxor behavior may persist even in *stoichiometric* $Pb(B_{1/3}B'_{2/3})O_3$

systems. There is a lack of experimental evidence to support the above assertion since fully-

ordered, stoichiometric PMN-type materials have not been grown as bulk ceramics, though varying

degrees of cation order have been achieved in a narrow window of kinetic activity and

thermodynamic stability.

In addition, the relation between the PNRs, CORs, and the freezing of the PNRs leading to

the non-ergodic phase in PMN is not clearly understood. At high temperature, the PNR clusters are

small and non-interacting; however, on cooling below T_B, they can correlate with the neighboring

clusters and grow in size (as controlled by the correlation length). Drawing an analogy with spin

glasses, Viehland[30,51] demonstrated that the frequency dependence of the dielectric data could be

fit with the Vogel-Fulcher relationship using a temperature-dependent correlation activation energy

among PNR clusters, followed by freezing at T_f given by the following relationship:

$$f = f_0 \exp\left(\frac{E_a}{k(T_m - T_f)}\right) \qquad\qquad \text{Equation 0-1}$$

In Equation 0-2, E_a represents the activation energy for polarization fluctuations of an isolated cluster. The temperature dependence of the equation can be attributed to the development of short range order between neighboring clusters, with an interaction energy of kT_f. The physical model suggests that the polar clusters have a random distribution of polar orientations, similar to the magnetization in spin glasses. When cooled, the polar clusters form a preferred polar orientation, due to long-range interactions between the polar clusters. However, long-range ordering is suppressed by the frustrated interactions during the freezing process, suggesting that clusters could interact elastically through the rhombohedral distortion. The development of correlation between these super-paraelectric moments leads to freezing at T_f, which is close to the plateau temperature of correlation lengths, obtained via neutron scattering of PMN as shown in Figure 0-9 [5]. A long-range ordered ferroelectric state can be achieved if these clusters percolate (spontaneously[44] or under an applied electric field[28]). Burton's theoretical work using molecular dynamics based on first principles[52] in both PST and PMN proposed that the CORs act as nucleation centers for the PNRs. Local fields due to chemical disorder in the paraelectric matrix pin the PNRs from extending into the matrix, impeding the correlation between PNR clusters and leading to the glassy state in PMN as shown in Figure 0-10. This could potentially imply that a completely-ordered matrix with minor defects in PMN could suppress the formation of PNRs or, at the very least, enable a spontaneous relaxor-to-normal-ferroelectric transition. Inelastic neutron scattering techniques[53] have demonstrated dampening of the transverse optic mode, a so-called waterfall effect, when the material is cooled below T_d. However, there is recovery of the TO mode at temperatures around 213 K. Though this ordering is not visible via X-ray measurements, nonlinear dielectric spectroscopy suggests a ferroelectric transition for field cooled PMN.
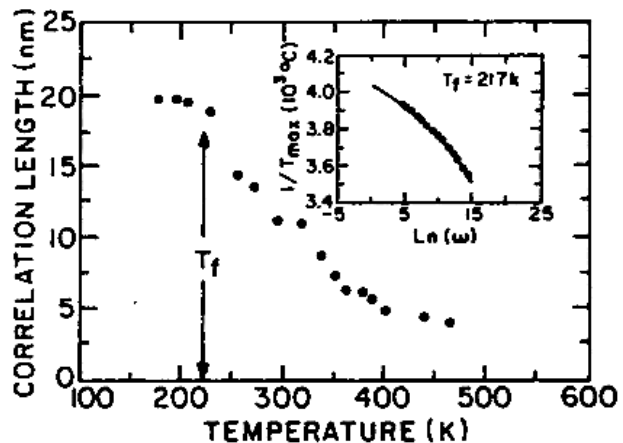
Figure 0-11: Temperature dependence of correlation lengths from neutron scattering of PMN at T_f with insert showing fitting to Vogel Fulcher, indicating glassy behavior[5].
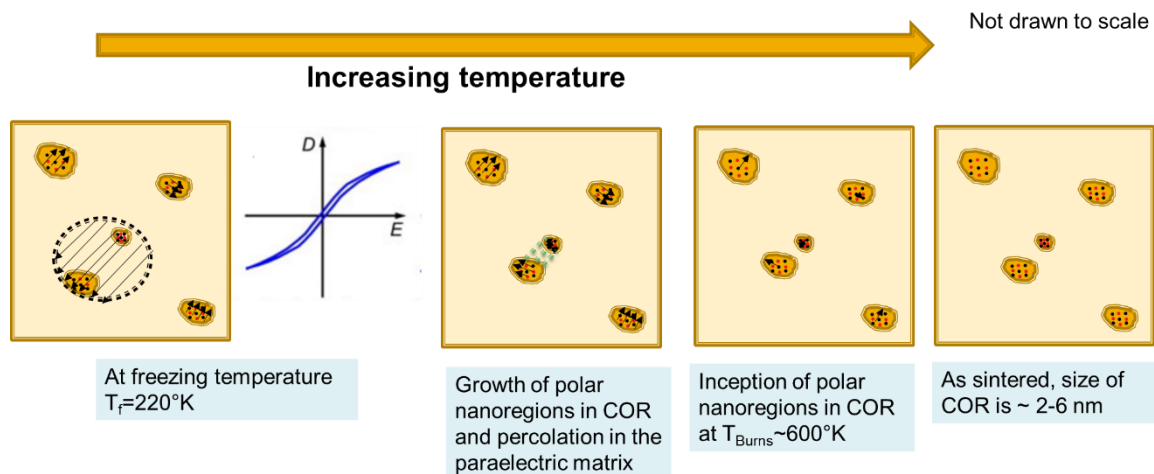
Figure 0-12: Schematic showing nucleation, growth and interaction of polar nanoregions in COR regions in a paraelectric matrix as a function of temperature.

Alternative microscopic models have been proposed to explain the key characteristics of PMN. Originally proposed by Isupov, the breathing wall model by Glazounov and Tagantsev[32,54] considers the polar cluster to be stabilized in orientation, but with interphase boundaries and domain wall-like entities, that are responsive to temperature and electric fields. The observed relaxor behavior of a single polar region is associated with the oscillation and movement of the

mobile walls due to an ac electric field, rather than thermally activated flips of local polarization. This model is capable of describing the frequency dependence of the first and third harmonics of PMN[55]. However, this model ignores the percolation of the interacting polar clusters through the material. Westphal, Kleemann and Glinchuk[17] proposed the "random field model", suggesting that the origin of the slowing down of the dynamics of PMN and its eventual freezing into non-ergodic phase at low temperature is a result of quenched high temperature disorder inherent in relaxor ferroelectrics with random orientations (electric dipoles, lattice defects, and contamination). The model states the structural phase transition into a ferroelectric state is destroyed by virtue of quenched random local fields. It is thought that the random fields and random interactions between the defects and the polar regions leads to the freezing transition into a glassy state, predicting the frequency dependence of the permittivity as a function of temperature. This model also highlighted that the Barkhausen jumps observed during the poling process (also observed by Colla[56] et al.) do not agree with the glassy dipolar model on a microscopic length scale.

To date, the origin and nature of non-ergodic behavior in relaxors remains controversial. The commonly accepted model for PMN is the spherical random-bond–random-field (SRBRF) model, which explains the low temperature freezing behavior by assuming that the formation and freezing of polar nanoregions are distinct phenomena. In the spherical random-bond–random-field (SRBRF) models[57,58], Pirc and Blinc assumed that PNRs are spherical and interact randomly via spin-glass type random exchange coupling, while being subjected to a random quenched internal electric field (a frozen dipole glass state for relaxor). This model describes the temperature dependence of the Edwards-Anderson glass order parameter q in terms of random fields and random bonds. In the absence of random fields for certain limiting interacting bond lengths, the theory predicts the transition from ergodic to ferroelectric phase with spontaneous

polarization. With increasing bond lengths, the system transforms into a spherical glass phase

without long range order. The presence of random fields destroys the phase transition with non-

zero q.

Relaxor to normal ferroelectric transitions can be introduced to PMN with addition of B-

site substitutional as shown in Figure 0-13 [59–62]. For example, addition of >10 vol. % Ti to PMN

stabilizes the rhombohedral phase with polarization along <111> upon cooling[61]. Interestingly,

increasing Ti concentration can increase the size of the polar macrodomain, but also causes

dilution of the electrostatic and strain interactions between Nb^{5+} and Mg^{2+} ions, thus reducing

their tendency to order.[63] This makes 67PMN-33PT (morphotropic phase transition composition)

a disordered perovskite.
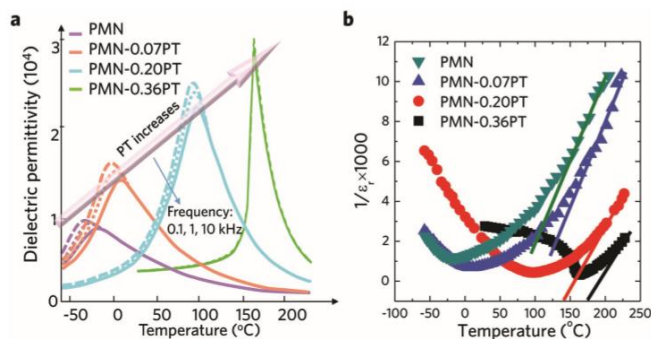
Figure 0-14:(a) Temperature dependence of the dielectric permittivity of PMN ceramic with increasing PT as a function of frequency. (b)Temperature dependence of the reciprocal of dielectric permittivity for PMN ceramic with increasing PT (<36%), where the straight lines reveal that the dielectric responses of PMN-PT ceramics start to follow Curie–Weiss law at the temperature much higher than T_{max} for PMN.

2.2 Rayleigh analysis: probing nonlinearity in normal ferroelectric and relaxor ferroelectric thin films

Small signal dielectric nonlinearities can provide insight into the response of mobile

interfaces like domain walls[64–67], phase boundaries or nano-polar regions[68–71] to dynamic electric

fields, in addition to intrinsic lattice responses. This can be a valuable tool in understanding the contributions of mobile interfaces in both normal ferroelectrics and materials along the ferroelectric-relaxor continuum. The Rayleigh law was first used by Neel et al.[72–74] to describe the physical origin of magnetization induced in a ferromagnetic material, due to the displacement of a single ferromagnetic domain wall in an environment in which the potential energy of the wall varies irregularly with position of the wall. He proposed that the randomly distributed pinning defects in a material introduce perturbations in the potential energy for domain wall motion; the resulting domain wall displacement produced Rayleigh characteristics (reversible linear and irreversible quadratic component as shown in Figure 0-15) The law is valid for low-field conditions, where the density and the structure of the domain walls remain unchanged, as the field is cycled. The hysteretic behavior arises when the walls moves from one potential minima to another, corresponding to the pinning and depinning of the domain walls by pinning centers.
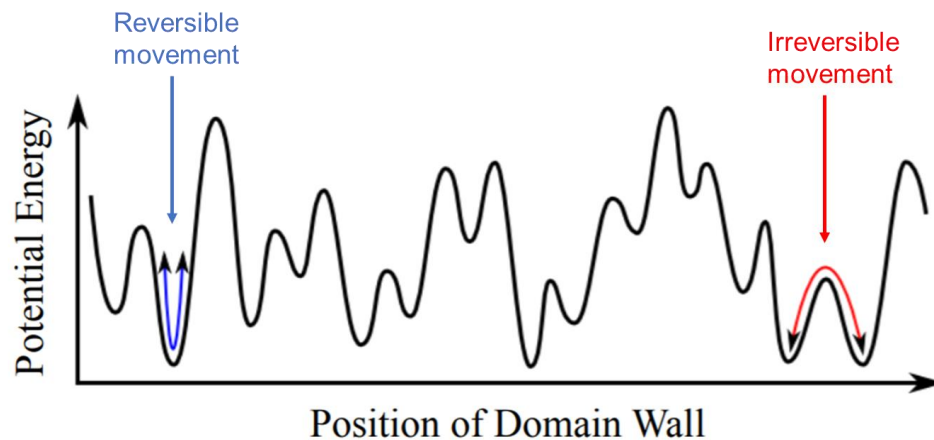
Figure 0-16: Potential energy landscape for domain wall motion in an environment with randomly distributed pinning centers[75]

Drawing an analogy with ferromagnetic materials, the Rayleigh law has been applied to describe the nonlinear dielectric and piezoelectric response in ferroelectrics[73,76]. For example, the

dielectric permittivity or piezoelectric coefficient as a function of amplitude of ac electric field E_{ac}, has a reversible component, ε_{init} or d_{init}, and an irreversible component, α_e or α_d, as described in Equations 0-3 and 0-4.

$$\varepsilon = \varepsilon_{init} + \alpha_e E_{AC} \qquad\qquad \text{Equation 0-5}$$

$$d = d_{init} + \alpha_d E_{AC} \qquad\qquad \text{Equation 0-6}$$

The initial permittivity and piezoelectric constant are attributed to the intrinsic lattice response and the non-lossy reversible movement of domain walls and phase boundaries. The irreversible domain wall or phase boundary motion and its dependence on the external ac field occur when the applied field is sufficiently large to overcome the potential barrier separating local energy minima. The Rayleigh law only applies in the regime where the permittivity and piezoelectric constant scale linearly with the ac electric field. Typically, this range is up to ⅓ – ½ the coercive field. For a Rayleigh-like ferroelectric material, the link between non-linearity and hysteresis also describe the sub-switching polarization response[65,77], as shown in **Equation 0-4**, where P is the polarization, $E = E_0 \sin \omega t$ is the applied alternating electric field, ε_{init} is the dielectric permittivity at the zero field, and α is the Rayleigh coefficient. The sign "+" stands for decreasing and "-" for the increasing part of the alternating field.

$$P = (\varepsilon_{init} + \alpha E_0)E \pm \alpha(E^2 - E_0^2) + \cdots \qquad \text{Equation 0-4}$$

It is important to note that for a more complete description of a real, non-ideal material, **Equation 0-4** may possess additional terms reflecting the degree of randomness of the energy profile[74]. Investigation of an ac-signal through its harmonic amplitudes and phase angles is useful to study nonlinear systems. Harmonic analysis of the sample response permits the study of different contributions to nonlinearity, if the material response is the result of several contributions differently depending on time.

2.3 Role of substrate clamping in thin ferroelectric films

The dielectric and piezoelectric responses of a ferroelectric material arise from contributions of both the intrinsic lattice (controlled by the material structure and composition) and extrinsic factors like domain wall mobility and motion of phase boundaries (which will be influenced by stoichiometry, mechanical boundary conditions and defect concentrations)[72]. The extrinsic contributions to the piezoelectric response are due primarily to non 180° domain walls, though nearly reversible motion of purely ferroelectric walls can also contribute[67]. Extrinsic responses in ferroelectrics can be pinned by point and line defects, grain boundaries and the substrate (for films) among other factors [66]. Lateral and thickness scaling of these films is required for various applications, and necessitates improved understanding and quantification of the factors influencing the piezoelectric response in thin films such as (i) grain size and orientation[78–81], (ii) property degradation owing to process- induced damages[82–86] and (iii) elastic interaction at the film-substrate interfaces.[87,88]

Among these factors, substrate-induced clamping can significantly reduce the converse piezoresponse coefficient $d_{33,f}$ in continuous piezoelectric films, relative to single crystal values for the same composition[89–95]. Application of the electric field to the thin ferroelectric film induces an out-of-plane piezoelectric strain. However, as the film expands out-of-plane, it contracts in-plane due to the d_{31} coefficient. Because the film is bonded to the underlying substrate, the lateral contraction is frustrated, thereby reducing the out-of-plane strain. Assuming zero in-plane strain in the thin film, this effective $d_{33,f}$ can be calculated using the formulation proposed by Lefki and Dorman given as:

$$d_{33,f} = d_{33} - \frac{2d_{31}s_{13}^E}{s_{11}^E + s_{12}^E}$$

Equation 0-7

where d_{33} is the unclamped piezoelectric coefficient of the film, s_{ij}^E are the mechanical compliances at constant strain and d_{31} is the transverse piezoelectric coefficient.

Lateral patterning can reduce the residual stress state of the film, affecting the intrinsic response and lowering the energy barriers for domain wall motion. Nagarajan[89] et al. demonstrated a ~3x increase in $d_{33,f}$ from switching ferroelastic 90° domain walls (from the in-plane *a*-domain state to a *c*-domain state) in partially declamped micron sized islands ion-milled in 100 nm thick epitaxial $PbZr_{0.2}Ti_{0.8}O_3$ films. Additionally Griggio[94] et al. and Wallace[95] et al. have shown that the 90° ferroelastic domain reorientation in released $PbZr_{1-x}Ti_xO_3$ films is comparable to that in bulk ceramics of similar composition. Keech[92] et al. demonstrated that subdividing a 350 nm thick $0.7PbMg_{0.33}Nb_{0.67}O_3$-$0.3PbTiO_3$ film (grown on platinized silicon) into 300 nm wide lines produces a ~3x enhancement in dielectric response and a 300% increase in irreversible domain wall contributions; the effect of substrate release exceeded that of etch-induced damage. Such declamping will have a profound impact on several applications - one such example is the high speed, low power piezoelectric transistor[10] proposed by IBM to address the challenges posed by stalled clock speeds in complementary metal oxide semiconductor transistor (CMOS) technology[9]. This approach relies on the high strain generated in nanostructured piezoelectric films to actuate a piezo-resistive switch element. There is, therefore, a growing need to develop high accuracy and high-resolution metrology for characterization of patterned piezoelectric thin films.

Chapter 3

Relaxor behavior in ordered lead magnesium niobate (PbMg$_{1/3}$Nb$_{2/3}$O$_3$) thin films

3.1 Introduction

Fully-ordered, stoichiometric PMN materials have not been grown as bulk ceramics, though varying degrees of cation order have been achieved with doping in a narrow window of kinetic activity and thermodynamic stability[7,42]. In bulk materials, the chemically ordered regions, formed at or below the sintering temperature (~1223K), are limited to 2-5 nm in dimension.

PMN undergoes a thermodynamic order-to-disorder transition at temperatures below 1073 K, which might kinetically restrict the development of ordered phase[7,41,42]. This work aims to address this kinetic-growth limitation required to achieve a thermodynamically-stable, ordered state in PMN, via synthesis of thin PMN heterostructure films with ordered layers of stoichiometric Pb[Mg$_{2/3}$Nb$_{1/3}$]O$_3$ and PbNbO$_3$ grown at lower temperature as per the charge balanced random site model. This is illustrated in the schematic in Figure 3-1. (111)-oriented films were grown on SrTiO$_3$ substrates with conducting La$_{0.7}$Sr$_{0.3}$MnO$_3$ bottom electrodes using timed pulsed-laser deposition. Without RHEED, it was not possible to get layer-by-layer growth in these relaxed films. That said, for any area on the surface, the fluxes were delivered with

alternating compositions. This enabled growth of local long range ordered

$Pb([Mg^{2+}_{2/3}Nb^{5+}_{1/3}]_{1/2}[Nb^{5+}]_{1/2})O_3$ regions in the film matrix with reduced relaxor-like behavior at

length scales not achievable in bulk, while ensuring local lead stoichiometry. Though the relaxor

behavior did not switch "off", this work can have implications on understanding the impact of

chemical ordering on polar domains in PMN. TEM characterization, supported by dielectric and

second-harmonic generation measurements, suggests that the low-temperature state of these PMN

heterostructures is ferroelectric with domains of tens of nanometer size, similar to the assertion

made by Fu et al. in PMN single crystals[96]. With decreasing temperature, it is speculated that

there is a continuum of ferroelectric and relaxor behavior, with increased percolating volume

fraction of PNR in long range ordered PMN heterostructure films.
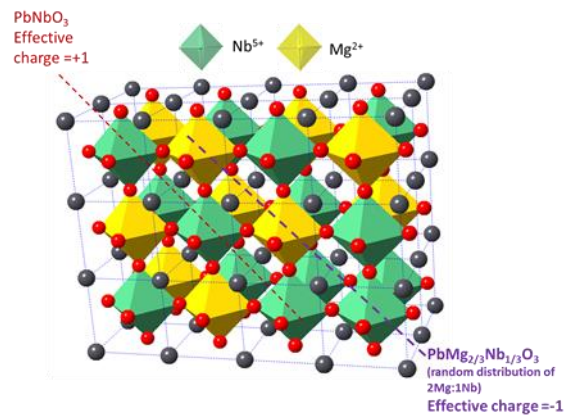
Figure 3-1: Proposed PMN heterostructure with alternate $PbNbO_3$ and $PbMg_{2/3}Nb_{1/3}O_3$ layering along <111>

3.2 Experimental procedure

Prior to deposition, (001) and (111) $SrTiO_3$ substrates were prepared by chemical etching

with a 50:1 buffered-oxide etchant (BHF) for 6 minutes, followed by a thermal anneal at 1273 K

for 3 hours in order to achieve step-terrace structures for the step-flow/layer-by-layer growth of the

bottom electrode. $La_{0.7}Sr_{0.3}MnO_3$ films (~45 nm thick) were epitaxially grown as the bottom electrode on the treated $SrTiO_3$ substrates by pulsed-laser deposition, employing a KrF excimer laser (248 nm; Coherent LPX305) from a ceramic $La_{0.7}Sr_{0.3}MnO_3$ target (Praxair Specialty Ceramics). The $La_{0.7}Sr_{0.3}MnO_3$ layer was deposited at 973 K in an oxygen pressure of 100 mTorr, with a laser fluence of 1.5 J/cm^2 at a repetition rate of 5 Hz. Heterogeneous long-range-ordered PMN film growth was achieved via subsequent pulsing of the $Pb_{1.2}NbO_{3.2}$ and $Pb_{1.2}Mg_{2/3}Nb_{1/3}O_{3.2}$ targets doped with 1% La doped at 873 K in an oxygen pressure of 200 mTorr at a laser fluence of 0.75 J/cm^2 and a laser repetition rate of 3 Hz. Short-range-ordered $PbMg_{1/3}Nb_{2/3}O_3$ films were also grown from a single stoichiometric PMN target with 20% excess Pb, under similar growth conditions for comparison. Following growth, all samples were cooled to room temperature at a static oxygen pressure of 100 Torr. For clarity, the multi-target films are referred as long-range-ordered PMN heterostructures (LRO) while the single target films are referred as short-range-ordered PMN (SRO). Additionally, initial heterostructure growth results using RHEED based pulsed laser deposition system have been summarized in Appendix A.

The crystalline structure of the films was investigated by PANalytical 4-circle X'Pert 3 MRD X-ray diffractometer (XRD) with Cu Ka radiation (PANalytical B.V., Almelo, The Netherlands). Compositional analysis was performed on the two-target films using Rutherford Backscattering by Liv Dedon at the Lawrence Berkeley National Laboratory with incident ion energy of 3040 keV, incident angle α (22.5 °), exit angle β (25.35 °), and scattering angle (168 °). Data were fit using the SIMNRA software (Max-Planck-Institute for Plasmaphysics, Germany). 100-nm-thick platinum top electrodes were sputter deposited via a lift-off procedure for electrical characterization. Temperature-dependent structural characterization was achieved using a Gatan cooling in-situ holder (Model 613) on a Titan3 dual aberration corrected scanning/TEM (S/TEM) operated at 200 kV. Room temperature selected area electron diffraction followed by dark-field imaging was used to identify the F-type ordering spot {h+1/2, k+1/2, l+1/2} and chemically-

ordered domains for both long range ordered and short range ordered PMN samples, similar to the procedure employed in bulk samples[63]. In addition, the PNRs were imaged at the 111-fundamental reflection as a function of temperature (100-296 K) in the long range ordered PMN heterostructures. TEM specimens were prepared by *in situ* milling in a FEI Helios NanoLab DualBeam 660 focused-ion beam (FIB). Before milling, a thick protective amorphous carbon layer was deposited over the region of interest by electron-beam deposition. The FIB-TEM membrane was fabricated with a starting milling voltage of 30 kV that was then stepped down to 2 kV to minimize sidewall damage and thin the specimen to electron transparency.

Temperature dependent polarization – electric field hysteresis loops, small signal dielectric response, and the ac field dependence of the dielectric response were characterized using a cryo-cooled probe station (Lakeshore CRX-VF) from 10 -350 K. Prior to measurement, both long-range-ordered and short-range-ordered samples were annealed at 723 K in a rapid thermal annealer for 1 min to erase any aging. The samples were subsequently zero field cooled to 10 K in the cryocooled probe station and the dielectric response was measured on heating. Polarization-electric field (P-E) hysteresis loops were measured at 10 kHz using a Multiferroic tester (Radiant Technology, Inc. Albuquerque, NM). The ac field and frequency dependence of the relative dielectric permittivity was characterized using an HP 4248A precision LCR meter (Agilent Technology, Palo Alto, CA) from 0.5-100 kHz. Thermal depolarization measurement was carried out on long-range-ordered PMN heterostructure film using a pA meter (HP 4140 B) during zero-field heating (heating rate of ~4 K/min) in the temperature range of 75-400 K. The sample has been previously cooled under an electric field of 200 kV/cm (cooling rate of ~1 K/min). Second harmonic generation measurements were conducted to verify the transition temperature and symmetry breaking without the application of an electric field. A Janis ST300 (Janis Research Company, Woburn, MA) temperature system with liquid nitrogen coolant was used to control the sample temperature during measurements. The samples were probed using a Solstice Ace (Spectra-Physics, Santa Clara, CA) femtosecond pulsed

laser beam (100 fs, 1kHz) at a fundamental wavelength of 800 nm. The second harmonic signal (400 nm) was detected using a photomultiplier tube (Hamamatsu H7826, Hamamatsu, Japan) and a Stanford Research (Sunnyvale, CA) SR830 lock-in amplifier.

3.3 Results and discussion

3.3.1 Structural/compositional characterization

XRD patterns for the long-range ordered PMN heterostructure and the short-range-ordered PMN films, grown on (001) and (111) STO substrates are shown in Figure 3-2(a). Phase pure perovskite films were obtained for growth on (111) substrates, while a niobium-rich second phase developed for films on (001) STO. Long-range-ordered PMN heterostructure films exhibited a full width half maximum of 0.1° in the ω rocking curves about the 111 reflection, as shown in the inset of Figure 3-2(b). Superstructure reflections of type (1/2 1/2 1/2) were not observed in the XRD pattern. This could be attributed to the incomplete ordering and/or length scale of the randomly distributed chemically ordered regions. Single target short-range-ordered PMN films were also found to be phase pure. PMN is relaxed at the grown thicknesses for both short-range and long-range films. Compositional analysis using the Rutherford backscattering technique, as shown in Figure 3-3 (a) and (b) shows the average film composition in a long-range-ordered film. Note the Mg peak was very close to the noise level and can skew the Mg:Nb ratio fit.
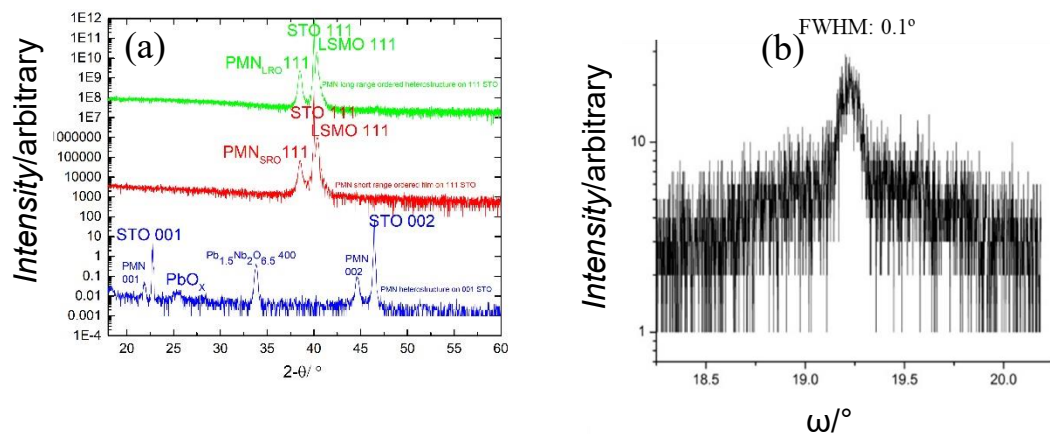
Figure 3-2: (a) XRD pattern for long range ordered PMN heterostructure film grown on 001 and 111 STO (labelled as PMN$_{LRO}$)and short range ordered PMN on 111 STO (labelled as PMN$_{SRO}$) (b) ω-scan for 111 reflection on 30 nm PMN heterostructure film grown on STO.
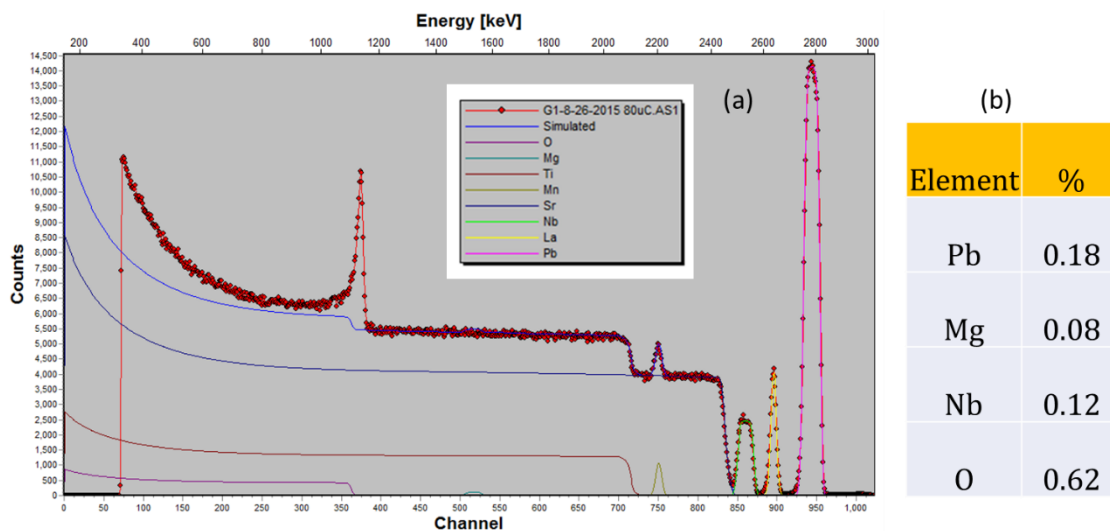
Figure 3-3: (a) Simulated data fit to the experimental data on the long range ordered PMN heterostructure film obtained by Rutherfold Backscattering (b) Calculated elemental composition from simulation.

A TEM image [Figure 3-4(a)] and the fast Fourier transform (FFT) from the corresponding high resolution TEM image from the same region (Figure 3-4(b)) indicate epitaxial growth of the 100 nm thick PMN heterostructure on the 45 nm thick LSMO bottom electrode. No evidence of secondary phases was observed in the sample by TEM, in agreement with the XRD investigations. The dislocation density is not so high, though there are some edge dislocations at the interface; these dislocations are somewhat curved and appear without a fixed period. The FFT along the [-112] pole shows the ($\frac{1}{2}$, $\frac{1}{2}$, $\frac{1}{2}$) superstructure reflections indicating cation ordering. The dark field images in Figures 3-4(c) (d) and (e) were acquired using one of these superstructure reflections and show long-range-ordered domains as large as 150 nm (marked as a dotted region in the image (d). Fig 3-4(c), (d) and (e) shows the chemically ordered regions are distributed in the heterostructure film (throughout the TEM sample size). Figure 3-5 (a) is a TEM image showing the cross-sectional structure of a short-range-ordered PMN film on LSMO/STO. In contrast, the FFT from the corresponding high resolution TEM image of the epitaxial PMN deposited from the single target shows diffuse superlattice reflections for chemical ordering, as expected. Additionally, in the dark field TEM data (Figure 3-5(c)), fewer ordered regions were observed with sizes less than 10 nm.
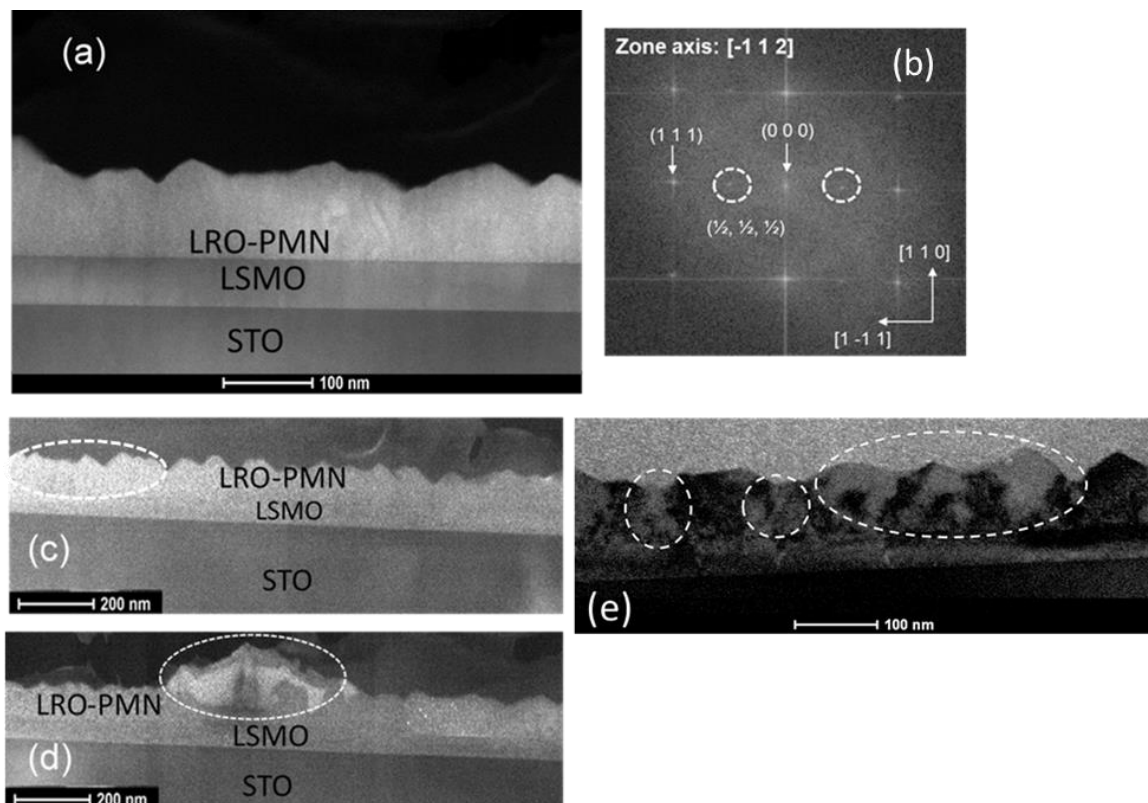
Figure 3-4: (a) A cross-section TEM image of a long range ordered heterostructure PMN (111) film (marked LRO-PMN) on LSMO/STO (111) recorded along the [−112] pole (b) FFT from a high resolution TEM image showing superstructure reflections; (c)(d) (e) cross-sectional dark field images captured using one of the superstructure reflections in (b), revealing the highlighted cation-ordered domain in the film.
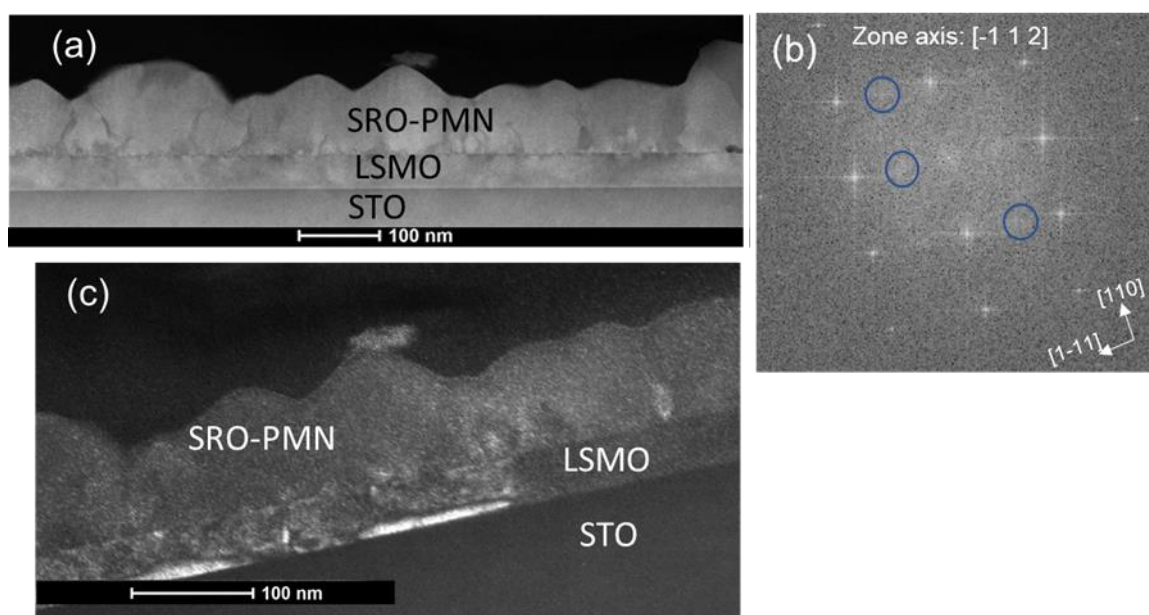
Figure 3-5:(a) A cross-section TEM image pattern of a short range ordered PMN (111) film (marked SRO-PMN) on LSMO/STO (111) (b) FFT of a high resolution TEM image recorded along the [−112] pole showing diffused superstructure reflections (marked by blue circles) associated with short-range cation ordering; (c) a cross-sectional dark field image captured using one of the superstructure reflections in (inset), revealing cation-ordered domains in the PMN film of a few tens of nm in size.

Figure 3-6 show the bright and dark field images of the same area imaged using the 111 reflection at room temperature and 100 K in situ, obtained during a heating cycle for the long-range-ordered PMN heterostructure. Figure 3-6(a) and (b) were collected at room temperature, while (c) and (d) were at 100 K. Clearly the microstructures are very different between these two temperatures. In the dark field images (Figure 3-6(d) and (e)) shown at 100 K, a fringe-like contrast having a spacing of ~0.7 nm is seen in volumes with columnar shape. The long axis of those columnar regions is normal to the interface; the domains are ~10-20 nm in size along the short axis and ~50 nm along the long axis. This observation is consistent with the polar microdomain imaging in the (110) orientation, reported in bulk PMN during heating[59,97]. These fine structures disappear as the film is heated beyond 220 K, as evident in the temperature dependent nanopolar imaging shown in Figure 3.7. These fringe-like structures are speculated to be a *result* of polar macrodomains of the rhombohedral phase, as suggested by previous work[59,97].

The average fringe distance (D) was measured to be approximately 0.7 nm, which is unlikely to be Moire fringes caused by lateral overlapping of 111 planes (d spacing= 0.225 nm). Additionally, a rotational Moire pattern is assumed to exist, the twist angle (α)[98] calculated using the relation (D=d/2 sin (0.5 α)) turns out to be 18°, which is inconsistent with epitaxy. In addition, these features are consistently temperature dependent. Based on the contrast from dark field, the volume fraction of the polar cluster was estimated to be ~20-30% at 100K. This volume fraction is above the theoretical prediction for geometrical in-plane percolation threshold[99] (18-20%) for iso-parametric overlapping ellipsoidal clusters with aspect ratio ranging from 1:5 to 1:2.5 and consistent with the neutron scattering pair distribution function analysis results at 15K by Jeong *et al.*[100]. This favors the prevalence of ferroelectric state in ordered PMN at low temperature.
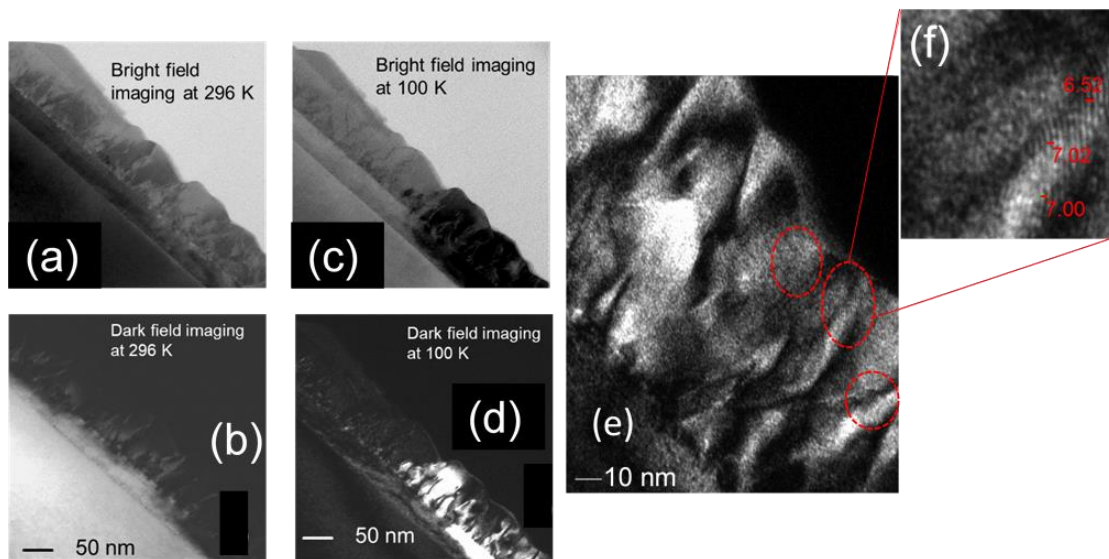
Figure 3-6: (a),(b) Cross-sectional bright and dark field TEM image of ordered heterostructure PMN (111) film on LSMO/STO (111) at 296 K (c),(d) A cross-section bright and dark field TEM image of or PMN (111) film on LSMO/STO (111) at 10 K, (e) A magnified dark field image (red circular regions show polar fringes) and (f) magnified image showing evidence of polar nanoregion striations through the film thickness with interfringe spacing of ~7 nm.
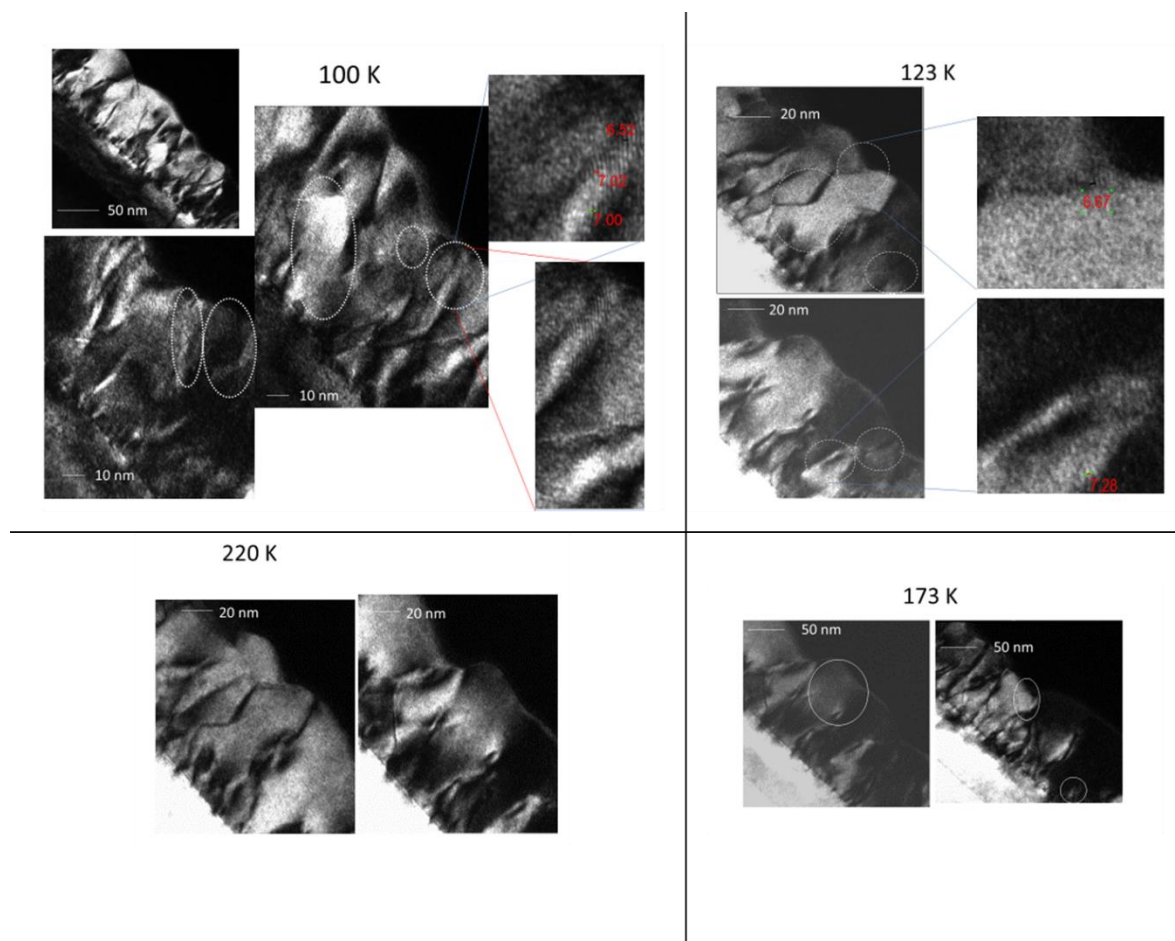
Figure 3-7: Temperature evolution of the polar nanoregion from 100 -220K. The polar nanoregion fringe like structures disappear completely at 220 K.

3.3.2 Electrical characterization

The ferroelectric properties of the ordered PMN heterostructure film were studied by polarization – electric field (P-E) hysteresis loop measurements as a function of temperature. Slim, but well-defined nested hysteresis loops were obtained, as shown in Figure 3-8a, with low levels of leakage. At room temperature, twice the remanent polarization ($2P_r$) and coercive field (E_c) of the heterostructure PMN film were found to be 11.3 ± 0.3 $\mu C/cm^2$ and -110 kV/cm, respectively. Compared to short range ordered films, the polarization increased by 38% under similar electric field conditions. The polarization value is considerably higher than in previously reported work, presumably due to stabilization of the field-induced polarization as a consequence of the partial cation ordering achieved in the film. The ferroelectric behavior of the films was also confirmed by capacitance-field measurements; as shown in Figure 3-8b, the data show switching peaks that are the fingerprint of the ferroelectric switching. Increasing nonlinearity and hysteresis was observed in large signal P-E hysteresis loops as the temperature was lowered to 10 K. At low temperature, the loops became increasingly square [Figure3- 8(c)]; on heating. the temperature dependence of the remanent polarization reveals a gradual loss in polarization with temperature which is consistent with relaxor characteristics. As shown in Figure 3.8 (d), compared with measured and calculated $\sqrt{P_s^2}$ in bulk ceramic and single crystal PMN[14,15], the observed polarization is lower, however confirms a decreasing trend up to T_{Burns} (~600 K).

Figure 3-9(a) and 3-9(b) show the temperature dependence of the relative dielectric constant and its loss at different frequencies, for 100 nm thick long-range-ordered and short-range-ordered PMN films. The long-range-ordered PMN heterostructure shows less dispersion of the permittivity, compared to that found in the short-range-ordered film. The shift in T_{max} (compared at the highest and the lowest frequencies) in the case of a short-range-ordered film is ~40 K, however in the case of long-range-ordered film, this difference is ~25 K. In the long-range-ordered film beyond T_{max},

the dielectric response converged while more space charge in the short- range-ordered film leads to a failure to converge the permittivity data above T_{max}. As expected, the maximum permittivity of the PMN thin film is much below that of bulk ceramics (~16,000), which is certainly due, at least in part to substrate clamping[79,101].
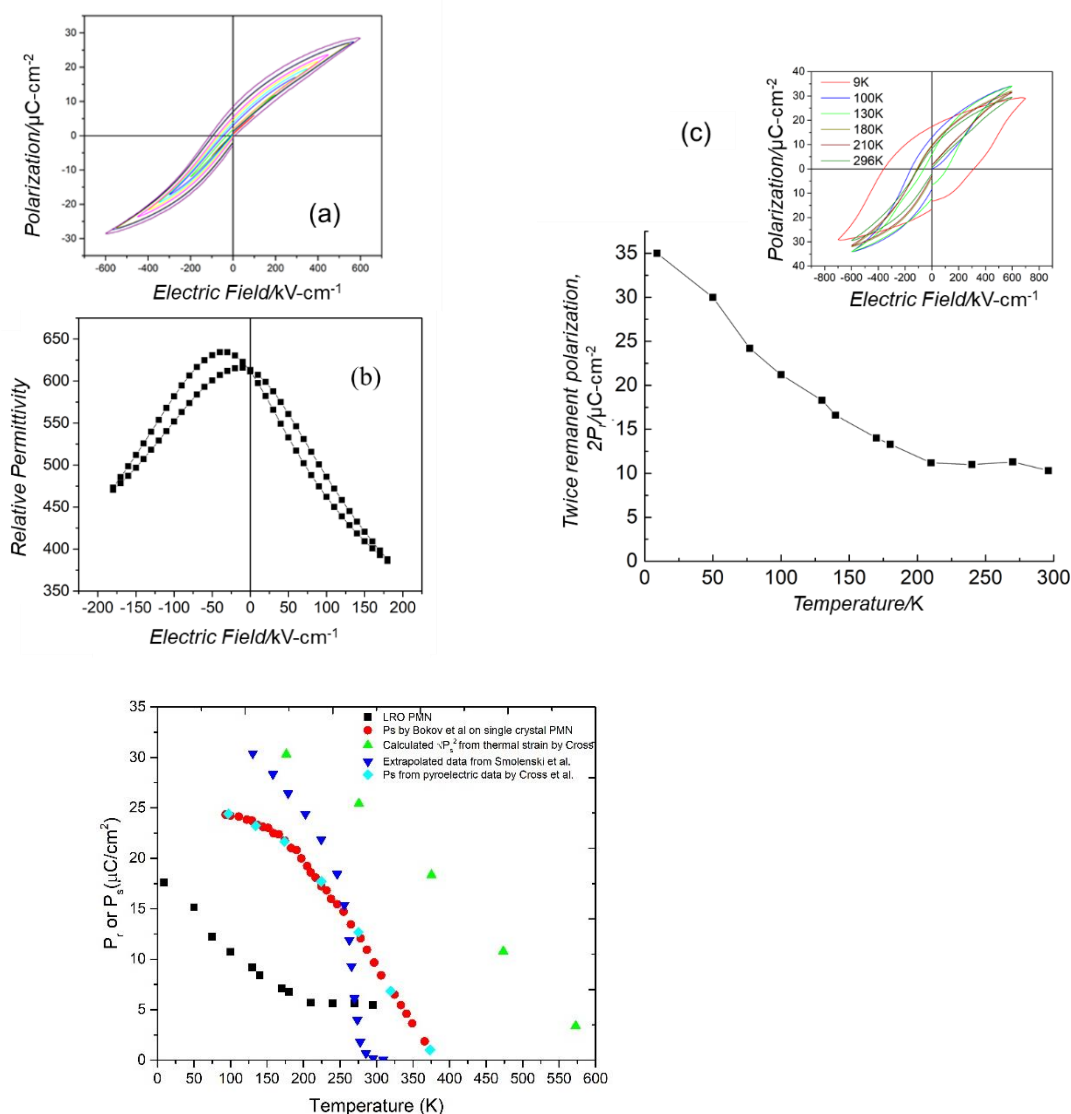
Figure 3-8:(a) Room temperature P-E loop evolution as a function of ac field; (b) permittivity field data at 10 kHz showing switching (c) Twice the remanent polarization ($2P_r$) as a function of temperature with an inset showing polarization evolution in long-range-ordered PMN

heterostructure thin films at select temperatures (d) Comparison of LRO polarization as a function of temperature upto T_{Burns} (~600 K) with bulk ceramic and single crystal PMN.
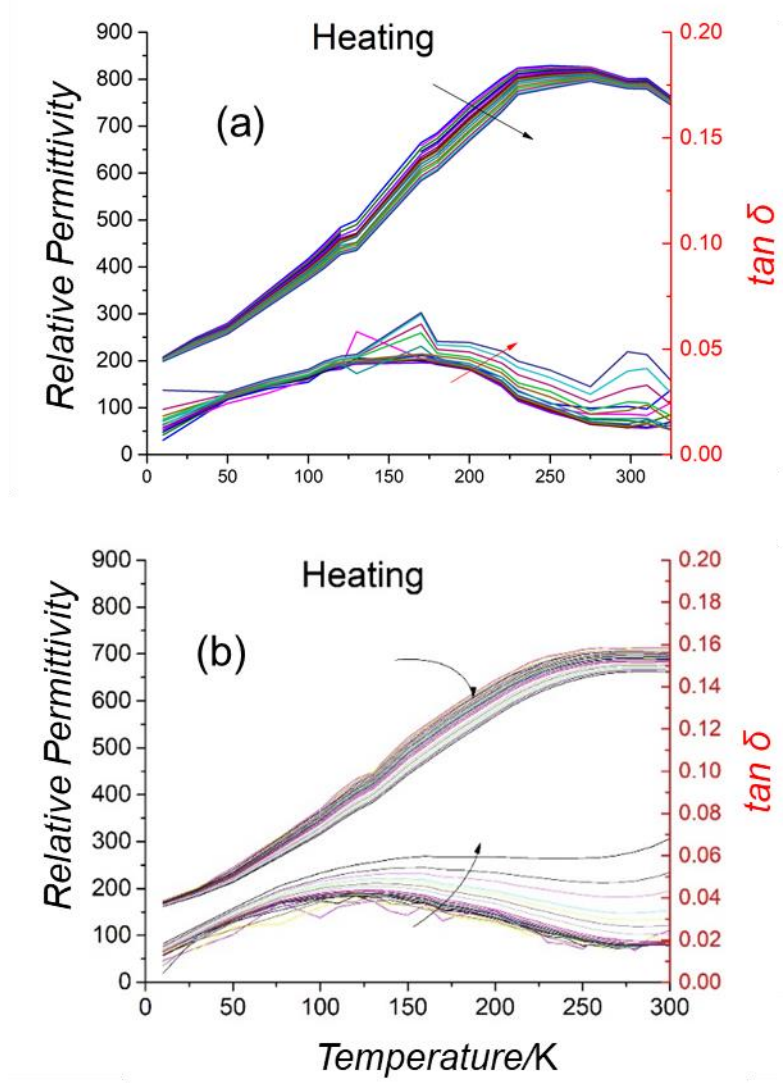
Figure 3.9: (a) Temperature dependence of dielectric response for long-range-ordered PMN films as a function of frequency measured during a heating cycle (b) Temperature dependence of dielectric response for short-range-ordered PMN films as a function of frequency during a heating cycle. Note: arrows indicate increasing frequency (from ~ 1 kHz - ~ 300 kHz). In both cases, the upper set of curves correspond to the permittivity and the lower set of curves correspond to the loss tangent.

The relaxor behavior did not turn "off" completely in the long-range-ordered sample, despite observing increased size of chemically ordered regions in TEM. Electron diffraction is poor at distinguishing complete and partial ordering. Recent atomic resolution HAADF STEM imaging work by Lebeau et al.[102] demonstrated the presence of chemical order gradients within each COR in relaxor PMN, rather than abrupt transition between the COR and disordered matrix, as shown in Figure 3.10 (a). Also, the order metric (defined as the standard deviation of the Mg/Nb atom column intensities surrounding each Pb/O atom column normalized to mean) is independent of the COR size in the ordering gradient mode as shown in Figure 3.10 (b). Thus, relaxor behavior in PMN might be strongly influenced by the disorder inherent in the β' sublattice of the COR in the ordered PMN films. This random positional disorder cannot be controlled during growth and hence ordering along one dimension is not enough to turn off relaxor ferroelectricity. Our results assert a mixture of ferroelectric and relaxor behavior in the long-range-ordered PMN heterostructure films, as the ordering observed is inadequate to drive a fully ferroelectric state.
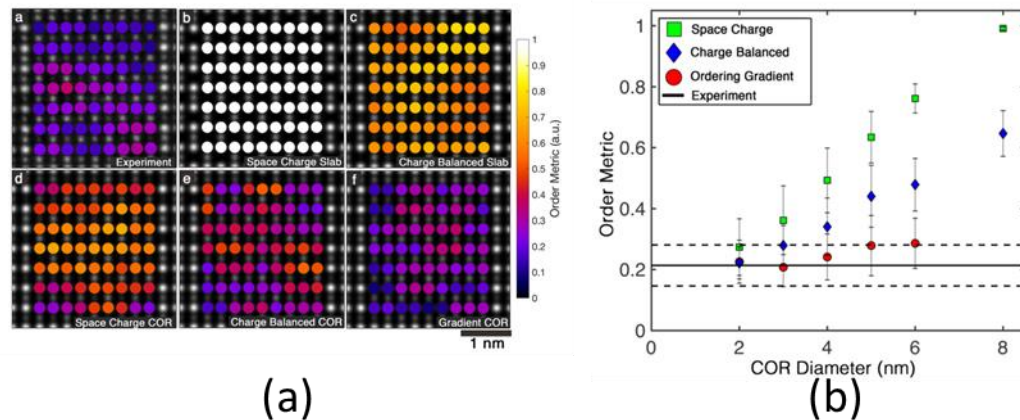
Figure 3.10: (a) Order metrics match for a 4 nm representative COR from experiment with ordering

gradient model proposed by LeBeau et al.[102] (b) Average order metrics as a function of COR size

Figure 3-11(a) shows the effect of increasing ac field (3-25 kV/cm) as measured at 1 kHz on long-range-ordered PMN films, as a function of temperature. The permittivity increased linearly as a function of ac field, with T_{max} shifting to lower temperature. These data were fitted using the Rayleigh law $\varepsilon_r = \varepsilon_{init} + \alpha E_{ac}$ for ac fiels up to ~1/3-1/2*coercive field. The irreversible Rayleigh coefficient α represents the irreversible movement of domain walls, polar cluster boundaries, or phase boundaries, while ε_{init} arises from both the intrinsic response and reversible motion of boundaries. The Rayleigh coefficients decrease at higher frequencies, which would be consistent with observations by Glazunov et al.[103] in PMN single crystals. These data suggest a domain wall or interface boundary type relaxation phenomenon, instead of the thermally activated polarization flips, as would have been suggested by the superparaelectric model. As observed in Figure 3-11(b), α peaked at 130-140 K for the heterostructure sample. The decrease in α at low temperatures is presumed to be due to loss of thermal activation of the mobile boundaries, as described by Li et al.[5] The decrease in α at high temperature is likely to be due to a reduction in the number of mobile boundaries; this could be due to loss of a long-range-ordered ferroelectric phase or to a decrease in the volume fraction of micropolar regions. For the short-range-ordered PMN film, α goes through a similar peak, but the magnitude of α is smaller.

Figure 3-12 shows the thermal depolarization current density measured on heating under zero field conditions in the long range ordered PMN heterostructure films from 75 K-275 K. This shows the presence of depolarization temperature peak at ~125 K, which is in close agreement to the maximum in the irreversible Rayleigh coefficient. This peak would correspond to the discharge of the polarization developed during the prior field cooling on the sample, similar to field induced

normal ferroelectric to relaxor phase transition in doped PMN ceramics[104]. The calculated polarization, obtained by integrating the area under the curve in the temperature range from 75 K-225 K was ~4.2 μC/cm^2. This low value may be attributed to the loss in polarization due to time dependent zero field aging, previously observed in PMN single crystals above 200 K[105,106]. The depolarization temperature at 125 K is much lower than that in undoped bulk PMN (~213 K), which may be partly attributed to 1% La doping of the Pb$_{1.2}$Mg$_{2/3}$Nb$_{1/3}$O$_{3.2}$ target; as demonstrated by Zhao et al[104].
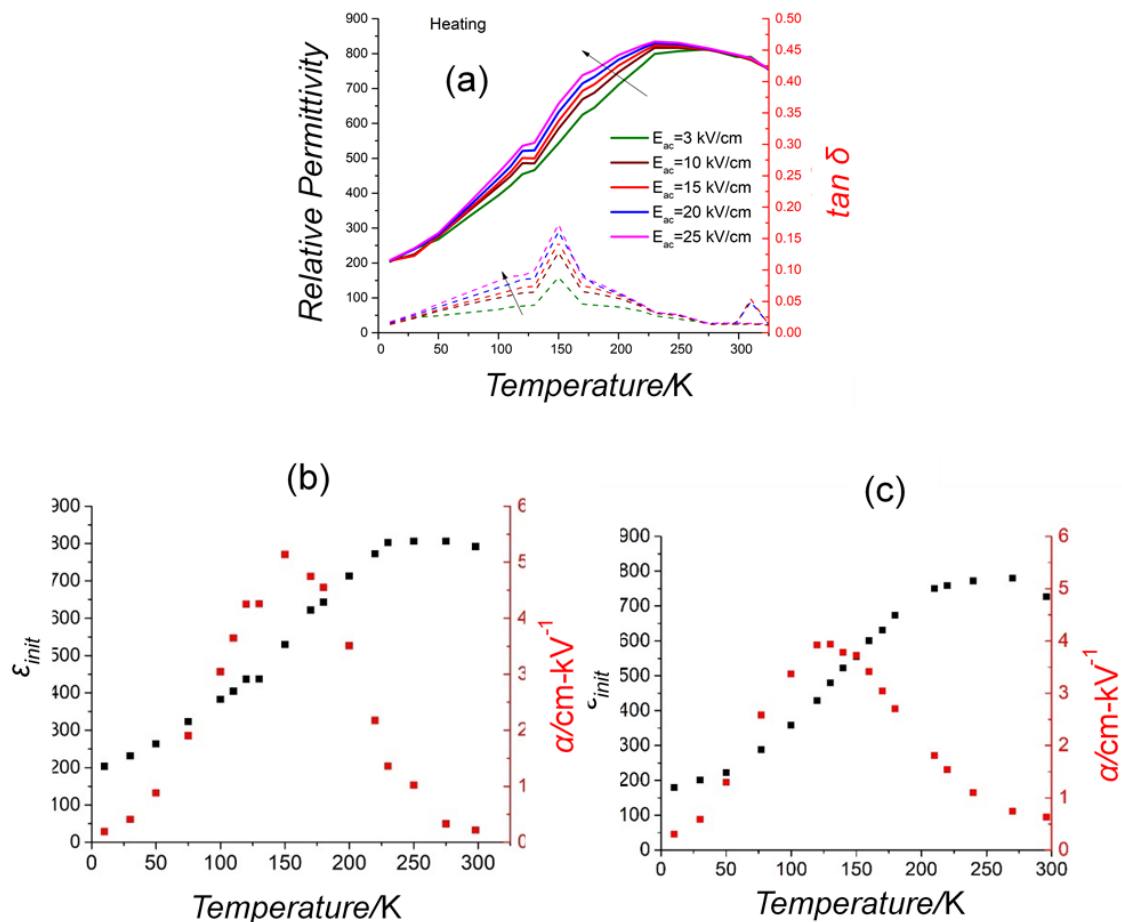
Figure 3-11: (a) Dielectric permittivity of ordered PMN as a function of ac field measured at 1kHz (b) Reversible and irreversible Rayleigh coefficients of the relative permittivity of a heterostructure PMN film as a function of temperature (c) Reversible and irreversible Rayleigh

coefficients of the relative permittivity of a short-range-ordered PMN film as a function of temperature
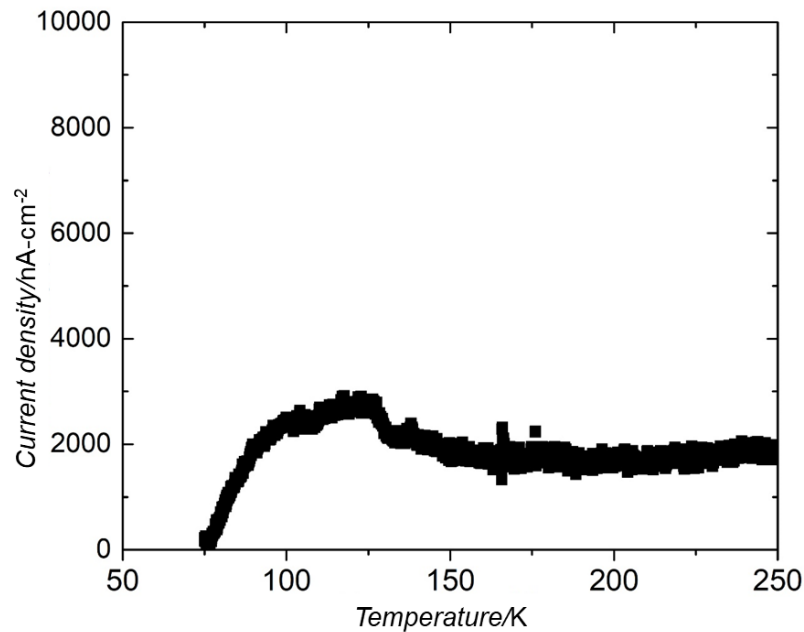
Figure 3-12: Depolarization current from long-range-ordered PMN on heating at E=0 KV/cm, after cooling at E=275 kV/cm, showing peak at 125 K. Data measured for the other polarization direction were extremely noisy due to low retention of the poled state.

3.3.3 Second harmonic generation (SHG) optical measurement

Second harmonic generation measurements were used to further investigate the

heterostructure films as a function of temperature. This technique does not require the application

of electric fields, eliminating the potential impact of the small signals used for dielectric

characterization on nucleation of a long-range-ordered ferroelectric phase. Figure 3-13 shows the

SHG response for LSMO (bottom electrode), short-range-ordered PMN film and the long-range-

ordered PMN heterostructures during heating and cooling cycles. Compared to short-range-

ordered PMN, the long-range-ordered PMN films showed larger signals, suggesting an increased

volume of a polar phase or larger nonlinear optical constant. Additionally, in the case of the PMN

heterostructures, onset of features were consistently observed in the SHG data at 130 K during the

heating cycle; the 130 K anomaly matches the temperature of the peak in the irreversible

Rayleigh coefficient. This might indicate a change in ferroelectric ordering, due to the disruption

of percolated domains (formed during the cooling cycle) with increasing temperature.
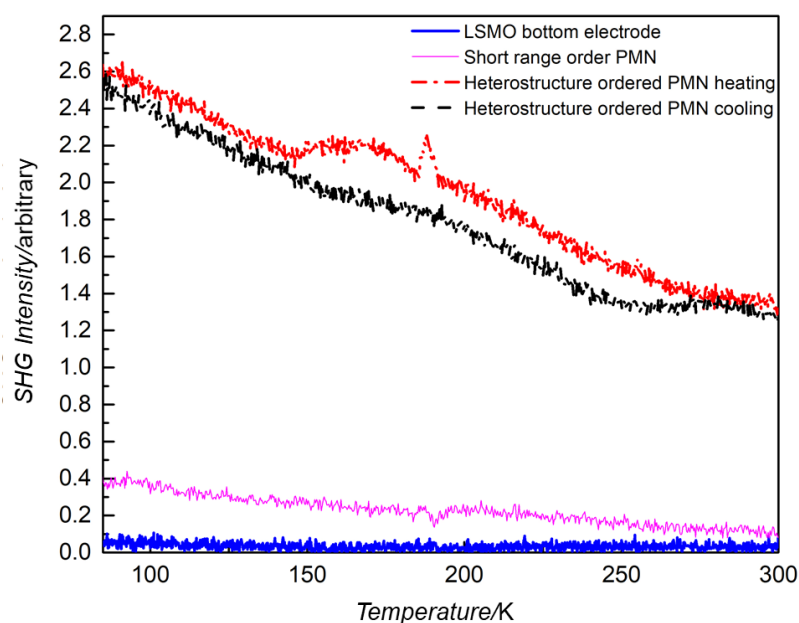
Figure 3-13: Second harmonic generation results for LSMO on STO substrate, short-range-ordered PMN and long-range-ordered PMN heterostructure during heating and cooling cycles

The difference between the short-range and the long-range-ordered PMN films, shown by

the second harmonic and electrical characterization might imply a difference in the percolation of

polar microdomains, with increased ferroelectricity in the ordered case. This work shows that the

degree of relaxor character in thin film PMN can be reduced with increased length scales for the

cation ordering (e.g. when the size of the chemically ordered regions approaches 100 nm) via

engineered growth of heterostructures with alternate layers of $Pb(Mg_{2/3}Nb_{1/3})O_3$ and $PbNbO_3$.

These heterostructures possess some characteristics of relaxor and some of normal ferroelectric behavior. Ferroelectric domains develop in the long-range-ordered films below 140K under zero field cooling conditions. Results on growth and electrical characterization of PMN heterostructures on scandate substrates have been discussed in Appendix B. Similar trends in the temperature dependent dielectric behavior of PMN heterostructure (as a function of ac field and frequency) were observed on the scandate substrates as STO. This indicates substrate does not influence the observed properties in the long-range ordered films.

<div align="center">

Chapter 4

Non-linearity in engineered lead magnesium niobate (PbMg$_{1/3}$Nb$_{2/3}$O$_3$) thin films

</div>

4.1 Introduction to non-linear susceptibility in relaxor ferroelectricity

Small signal dielectric nonlinearities can be used to probe the response of domain walls[64–67] or nanopolar regions[68–71] to oscillating electric fields. This can be a valuable tool in understanding the ferroelectric-relaxor continuum model observed in long range ordered PMN films. In materials containing ferroelectric domain walls with a randomly broad and uniform distribution of pinning centers, the polarization response in the sub-switching regime (E<~1/2 E$_c$; where E$_c$: coercive field) may be approximated by the Rayleigh relation[74]:

$$P = (\varepsilon_{init} + \alpha E_0)E \pm \alpha(E^2 - E_0^2) + \cdots. \qquad \text{(Equation 4- 1)}$$

where P is the polarization, $E = E_0\,sin\,\omega t$ is the applied alternating electric field, ε_{init} is the dielectric permittivity at zero field, and α is the irreversible Rayleigh coefficient; the "+" sign corresponds to decreasing and "-" to increasing field. The above relationship can be expanded into a Fourier series[64] as:

$$P = (\varepsilon_{init} + \alpha E_0)E_0 \sin \omega t - \frac{4\alpha E_0^{\,2}}{3\pi}\cos \omega t - \frac{4\alpha E_0^{\,2}}{3\pi}\left[\frac{1}{15}\cos 3\omega t - \frac{1}{105}\cos 5\omega t + \cdots.\right]$$

<div align="center">

(Equation 4-2)

</div>

The higher harmonic terms are 90 ° out-of-phase with the driving field; as a result, they contribute both to the nonlinearity in the polarization and to hysteresis. This model provides a good description of the response of a number of ferroelectrics[67,77] with mobile domain walls or boundaries of polar clusters. This field dependence of the phase angle of the higher order harmonic permittivity has been used to investigate the presence of Rayleigh-like behavior in $Ba_{0.6}Sr_{0.4}TiO_3$ ceramics[107], by Hashemizedah and Damjanovic. In those ceramics, the phase angles were inconsistent with Equation 2. Instead, the behavior was consonant with harmonic analysis of PMN ceramics above T_{max}, where the polar entities provide a nonlinear, but nearly anhysteretic response[33] as a function of the electric field, implying that the Rayleigh-like analysis cannot be used to fully explain the dielectric response in this regime.

The non-linear dielectric properties are also important in discriminating between existing models for relaxor ferroelectrics, since it is believed that the higher order susceptibilities are more sensitive to the dipolar disorder than the linear parameters[70]. In globally centrosymmetric materials like PMN, the dielectric response between induced polarization (P) and the electric field (E) should be given by the expression:

$$P = \varepsilon_0(\chi_1 E + \chi_3 E^3 + \cdots)$$
(Equation 3)

where χ_1 and χ_3 are the first and third harmonic susceptibilities. There are several conflicting studies on the temperature dependence of the scaled susceptibility parameter a_3 (defined as $a_3 = -\chi_3/\varepsilon_0^3\chi_1^4$) in the vicinity of the static freezing temperature (T_f) of relaxors. In principle, a_3 should distinguish between models in which PMN transforms into a ferroelectric state with nanodomains or diverges into a freezing transition, as in the case of dipolar glass[68].

The most widely accepted model for PMN is the spherical random-bond–random-field (SRBRF) model. In the SRBRF model, Pirc and Blinc assumed that spherical PNRs interact via spin-glass type random exchange coupling, while being subjected to a random quenched internal

electric field.[57,58]. The model predicts a negative χ_3 and a positive a_3 with two extremes: one at the freezing temperature T_f of the spherical glass phase and another at the T_{max}. To date, this prediction has been examined experimentally by a number of groups[55,68,70] for PMN single crystals. Bobnar et al.[68] confirmed the theoretically predicted anomaly of a_3 at T_f (a_3 strongly increases as the temperature approaches the freezing $T_f \sim 220$ K, where ergodicity is effectively broken for undoped PMN single crystal). Glazounov and Dec observed that a_3 continues its monotonic increase even below T_f, ≈ 220 K. A monotonic increase in a_3 would be more in agreement with the ferroelectric background picture of relaxors than with the glassy one. The reported experimental data shows a positive sign of χ_3, which can be explained either by incorporating the effect of the electric field on the interacting polar clusters in the generalized spherical random bond random field model[108] or by including the average polarization of the polar nanoregions in a modified Landau-Ginzburg-Devonshire formalism[70]. The signs and phase of χ_3 and the sign of a_3 have been summarized in Table 4-1 for the Rayleigh model, the modified phenomenological model for relaxors[70] and the SRBRF model. It has been pointed out that many of these seemingly contradictory observations could be due to the fact that the experimental results were obtained in different regions of the electric field-temperature phase diagram[5]. Namely, by cooling the relaxor at an electric field exceeding the critical field E_C, a long-range ferroelectric phase is formed. Thus, the field-history characteristic of the measurement can have a profound effect on the results.

Table 4-1: Summary of signs for χ_3 and a_3 and phase for χ_3 predicted by different relaxor models.

	Sign of χ_3	Phase of χ_3	Sign of a_3
Rayleigh model[77,107]	-	-90 °	+
Modified LGD[70] **phenomenology-based model for relaxors**	+	NA	-
SRBRF model[57]	-	180 °	+
Generalized SRBRF[108]	+	180°	-

There are essentially two ways to characterize the third order non-linear dielectric response χ_3. The most reliable technique involves measurement of the polarization response at 3ω, simultaneously with the linear response at ω at zero field dc bias. The second technique utilizes the static electric field dependence of the linear dielectric constant, where χ_3 is defined as, $\chi_3 = [\chi_1(E_2) - \chi_1(E_1)]/((E_2)^2 - (E_1)^2)$; this can be erroneous due to contributions from a phase transition into a long-range-ordered ferroelectric state near T_f.

Although symmetry should forbid a second harmonic dielectric response in centrosymmetric materials, measurable second harmonic contributions in the polarization response have been reported for centrosymmetric phases of ferroelectric/relaxor crystals and ceramics like 60-40 BST[107], PZN-PT[109], $BaTiO_3$[109], $Sr_{0.61}Ba_{0.39}Nb_2O_6$ etc. This has been attributed to the presence of residual polarization that is the result of a previous application of an electric field and that has not been completely removed by annealing the crystal at a temperature above T_{max} due to presence of micropolar regions or to a finite defect population, leading to local inhomogeneous fields and quadratic dielectric displacement in the material. That is, a second harmonic can appear if the local symmetry is non-centrosymmetric. Alternatively, a second harmonic can also be observed in cases

where mobile charges are trapped on the first cycle of the electric field[110].

It is an open question as to how the level of cation ordering in a relaxor ferroelectric will influence the higher order polarization terms as a function of temperature. In this work, the linear complex dielectric susceptibility was analyzed as a function of temperature and frequency in zero field cooled PMN films with short- and long-range ordering. Additionally, the second and third harmonic displacement charge densities were determined as a function of temperature to assess the influence of chemical ordering on the non-linear dielectric susceptibility. These, along with the phase angles of the higher harmonics, were used to probe the ferroelectric-relaxor continuum phenomenon observed in these films. In particular, of interest was which, if any of the models shown in Table 4-1, described the behavior of these PMN films. The measurements made also track the nonlinearity over a wider temperature range than has been reported previously.

4.2 Experimental procedure

For the second- and third order dielectric harmonics measurements, a sinusoidal ac oscillation was applied using the built-in voltage source of a lock-in amplifier (Stanford Research Inc. SR-830). A low-noise charge amplifier with a scaling factor of 1 V/100pC was used to amplify the output signal of the sample. The charge amplifier showed very little change in amplitude (< 2 %) and moderate phase errors (< 15 °) with a reference capacitor load similar to that of the PMN films, at the highest measured frequency of ~60 kHz (e.g. the 3rd harmonic of the 20 kHz fundamental). Over most of the frequency range, the phase angle was substantially smaller. The resulting voltage from the charge amplifier was detected by the lock-in amplifier for the second and third harmonics, sequentially. In this way, the magnitudes of the higher-order dielectric charge displacement densities were measured as a function of temperature and frequency. The harmonic displacement charge density is defined as $D_n = Q_n/A$, where A is the area of the sample,

D is the induced displacement charge density, Q is the magnitude of the measured charge at the desired frequency, and n is the harmonic order. Similar to the nonlinear dynamic approach adopted by Hashemizadeh et al.[107], the phase of the higher harmonic dielectric measurement was measured to investigate the dynamics of the polar mobile interfaces (such as domains walls or polar cluster boundaries), as well as to validate the Rayleigh-like behavior regime in the ordered sample, as a function of temperature and ac field up to 100 kV/cm at 1 kHz.

4.3 Results and discussion

Figure 4-1 and 4-2 shows the temperature dependence of the real parts of the first ($D_{1\omega}$), second ($D_{2\omega}$), and third ($D_{3\omega}$) harmonic dielectric displacement densities for short and long range ordered PMN thin films, respectively, measured at 15 kV/cm. All three responses showed broad frequency dependent maxima as a function of temperature in the frequency range from 0.5 to 20 kHz. $D_{3\omega}$ is more frequency dependent than $D_{1\omega}$. As reported previously, the short range ordered film shows a larger frequency dispersion in $D_{1\omega}$ compared to the long range ordered film. This is consistent with a higher degree of relaxor behavior in the short range ordered film. Interestingly, the magnitude of $D_{2\omega}$ is comparable to $D_{3\omega}$ in both films and shows substantial frequency dispersion above 200 K. The latter observation is likely to be due to increased conductivity at higher temperatures, with a commensurate increase in trapping of mobile charges.[110]

The $D_{3\omega}$ response has a complex shape with a change in sign, as a function of temperature and frequency. There is a minimum in $D_{3\omega}$ (i.e. the highest negative value) near the permittivity maximum (observed at the highest frequencies), with the values converging back towards zero both at 0K and well above T_{max}. With increasing frequencies in both long and short-range ordered PMN films, $D_{3\omega}$ is more negative. The dispersion in $D_{3\omega}$ is small at T<100 K, and increases in magnitude with temperature, until it reaches 175 K in the case of long range ordered films and 200 K for short

range ordered film. On further heating, the frequency dispersion collapses. Persistence of dispersion up to higher temperature in short range ordered film is consistent with a higher degree of relaxor behavior.
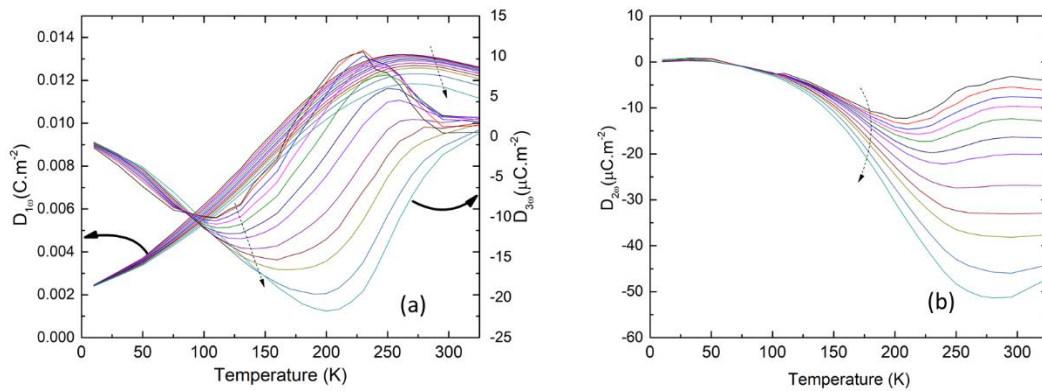
Figure 4-1: (a) Temperature dependence of first order and third harmonic displacement current for zero-field cooled short-range-ordered PMN films as a function of frequency (500 Hz-20 kHz) measured on heating (b) Temperature dependence of second harmonic displacement current for short-range-ordered PMN films as a function of frequency measured on heating. The dotted arrows indicate increasing frequency (from 500 Hz -20 kHz). All measurements were done at an electrical field of 15 kV/cm.
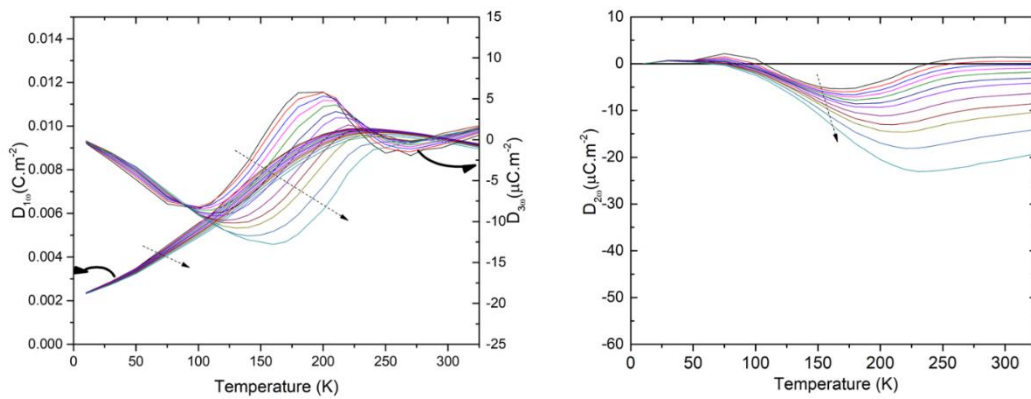
Figure 4-2: (a) Temperature dependence of first order and third harmonic displacement current for zero-field cooled long-range-ordered PMN films as a function of frequency (500 Hz-20 kHz) measured on heating (b) Temperature dependence of second harmonic displacement current for long-range-ordered PMN films as a function of frequency on heating. The dotted arrows indicate increasing frequency (from 500 Hz -20 kHz). All measurements were done at an electrical field of 15 kV/cm.

To develop additional insight into the mechanisms responsible for this behavior, the higher harmonic polarization was measured as a function of temperature and the amplitude of ac electric field for PMN films with cation ordering at different length scales. Figure 4-3 (a)-(d) illustrates the phase of third harmonic contribution as a function of temperature. At low temperatures, after a certain threshold electric field, the phase angle of the 1st harmonic is ~0°, while that of 3rd harmonic is -90°, similar to that observed in PZT thin films[77]. This is consistent with Rayleigh-like hysteretic responses of mobile interfaces like domain walls or polar cluster boundaries. The observation of Rayleigh-like behavior at low temperatures is consistent with the drop in the magnitude of D$_{3\omega}$ below 100K, as the motion of domain walls (or cluster boundaries) is thermally activated. This might also account for the relatively modest frequency dependence, with the largest response occurring at the lowest frequencies.

At temperatures above ~180 K, the 3rd harmonic phase angle deviates towards 0 or -180°, as shown in Figure 4-3 (c)-(e). The threshold field (defined as the minimum electric field for observing Rayleigh response where the phase angle is close to 90°) was observed to decrease with increasing temperature till 180K, with increasing Rayleigh-like behavior. This corroborates well with the peak in the irreversible Rayleigh coefficient α at 150 K as reported elsewhere. At room temperature, the 3rd harmonic angle is close to -180°, representing an-hysteretic behavior similar to that reported in bulk PMN. This means that the dielectric behavior at room temperature is governed by polar nanoregions, whose dynamics cannot be explained using the Rayleigh law. This further supports the continuum of ferroelectric and relaxor behavior with increasing temperatures. This may occur as a result of increased relaxor behavior due to contributions for polar nano-region, as proposed by the spherical random bond random field model.
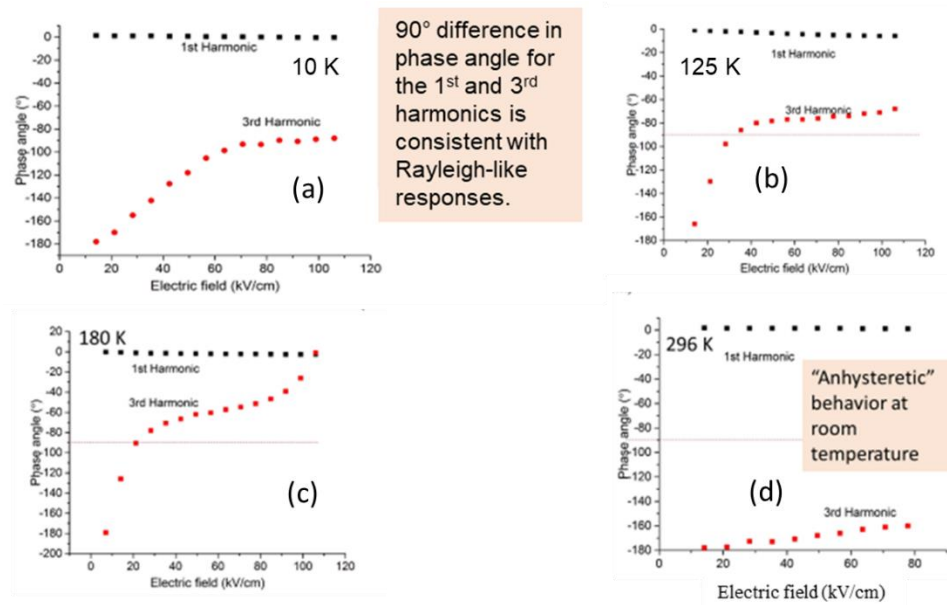
Figure 4-3: Phase angle for the 1st and the 3rd harmonics of the polarization at 10K (a)-(d) Hysteretic to anhysteretic transition in long-range-ordered PMN as demonstrated by 3rd harmonic phase with increasing temperatures at 125 K, 180 K and 296 K respectively.

Figure 4-4 (a)-(e) shows the ac field dependence of the first (χ_1), second (χ_2), third order susceptibilities (χ_3) and scaled parameter a$_3$ as a function of temperature, measured at 1 kHz for the long-range-ordered PMN thin films. The linear susceptibility displays a broad maximum as a function of temperature. The non-zero second harmonic observed in Fig 4-4(b) is largest below 150 – 170 K, consistent with previous observations of long-range ferroelectric ordering at these temperatures[12]. The magnitude of χ_2 remains non-zero, but decreases above this temperature, consistent with the possibility of local polarization in the unpoled heterostructure above 170 K. In this work, the difference in the maximum/minimum temperatures for χ_1 and χ_3 is larger than that reported by Dec.[70]

As shown in Figure 4-4(c), at the lowest measured field (which is below the threshold field at low temperatures, but well in the Rayleigh regime above ~120K), χ_3 is mostly negative, with a change in sign at temperatures above 200 K. At this field, the temperature where χ_3 has its largest

negative magnitude corresponds well with the temperature at which the irreversible Rayleigh coefficient α has its maximum value, as reported elsewhere[12]. The change in sign shifts towards lower temperatures with increasing ac field. The fact that χ_3 is more positive at high AC electric fields implies that domain wall contributions cannot be responsible for the sign change, as Rayleigh contributions should produce a negative χ_3. The positive χ_3 is consistent with prior reports by Dec for PMN ceramics. A transition from a non-hysteretic to hysteretic behavior is seen with lowering temperatures. This suggests that the nonlinear properties must lie somewhere on a continuum between normal and relaxor-like ferroelectrics.

A similar trend with ac field is also reflected in the scaled parameter a_3, as seen in Figure 4-4(d). Over most of the observed temperature range, a_3 is small and negative. At lower temperatures, a_3 becomes positive; the temperature at which it does shifts lower with increasing electric field. Neither χ_3 nor a_3 display any extremes in the vicinity of the freezing temperature T_F, as predicted by the random bond random field model. The positive χ_3 is in accordance with a Landau Ginsburg Devonshire phenomenological model[71] or the generalized SRBRF model.
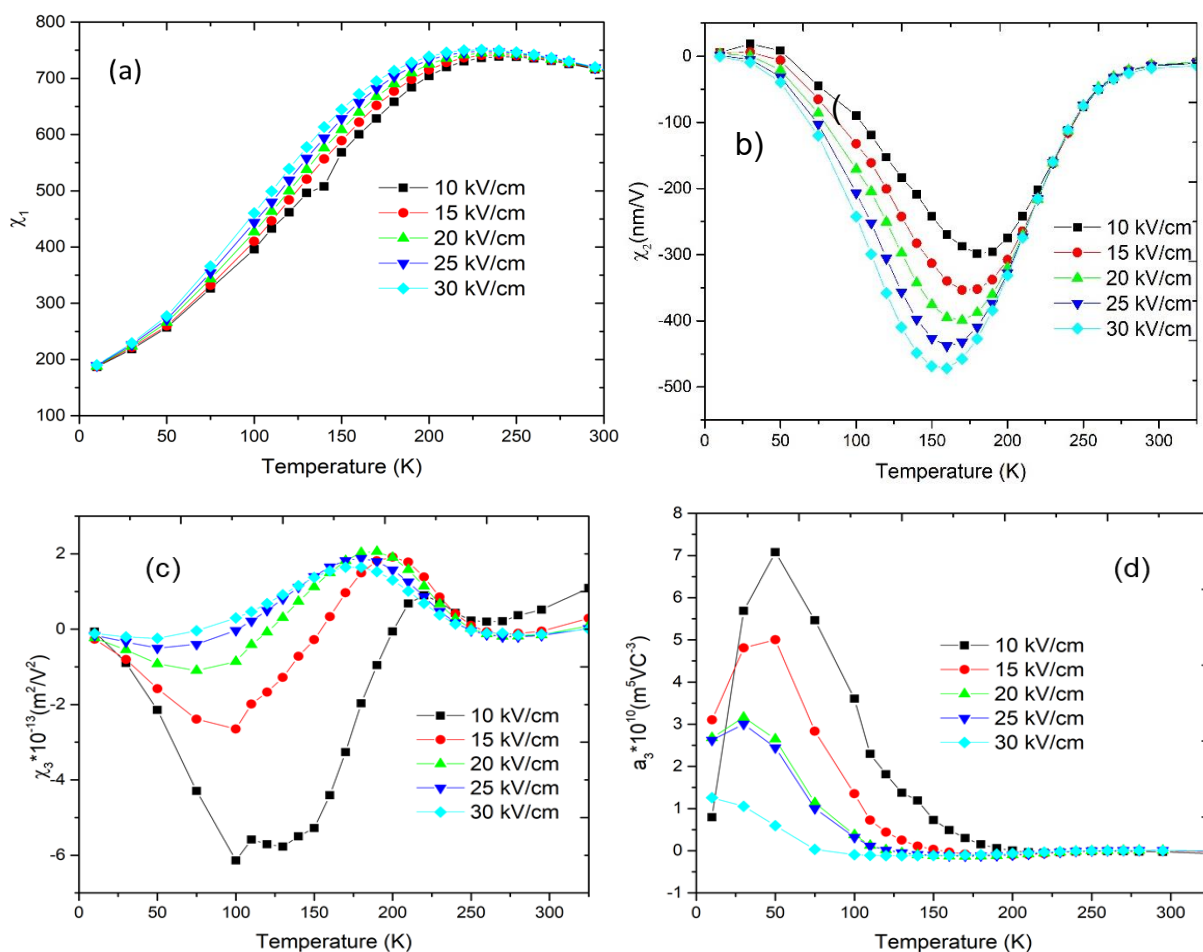
Figure 4- 4: Temperature dependence of (a) first order susceptibility, (b) second order susceptibility, (c) third order susceptibility, (d) scaled susceptibility parameter a_3 for long-range-ordered PMN films as a function of electric field (5-30 kV/cm) measured during a heating cycle
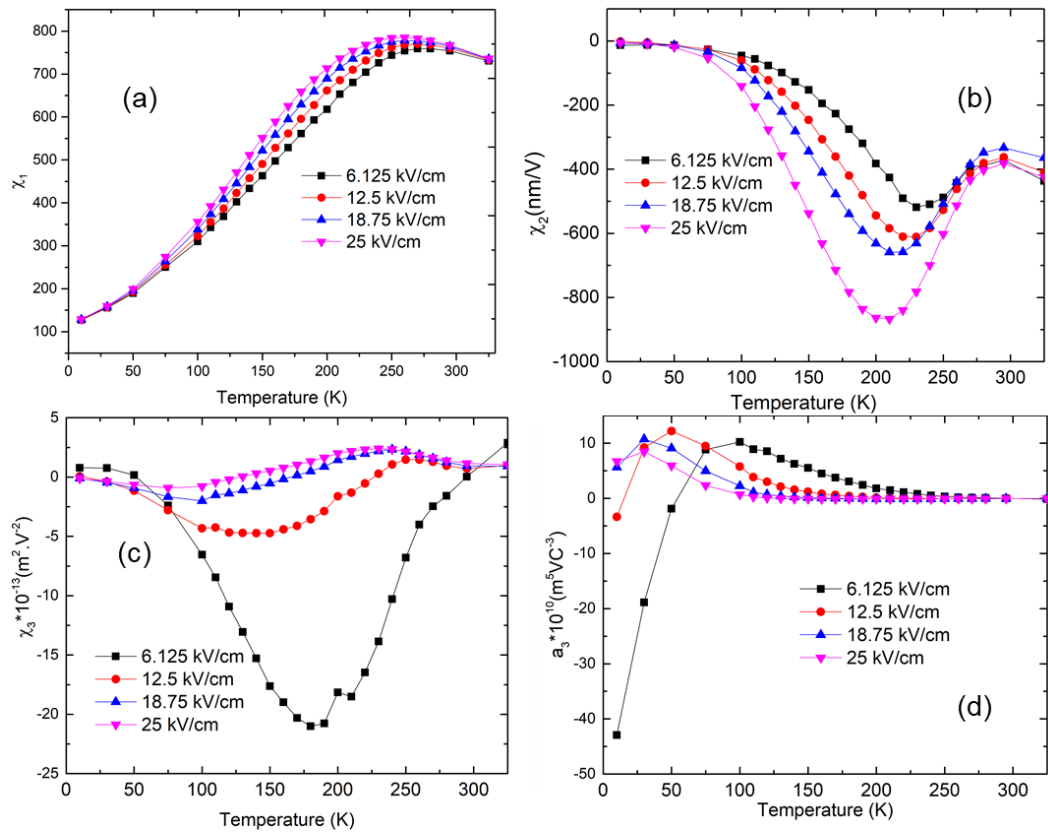
Figure 4-5: Temperature dependence of (a) first order susceptibility, (b) second order susceptibility, (c) third order susceptibility, (d) scaled susceptibility parameter a_3 for short-range-ordered PMN films as a function of electric field measured during a heating cycle

To compare to the long-range-ordered films, Figures 4-5 (a)-(d) show the first, second, and third order susceptibilities and scaled parameter a_3 as a function of temperature, measured at 1 kHz for the short-range-ordered PMN thin films. While the magnitudes of χ_1 are comparable for the short- and long-range-ordered films, the nonlinearity observed in the short-range-ordered films is an order of magnitude higher than that of the-long-ranged ordered films. This is presumably a consequence of the higher degree of relaxor character in the short-range-ordered films. If the origin of this is Rayleigh-like responses due to polar cluster boundaries, then this would suggest that at least some of the boundaries move reversibly, such that the contribution to χ_3 but not to the irreversible Rayleigh coefficient α. There is also a shift in T_{max} for χ_3 towards

higher temperatures as a function of reduced ordering. Interestingly, unlike long-range-ordered films, there is an additional change in sign in a_3, as it begins to diverge at lower temperature.

Figure 4-6 shows the summary of the dielectric, SHG and third harmonic susceptibility phase for a long-range-ordered PMN film. This suggests that below 150K, the long-range-ordered film behaves more like a normal ferroelectric. However, with increasing temperature, relaxor character dominates due to loss of long-range ordering with heating. As a function of temperature, the phase angle of χ_3 moves from showing hysteretic (near -90°) to anhysteretic behavior (near -180°) behavior. The phase angle of the third harmonic of polarization, as function of temperature shows a dependence on applied electric field. Interestingly, the phase angle plot is closer to 90 ° over a wider temperature range at higher electric field. At lower fields, the slope becomes steeper and an-hysteretic at very low and room temperature.
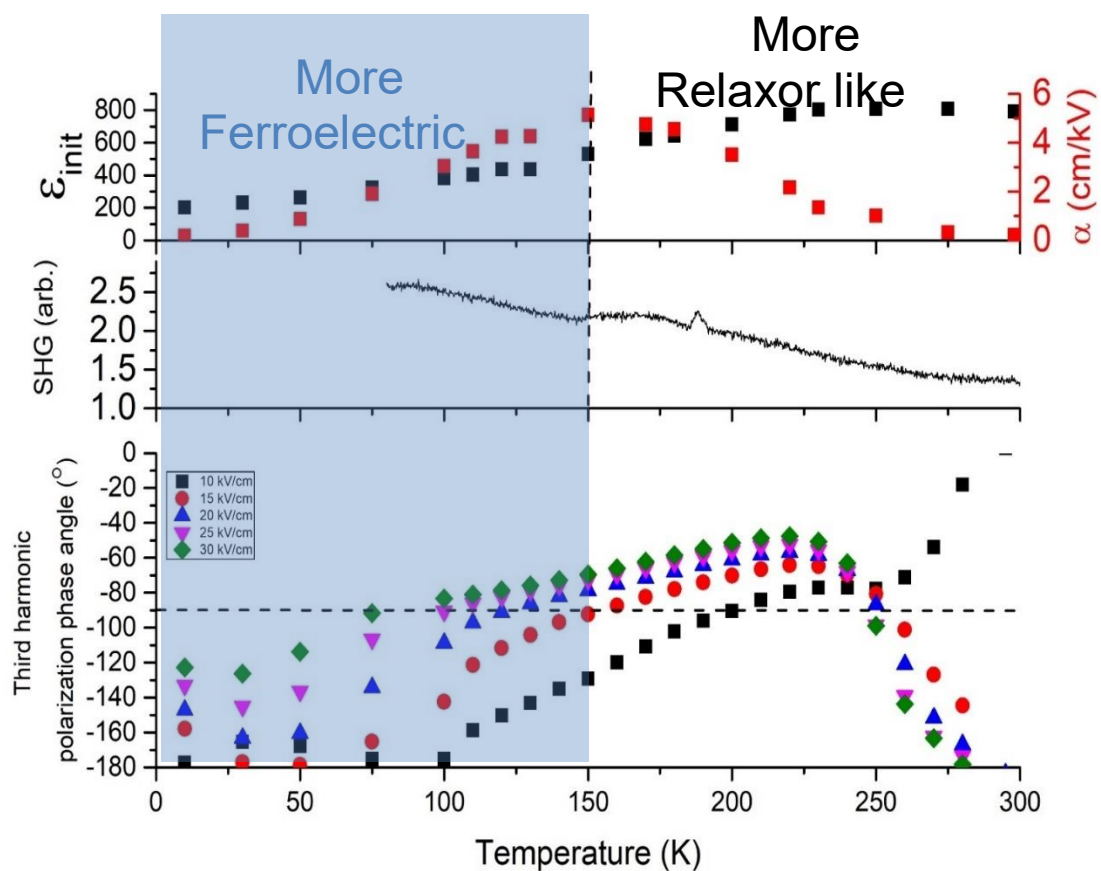
Figure 4-6: Summary of nonlinearity data from (a) Rayleigh (b) Second harmonic optical generation intensity (d) third harmonic polarization phase angle as a function of temperature and electric field for the long-range-ordered PMN film

Chapter 5

Quantitative and high spatial resolution d_{33} measurement of piezoelectric bulk and thin films

A major portion of this chapter has been reproduced from: Smitha Shetty, Jung In Yang,

Joe Stitt, and Susan Trolier-McKinstry, "Quantitative and high spatial resolution d_{33}

measurement of piezoelectric bulk and thin films," Journal of Applied Physics 118, 174104

(2015).

5.1 Introduction

Substrate declamping can have a profound impact on usage of piezoelectric thin films for several actuator based applications - one such example is the high speed, low power piezoelectric transistor[10] proposed by IBM to address the challenges posed by stalled clock speeds in complementary metal oxide semiconductor transistor (CMOS) technology[9]. This approach relies on the high strain generated in nanostructured piezoelectric films to actuate a piezo-resistive switch element. There is, therefore, a growing need to develop high accuracy and high-resolution metrology for characterization of patterned piezoelectric thin films.

In the case of a perfectly rigid and incompressible electrode/piezoelectric film/electrode/ substrate configuration (i.e. no flexure of the underlying substrate), the formulation by Lefki and Dormans[111] describes the effective value of the converse $d_{33,f}$ coefficient for continuous films measured by probing the motion of the top surface of the sample. The effective value is related to the unclamped d_{33} and the elastic and piezoelectric constants of the substrate and the film, based on the mechanical boundary conditions. In practice, for typical substrates and electrode diameters, the

surface displacement is dominated by substrate bending[112]. If this is not correctly accounted for, erroneously large apparent piezoelectric coefficients result. Local substrate bending effects are reduced for patterned films with decreasing aspect ratio (defined as the ratio of feature width to film thickness)[113]. Lepadatu[114] et al. demonstrated negligible substrate bending for top electrode diameters of <100 μm for 100 nm thick epitaxial $PbZr_{0.2}Ti_{0.8}O_3$ grown on Nb doped STO substrates measured using a scanning laser vibrometer. In addition, recent work by Steward[115] et al. have suggested that substrate bending can be accounted for by measuring the step differential at the electrode edge for large electrode diameters. This would require newer metrology enabling high spatial resolution piezoresponse measurement along the electrode edge. For electrode sizes smaller than the film thickness[116,117], there is an error introduced in displacement measurements due to compression of the substrate as the piezoelectric is actuated. This will reduce the surface displacement, and so will yield an underestimation of the true film $d_{33,f}$. This error is most pronounced when the contributions of substrate bending are reduced (e.g. at small electrode sizes). For applications that require knowledge of the surface displacement however, this underestimated value is the most appropriate one.

Current $d_{33,f}$ thin measurement techniques include optical techniques like homodyne interferometry (single and double beam laser interferometers DBLI)[112,118–124] and heterodyne Doppler shift interferometry (scanning laser vibrometer)[114,125,126] for global measurements, atomic force microscopy based techniques like scanning piezoresponse force microscopy (PFM)[127] for local measurements, scanning tunneling based measurements[128] and direct techniques like the pneumatic pressure rig[129], as summarized in Table 5-1. Though interferometry-based techniques are accurate, with vertical resolutions ranging between 0.01-1 pm, they are spatially limited by the width of the laser spot size (usually >50 μm). This technique is sensitive to vibrations, thermal drift of the sample, quality of the reflecting sample surface and refractive index variations[130,131] along the optical path of laser. In addition, DBLI measurement requires critical alignment of the two

beams to account for substrate bending, which gets complicated for smaller focused beam widths. Also, these measurements cannot be assessed independently on an opaque substrate (the backside of the substrate must also have a very good reflectivity). One can always make a measurement at excellent spatial resolution, but the result is not necessarily a measurement of the piezoelectric properties of the film, since flexure-induced errors cannot be completely compensated. Sivaramakrishnan[116] et al. have demonstrated that stress induced substrate thickness changes which cause variations in $d_{33,f}$ (as a function of electrode diameter and elastic properties of the substrates) are an artifact of the simply supported sample mechanical boundary condition and relative displacement between the top and bottom surfaces of the sample. This may limit the application of the DBLI to accurately determine the $d_{33,f}$ for finely subdivided patterns. Piezoresponse force microscopy (PFM) is the most commonly employed measurement technique with high lateral resolution (~10 nm). Although the lateral resolution is outstanding, the tool is often reported to have vertical resolution errors of ~15 - 40%[132,133]. These errors are attributed to the difficulty in calibration owing to ill-defined and inhomogeneous field distribution at the tip-material interface[132,134], the contact mechanics of the tip with the sample [135–137], flexure in samples with large area electrodes, need of band excitation mode to address varying contact resonance frequency of grains in polycrystalline materials[138], and variation in the apparent d_{33} from the stress applied by the tip to the film surface[136].

This objective of this work is to describe a Mirau interferometric microscope approach, intended to bridge the gap between the semi-quantitative nature of PFM and the low lateral resolution of double beam laser interferometer. Previously, Mammano[139] et al. built a Michelson based interferometric microscope to study sub-micron vibrations in cochlear cells; however the tool sensitivity was limited to 0.1 nm. Also, the non-contact optical profilometer microscope[140] has restricted sub-nanometer resolution due to the poor coherency of the white light source and the relatively low signal to noise ratio of the charge coupled detection scheme. Alternately, the single

beam interferometer microscope developed in this work achieved improved vertical sensitivity (in the picometer range) by using a lock in phase detection scheme, in addition to lateral resolution of $2\,\mu$m. Though substrate declamping has been modeled and experimentally verified as a function of geometry in thin $PbZr_{0.2}Ti_{0.8}O_3$ films using piezoresponse force microscopy[89], this work demonstrates the first quantitative study, with clear indication of increased response along the sidewall of the film. The following sections detail the construction and calibration of an interferometric microscope and compares results on piezoelectric bulk and continuous film samples with a commercial AixACCT^{TM} double beam laser interferometer. This work also demonstrates quantitative $d_{33,\,f}$ measurements on small piezoelectric features, based on observed reduction in substrate bending with decreasing electrode size in continuous films. The single beam approach can be used in a scanning mode to account for residual substrate bending contributions by measuring the deflection of the specimen on and around a sub-divided feature.

Table 5-1: Comparison of $d_{33,f}$ techniques for piezoelectric thin films.

| Detection approach | Ref. | Resolution | | Potential |
		Lateral	*Vertical*	**Error sources**
I. Optical interferometer				
a. Single beam	26,32,33,35	>50 μm	0.01 pm	Substrate bending contribution
b. Double beam	26,34,36,37,38	> 50 μm	0.02-1 pm	Global response, reduced sensitivity due to increased optical beam length (sensitivity varies as a function of bandwidth and time constant of the lock in amplifier)
c. Scanning laser Doppler vibrometer	28,38,39	> 5 μm	1 pm	Substrate bending contribution
II. Piezoresponse force microscopy	46-51	10 nm	1 pm	Quantification error due to ill-defined field, tip-film contact mechanics and/or sample flexure
III. Scanning tunneling microscopy	42	> 1 nm	5 pm	Ultra-thin top electrode layer for tunneling, sensitive to surface corrugation
IV. Pneumatic pressure rig	43	> 1 mm	-	Inflated $d_{33,f}$ due to in plane stress contributions from mechanical boundary conditions or surface friction imposed by the O-rings

5.2 Experimental procedure

5.2.1 *Construction of the optical interferometer system*

The instrument configuration is based on a modified Mirau interference detection technique, incorporating the optical components in a custom-built microscope schematically shown in Figure 5-1. An Axio Imager Z2 Vario microscope head (Carl Zeiss Microscopy GmbH, Jena, Germany) was chosen due to the ease in interfacing the laser to generate interference fringes, while simultaneously enabling white light for viewing. Polarized light from a 2 mW, 633 nm wavelength stabilized He-Ne laser (JDS Uniphase corporation, Milpitas, CA) is aligned to a polarization maintaining single mode fiber patch cable with antireflection coating (model: P1-630PM-FC-2, Thorlabs, Newton, NJ) using a fiber port coupler (model: PAF-X-5-B, Thorlabs, Newton, NJ) with 60% coupling efficiency. Laser output from the fiber cable is collimated to ~8 mm diameter using an air spaced doublet collimator (model: F810FC-635, Thorlabs, Newton, NJ). In order to obtain a 2 μm diffraction limited spot size for fine spatial resolution, laser beam focusing is achieved using a Galilean telescope setup (50 mm plano convex lens in series with 15 mm bi-concave lens) housed within a 1" tube assembly, external to the microscope. A custom-built slider (Desna Laboratories Inc, NY) housing a reflective mirror positioned at 45° to the laser path was placed inside the auto-alignment port of the microscope to direct the laser to the reflective turret housing the microscope objective. A 20x, 0.4 NA, 4.7 mm working distance Mirau interferometric objective lens (Nikon), routinely employed for white light optical profilometry[140], was chosen for this application. This objective attachment incorporates a 50/50 beam splitter which divides the incoming beam into the measuring beam (towards the sample) and the reference beam as shown in **Error! Reference source not found.**b. When the sample is in focus, the optical path lengths of the measurement and the reference beams are identical. In this position, white light interferometry between the two beams generates a planar bright and dark interference fringe pattern while laser interferometry generates

a bright spot at the center of the spherical fringe pattern.

The stage assembly consists of a x-y manual stage for the Zeiss microscope with a 25 mm travel range and a 1 µm lateral resolution (model: M-545.2MZ, Physik Instrumente L.P., Auburn, MA) and a 13 mm travel manual z-axis positioning system (model: MVS005/M, Thorlabs, NJ). Fine resolution z displacement (~1 nm) required for the interferometer calibration was achieved by mounting a piezoelectric controlled nano-Z slide scanner system (model: P-736, Physik Instrumente L.P., Auburn, MA) on the manual stage assembly. An optically flat aluminum plate with holding clips was fastened on the nano-Z stage to securely fix the sample. After interference, the output laser beam propagates along the optical column of the microscope, and is then split by a 90/10 beam splitter (Chroma Technology Corp, VT). 10% of the beam is directed to the camera (model: AxioCam ICc1 R4, Carl Zeiss Microscopy GmbH, Jena, Germany) while the bulk of the output beam is monitored using a photo-detector mounted on a coupler. A reverse-biased silicon photodiode detector (Model: Det 36 A, Thorlabs, NJ) was originally used for intensity measurement. However, this provided a limited interferometer bandwidth (~120 Hz). The photodiode detector was thus replaced by a photomultiplier tube (Model: H5784-02, Hamamatsu Photonics, Japan) with an amplifier feedback circuit for enhanced sensitivity (gain of ~10^5 V/A) and improved frequency response (up to 20 kHz). A 50 $\Box$m precision pinhole (model: P50S, Thorlabs, NJ) for spatial filtering was aligned using an x-y translation stage, before the photomultiplier tube. The photomultiplier tube was fiber coupled to the interferometer in order to prevent accidental saturation of the module from ambient light. The photomultiplier output was phase locked with the actuating electric field on the piezoelectric (model: waveform generator 3390, Keithley, OH) using a lock in amplifier (Model: SR-850 DSP, Stanford Research Systems, CA) to obtain reasonable signal to noise ratio for sub coercive field piezoelectric measurements.

The interferometer microscope head is anchored by a vibration damping mounting frame

(Desna Laboratories Inc., NY) for improved dynamic rigidity. **Error! Reference source not found.**c depicts the interferometer setup. The system is isolated from ambient light and temperature fluctuations using an enclosure. The system is placed on an air table (Newport, isolator series) in a low-noise environment for improved resolution.

5.2.2 Interferometer calibration

The electric field-induced thickness change in the piezoelectric material is small (1-1000 pm), relative to the measuring wavelength. In order to detect this strain, the path length of the measurement beam reflected from the sample surface needs to be monitored relative to the reference beam in the Mirau objective. This difference is measured as an intensity change in the center of the interference pattern. To achieve the highest sensitivity (change in intensity with optical path length difference), the single beam interferometer is stabilized at an active operating quadrature point (where the path length difference between the measuring beam and the reference beam is one-fourth the laser wavelength). The phase of the measuring laser beam is modulated about this quadrature point by the alternating excitation field (seen by the sample). In this case, the surface displacement amplitude is linearly proportional to the resulting interference intensity change (less than 1% error for thickness changes less than 13 nm)[120]. Note that, the sample displacement ΔL needs to be incorporated twice, since the path length of the measuring beam is changed twice, before and after the reflection. This displacement ΔL (corresponding to V_{out} measured by the photodetector about the quadrature point) can be calculated by equation (1)[120] :

$$\Delta L = \left(\frac{\lambda}{2\pi}\right)\frac{V_{out}}{V_{p-p}} \qquad\qquad (1)$$

where λ is the wavelength of the measuring beam and V_{p-p} is the peak to peak voltage change corresponding to a full fringe width $(I_{max} - I_{min})$ at the center of the interference fringe.

Interferometer calibration required the following key steps: (1) determination of the quadrature point for maximum sensitivity, (2) determination of the minimum detectable sample displacement using a standard and (3) comparison of the measured surface displacement on known samples with existing measurement techniques. The quadrature operating point was determined by measuring the intensity change corresponding to the full fringe displacement at the center of the interference pattern, using an oscilloscope. This was achieved by first bringing the sample in focus (ensured by white light interferometry) and then translating the nano piezo z stage by 158 nm (the distance travelled by the light is twice that by the z stage). Stabilization of the quadrature point was achieved via continuous monitoring of the static light intensity at the quadrature point using the oscilloscope and moving the nanopiezo stage to compensate for the intensity changes due to external vibrations.

To determine the minimum detectable deflection, an x-cut quartz crystal with known d_{11} of 2.3 pm/V[141] was used to measure the sensitivity and linearity of the interferometer at low excitation field. Both first generation {001} oriented single crystal $0.67PbMg_{0.33}Nb_{0.67}O_3$-$0.33PbTiO_3$ and bulk polycrystalline PZT-5A (TRS Technologies Inc., State College, PA) were employed for the interferometer calibration. Bulk samples were poled at 10 kV/cm for 5 minutes at room temperature in an oil bath, prior to measurements. These samples had a rough top surface with 100 nm thick Au electrodes. To reduce the scattering due to roughness, a polished nickel foil was glued on the top surface. In the case of thin films, 1 μm thick {111} oriented $PbZr_{0.3}Ti_{0.7}O_3$ with 1% Mn, grown by chemical solution deposition on a platinized silicon substrate (details of film synthesis given in reference[142]) with large top Pt electrodes (10 mm x 1.5 mm) was used to demonstrate the role of substrate bending for different mechanical sample mounting conditions. A 0.93 μm thick $PbZr_{0.52}Ti_{0.48}O_3$ film with random orientation, grown via chemical solution deposition on platinized silicon substrates (details on the thin film preparation are given in reference[143]) was used to illustrate the dependence of substrate bending on the capacitor electrode area. The sample strain measured via the single beam interferometer was also compared with the

quasistatic direct piezoelectric measurement using the Berlincourt d_{33} meter (APC International Ltd., PA) and large signal displacement measurement using aixACCT double-beam laser interferometer (AixACCT Systems, Aachen, Germany) for five families of samples. In order to enable measurements on laterally scaled piezoelectric films, a series of features with equal surface areas but varying perimeter were patterned in the 500 nm thick sputtered randomly oriented $PbZr_{0.52}Ti_{0.48}O_3$ films with 1% Niobium (sample preparation detailed in the supplementary materials)[13]. The geometries consisted of antennae-like structures, with a small contact pad (40 x 40 μm^2), and a short central stub with arms as shown in Figure 5-2, to ensure minimal strain contributions from substrate bending. These arms were varied in width (5 μm and 10 μm), offering different degrees of substrate clamping. These films had a permittivity of ~900, a dissipation factor less than 4% and were slightly imprinted. The samples were poled at four times the coercive voltage ($V_c = 3.1$ V) for 15 minutes at 25°C and 150°C, before each measurement.

(a)

CCD camera

LED lamp

Photo-detector

Lock-in Amplifier

Fiber optic cable

He-Ne Laser

Collimator + Gallilean telescope setup

Mirau interferometric lens

SGN | Sample | GND

Piezoelectric Z stage with X-Y micrometer control

(b)

To photomultiplier tube

Dichroic mirror

Reflective insert

Collimated light from fiber coupled laser

Beam splitter in the reflective turret

Telescope setup for beam sizing

Mirau Objective

Reference mirror
Beam splitter

Sample

(c)

50 μm aperture housed on x-y translation stage

Vibration damping mounting frame

Fiber optic cable connection to the photomultiplier tube and lock in amplifier

Mirau Interferometry lens

Reflective insert

Nanopiezo-z stage

Manual x-y-z stage

Fiber coupled laser

Micromanipulators for electrically probing the sample

Figure 5-1: (a) Schematic of the spatially resolved single beam laser interferometer microscope. (b) Illustration of the beam path in the interferometer. (c) Picture of the interferometer setup.
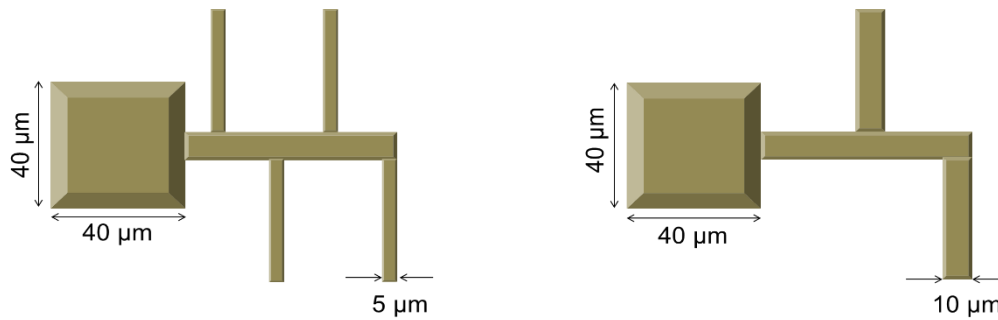
Figure 5-2: Antenna-like geometry of equal area but with varying perimeter used for laterally scaled measurements.

5.3 Results and discussion

5.3.1 Interferometer system resolution

The theoretical lateral resolution for the interferometric microscope was calculated to be ~0.96 μm, based on the Rayleigh limit. This was experimentally evaluated by measuring the intensity distribution of the laser spot image on a highly reflective Pt mirror surface, as a function of spatial position. The spatial conversion was achieved by determining the pixel: distance conversion ratio for lithographically defined standard patterns. The central beam spot image was captured using a neutral density filter (with optical density of 3) to prevent the saturation of the CCD camera. Figure 5-3 depicts the grayscale intensity plotted vs. lateral distance using ImageJ^{TM} software for the inset image. The peak width for the central spot was observed to be ~ 2-2.2 μm. The spatial sensitivity can be further enhanced by switching to a UV laser diode and higher numerical aperture objective.

Large signal d_{11} measurements on the X-cut quartz crystal were used to determine the vertical sensitivity. As indicated in Figure 5-4, a linear variation of displacement was observed as a function of driving ac amplitude at 1 kHz. The noise floor, corresponding to the smallest detectable signal was measured to be ~1 pm. These tests used an averaging time constant of 30 sec for the lock in

amplifier. The slope of the displacement vs. voltage (average d_{11}) for quartz was measured to be 2.1 ± 0.14 pm/V, close to the reported value of 2.3 pm/V[141]. This was further corroborated by a double beam interferometer measurement with V_{ac} amplitude of 10 V at 1 kHz (average d_{11} ~1.8 ± 1.4 pm/V).
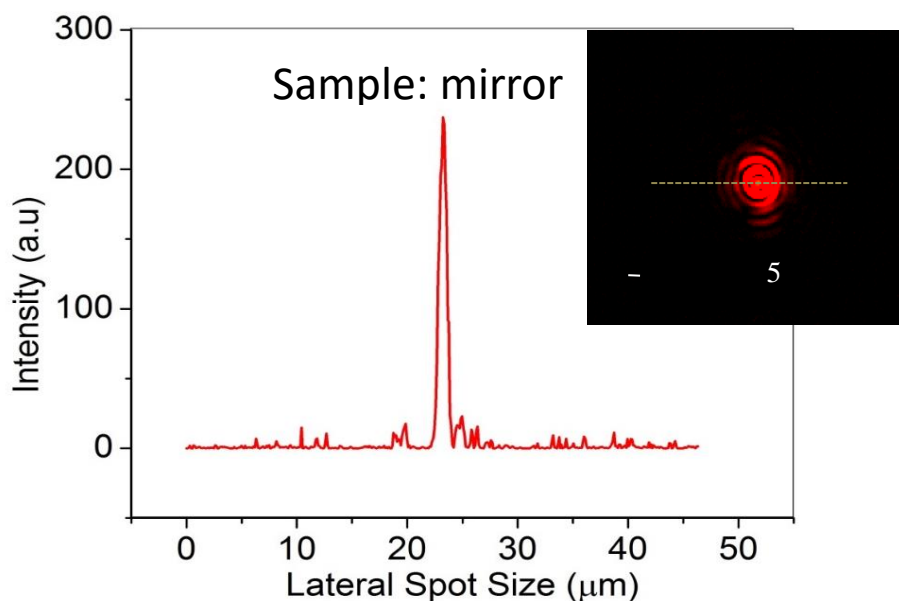
Figure 5-3: Determination of spatial resolution of the single beam interferometer using a Pt mirror sample: central laser spot size measured by plotting the grayscale intensity values as a function of laser spot position along the gray dotted line for the inset optical image showing mirror surface in focus.
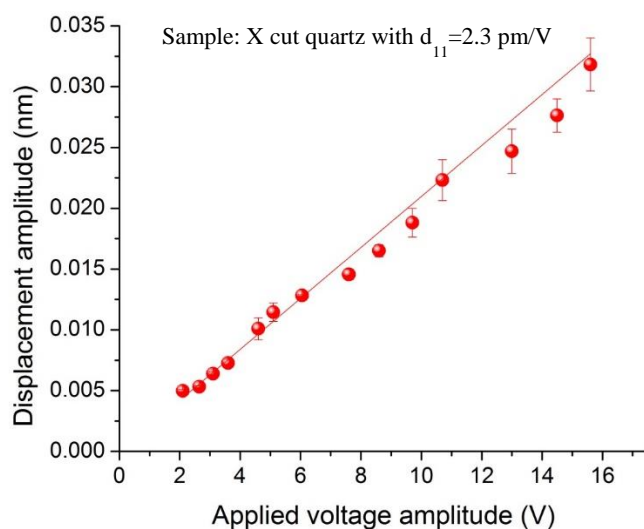
Figure 5-4: Determination of vertical resolution of the single beam interferometer using a X-cut quartz sample

The frequency response of the single beam interferometer illustrated in Figure 5-5 shows the amplitude (in mV) and phase response as a function of frequency of the excitation voltage (set at 10 V_{p-p}) for the single crystal PMN-PT. With the applied field along the poling direction, the phase shift between the measuring field and displacement was observed to be less than 10°. The operating regime for the interferometer was found to be ~2-20 Hz and 430 Hz-2 kHz. This response is affected by electrical resonances (artifacts associated with line voltage observed at 60 and 120 Hz), mechanical resonances of the interferometer stage assembly and the bandwidth of the photomultiplier tube.
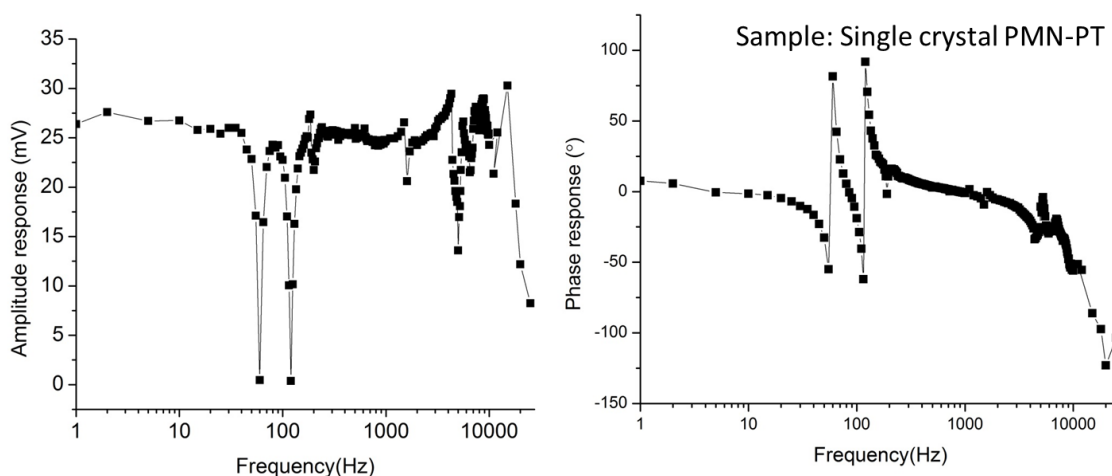
Figure 5-5: Frequency response of the interferometer showing both amplitude and phase variation on single crystal PMN-PT.

5.3.2 Piezoelectric measurement on bulk samples

The piezoresponse data for single crystal PMN-PT and polycrystalline PZT-5A ceramic, as a function of electric field are plotted in Figure 5-6. The variation of the sample displacement in the direction of the applied field is observed to be linear at low applied field. These results showed

reasonable agreement (within 3%) with the commercial DBLI response, which is expected due to absence of sample bending at the operating frequency. The d_{33} values have been summarized in Table 5-2 and compared with the data measured using the Berlincourt technique. The piezoelectric response of the PMN-PT crystal assessed via the Berlincourt technique is found to be ~20% higher in comparison to interferometry technique. This artifact can be attributed to the stress sensitivity of PMN-PT, inflating its d_{33} coefficient.
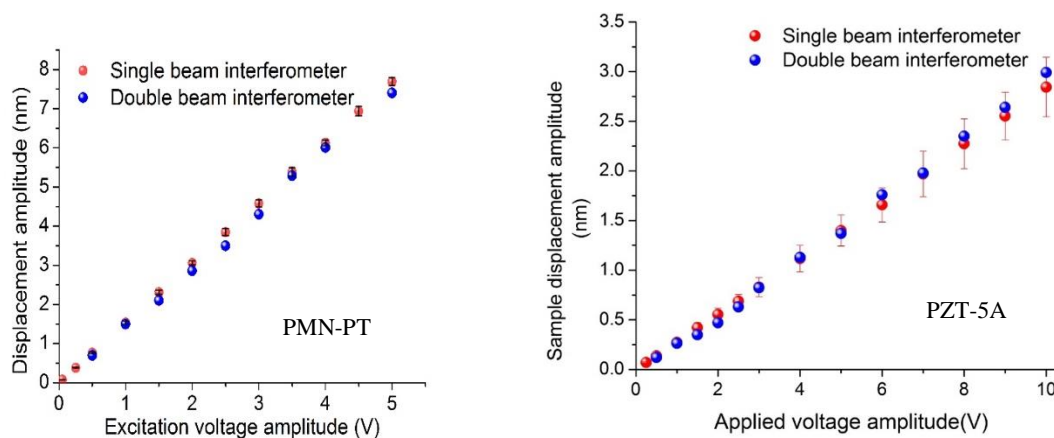
Figure 5-6: Large signal sample displacement for single crystal PMN-PT and PZT-5A measured at 1 kHz using single beam and double beam laser interferometer.

Table 5-2: Summary of comparative d_{33} measurement using Berlincourt, double beam laser interferometer and single beam laser interferometer on single crystal PMN-PT and polycrystalline PZT bulk.

Material	Berlincourt (pm/V)	DBLI (pm/V)	Single beam (pm/V)
PMN-PT	1700-1800	1501± 20	1537±14
PZT-5A	303±36	289 ± 28	280± 29

5.3.3 Piezoelectric measurement on films

The field-induced surface displacement was measured to be large (in the nm range) in the case of large electrodes (10 mm x 1.5 mm) on continuous 1 μm $PbZr0_{.3}Ti_{0.7}O_3$ film sample on a mechanically free-standing substrate, as observed in Figure 5-7. Large signal measurements were made using a sinusoidal signal (amplitude=2.5 V) superimposed on V_{dc}=3V, maintaining the polarization in the same direction as the poling field. This inflated response was due to substrate bending, as is corroborated by the observed 180° phase difference between the excitation field and the measured sample displacement. The sample was next glued to a thick metal block using polyacrylate. As shown in Figure 5-7, there was a substantial reduction of the sample displacement (1-2 orders of magnitude), and the generated strain on the electrode was in phase with the applied field. Additionally, the strain was higher along the edges (partially declamped boundary) as compared to the electrode interior. However, the relatively small negative displacement measured 250 μm away from the right electrode edge still indicated the presence of substrate bending in the measured piezoresponse. This demonstrates the dominance of bending for continuous films with large area electrodes, while adopting d_{33} measurement technique involving scanning only the top surface displacement.

In order to understand the influence of electrode size on substrate bending in continuous $PbZr_{0.52}Ti_{0.48}O_3$ films, the piezoresponse was measured in two regions: at the electrode center and ~20 μm away from electrode edges. The magnitude and phase of the surface displacement measured outside the electrode area, reflecting substrate bending contributions, was compared for varying top electrode sizes ranging from 50 μm to 200 μm. For constant electric field excitation, an enhanced bending-free sample displacement was observed for electrode diameters less than 100 μm, as illustrated in Figure 5-8a. (consistent with the findings by Lepadatu et al.[114] using a scanning

beam vibrometer). However, for electrode diameters greater than 100 μm, the substrate bending contribution, measured away from the electrode as shown in Figure 5-8b, was out of phase with the applied field excitation and increased with the electrode area. Hence for a true $d_{33,f}$ response characterization on a blanket piezoelectric films using this interferometry approach, electrode sizes less than 100 μm should be used. The measured $d_{33,f}$ for the 1 μm thick randomly oriented film poled under the conditions described above on a 50 μm diameter electrode was ~36.5 ± 0.6 pm/V.
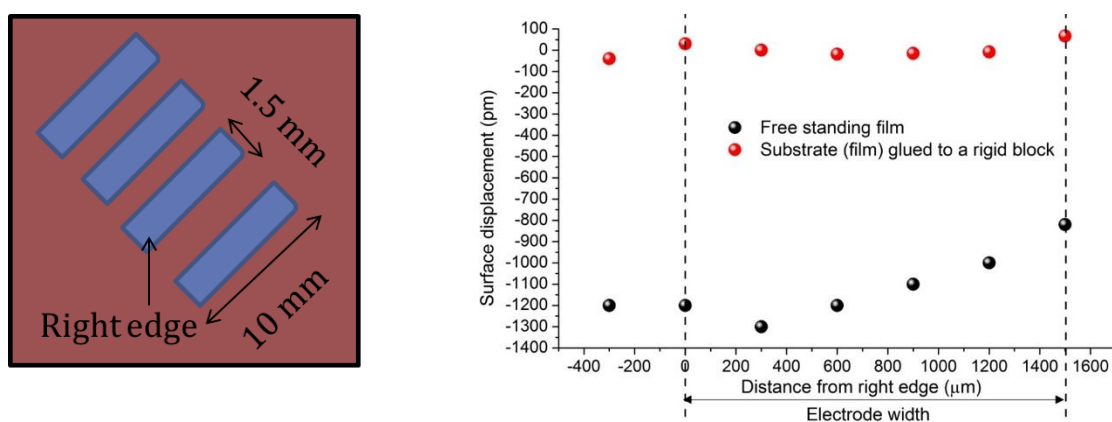
Figure 5-7: Large signal sample displacement for $PbZr_{0.3}Ti_{0.7}O_3$ films as a function of mechanical clamping of the growth substrates, measured along the electrode width using single beam laser interferometer. Large electrode area, in case of free standing (unglued) substrate produce nm displacement (black) for a ac field excitation of 2.5 V amplitude superimposed on a $3V_{dc}$ signal. Note the displacement is negative, indicating the dominance of substrate bending contributions over piezoresponse. For mechanically clamped substrates, this contribution (shown in red) is reduced significantly, however the small negative displacement measured 250 μm away from the right electrode edge still indicated presence of substrate bending
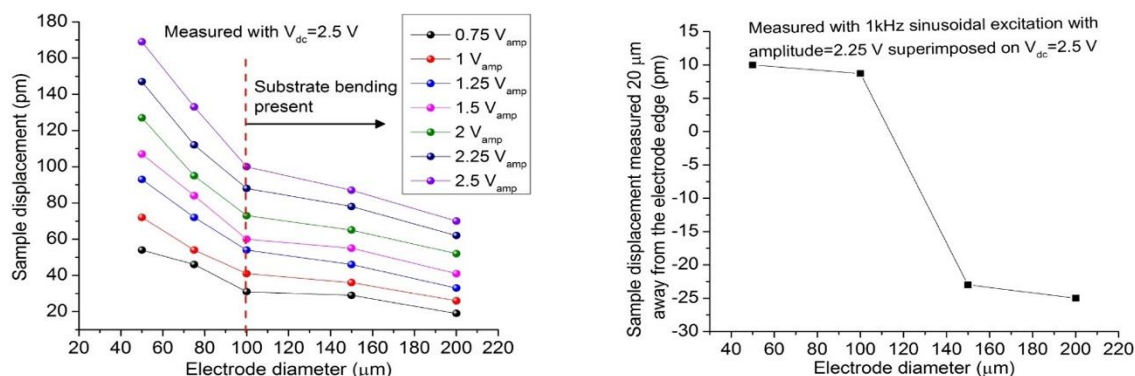
Figure 5-8: (a) Sample displacement measured at the electrode center in $PbZr_{0.52}Ti_{0.48}O_3$ continuous films with electrode diameters varying from 50 μm to 200 μm. (b). Sample displacement measured 20 μm away from the electrode edge. Note the negative displacement measured in case of electrode diameter greater than 100 μm, indicating bending of substrate.

In the case of 500 nm thick patterned $PbZr_{0.52}Ti_{0.48}O_3$ films, the small signal $d_{33,f}$ measured as a function of spatial position across a 5 μm feature (poled at room temperature) for V_{ac}=1.5 V has been plotted in Figure 5-9. The signal was observed over a larger apparent width due to the focused beam size (~ 2 μm). The sample displacement was less than 1 pm about 2.2 μm on either side of the feature edges. The piezoelectric response is highest near the sidewall of the patterned features, due to the relaxation of the mechanical constraints of underlying rigid Si substrate. An enhancement of ~100% was observed along the edges relative to the central fully clamped region of the feature. Figure 5-10a compares the small signal $d_{33,f}$ values for 5 μm and 10 μm arm patterns for both room temperature (red) and 150°C (blue) measured along the edge for the similar excitation voltage. Room temperature poled sample show a 50-60% increase in piezoresponse for smaller feature. The $d_{33,f}$ measured in the central region for both patterns varied between 30-40 pm/V. This corroborates greater declamping as a function of lateral scaling. Hot poling further enhances the $d_{33,f}$ by 80% in 5 μm and 120% in case on 10 μm. Figure 5-10b further corroborates lateral declamping in hot poled samples as a function of feature size with 22% increase for 10 μm, 30% for 8 μm arm and

44% enhancement for 5 μm (center to edge). The single beam interferometer reported here allows this to be measured quantitatively.

It is believed that the limits of the proposed interferometry approach have not been reached. The vertical resolution of the interferometer is currently limited by the ambient vibration noise, not the ultimate resolution of the optics of the system.   In theory, the lateral resolution can be reduced to 400 nm by switching to a larger numerical aperture Mirau objective (100x, NA ~ 0.7) and low wavelength laser (~460 nm) routinely used for interferometry. The bandwidth of the single beam interferometer microscope is currently limited by the high current gain setting on the photomultiplier tube (bandwidth of 20 kHz for the lowest gain setting). It is believed that both vertical resolution and bandwidth can be significantly improved by using a high intensity He-Ne laser, better isolation from room vibration, higher bandwidth optical detector and/or minimizing the optical power loss at each optical surface. This metrology approach, in addition to electrical characterization can be systematically used to provide absolute quantification of electromechanical coefficients as a function of scaling in piezoelectric films.
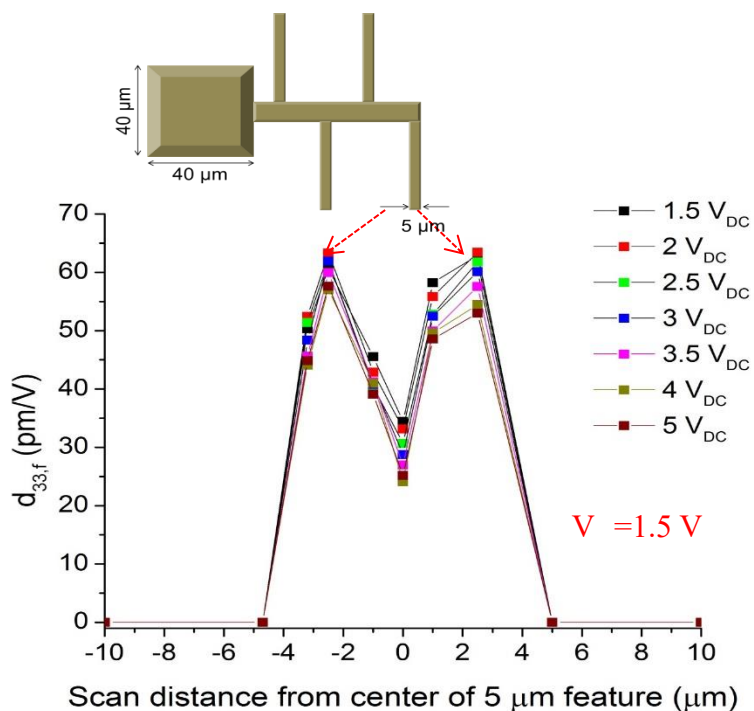
Figure 5-9: Small signal $d_{33,f}$ scan across a 5 μm etched feature showing minimal substrate bending outside the pattern and increased values along the sidewalls.
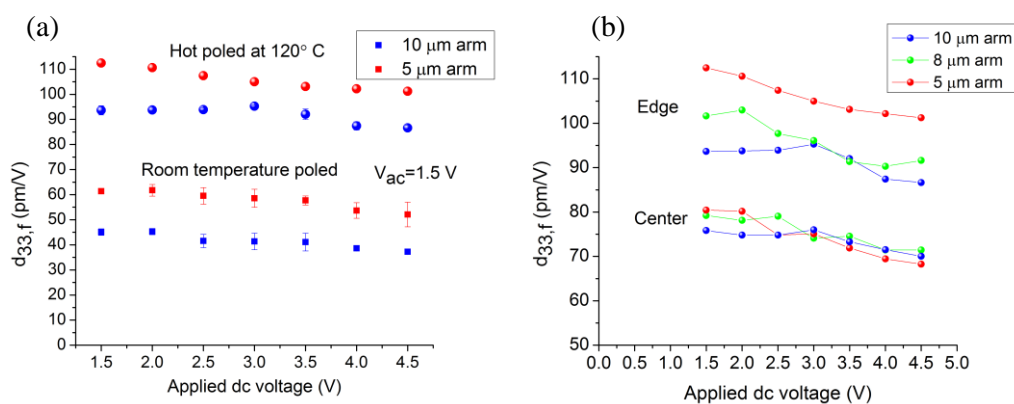
Figure 5-10 (a): Small signal $d_{33,f}$ comparison between room temperature and hot poled 5 μm vs 10 μm etched features (measured on the feature edge) (b) Comparison of sample response on edge vs center for 5,8 and 10 μm feature sizes for hot poled electrodes.

Chapter 6

Conclusion and future work

This chapter will briefly summarize the major findings in this thesis. Based on the experimental observations, guidelines for future works will be recommended.

6.1 Conclusions

6.1.1 Relaxor behavior in engineered Lead Magnesium Niobate (PMN) thin film heterostructures

PMN is well studied relaxor ferroelectric perovskite, with coexistence of polar nano-regions, multivalent B site cation order in chemically ordered regions, and their intimate interactions in a paraelectric matrix. In undoped bulk PMN, the cation order can hardly be changed, though the polar order is responsive to both electric field and temperature. This work reports the first PMN thin film material with long-range cation order. Heterostructure films grown as alternate layers of $Pb(Mg_{2/3}Nb_{1/3})O_3$ and $PbNbO_3$ are compared to PMN films grown from a single target. It was found that the (111) orientation facilitated the phase pure growth of 111 ordered heterostructure films, compared to the (001) orientation. The heterostructures showed significantly larger regions of chemical ordering. Selected area electron diffraction confirmed emergence of superlattice spots (1/2, 1/2, 1/2) with randomly distributed ordered domains as large as 100 nm. These heterostructures exhibited a dielectric constant of 800, loss tangents of approximately 0.03 and 2*remanent polarization of ~11 $\mu C/cm^2$ at room temperature. Polarization-electric field loops, Rayleigh data and optical second harmonic generation measurements are consistent with the development of ferroelectric domains below 140 K. The comparative study with short range ordered films elucidates the impact of long-range cation order in PMN on its electrical properties.

Temperature dependent permittivity measurements demonstrate reduced frequency dispersion compared to short-range-ordered PMN films. It was observed that the relaxor behavior did not "switch "off" in the presence of longe-range-ordering along one axis, although the Rayleigh, polarization and thermal depolarization data are consistent with increased levels of longer-range ferroelectric ordering. This work is an important step towards addressing many scientific questions in relaxor ferroelectricity such as understanding the interaction between chemically ordered regions and the polar domains. It is anticipated that this work will be useful in refining the models for relaxor ferroelectric behavior as a function of chemical ordering. This could have technological significance on further improving usage of PMN based material properties for several applications.

6.1.2 Effect of ordering on the non-linear dielectric properties of PMN

The dynamic nonlinear dielectric responses of (111) oriented $PbMg_{1/3}Nb_{2/3}O_3$ were studied as a function of temperature for thin films with long- and short-range ordering. It was found that long-range ordering decreased the dispersion in the first and third harmonic displacement current relative to short-range ordered films. For both sets of films, a second harmonic component of the dielectric response was also detected. The phase angles of the higher harmonic responses were used to probe the continuum in ferroelectric-relaxor behavior in these films. At high temperatures (e.g. above the freezing temperature), the presence of nanopolar clusters is believed to cause the strong dispersion in the third harmonic response in both long range and short-range films. However, at lower temperatures, changes in the sign of χ_3 suggest long-range ferroelectric ordering, such that the response of mobile interfaces (believed to be domain walls) dominate the response.

6.3 Quantitative characterization of laterally declamping in thin PMN-PT film using a novel Mirau based interferometry with high lateral resolution

A novel Mirau based interferometry microscope with ~ 2 μm spatial resolutions and ~1 pm minimum detectable displacement has been developed to measure piezoelectric response over a frequency range of 2 Hz-2 kHz. Results on piezoelectric PMN-PT single crystal and bulk ceramic PZT conform closely to data measured using standard techniques like Berlincourt and double beam laser interferometry. This microscope has been successfully applied to understand substrate bending as a function of electrode diameter. This approach has been used to illustrate partial declamping in patterned $PbZr_{0.52}Ti_{0.48}O_3$ films for electrode sizes down to 5 μm.

6.2 Future work

6.2.1 Quantification of $d_{33,F}$ in clamped and released PMN-PT thin films using microfabricated test structures with increased stiffness

Extremely high piezoelectric coefficients have been reported in domain engineered piezoelectric crystals with a relaxor ferroelectric end member[62]. {001} oriented $PbMg_{1/3}Nb_{2/3}O_3$-$PbTiO_3$ (PMN-PT) single crystals exhibit piezoelectric coefficients several times than that of ceramic $PbZr_{1-x}Ti_xO_3$, for compositions near 33% PT in PMN-PT solid solution, with electromechanical coupling coefficient k_{33} of 0.9[20]. This piezoelectric enhancement has been attributed to polarization rotation in domain engineered rhombohedral crystals near the morphotropic phase boundary, MPB. Recently, high-quality PMN-PT epitaxial thin films have also been grown on $SrTiO_3$ buffered (001) Si wafers with superior piezoelectric coefficients ($e_{31,f}$ = -27 ± 3 C/m^2)[144]. Finite element model illustrate the enhancement of the dielectric permittivity and piezoelectric constant with reduction of the lateral feature dimension in a {001} oriented 70PMN-30PT film[145]. As experimentally observed in the $PbZr_{0.52}Ti_{0.48}O_3$ films (Chapter 5), the

piezoelectric response for the PMN-PT model is highest near the sidewall of the patterned feature. However, there is a significant increase in response at the center of a feature in PMN-PT film on declamping for width: height aspect ratios less than 2, yielding effective piezoelectric coefficients closer to those observed in bulk samples.

To date, there is no complete characterization of the piezoelectric response in finely patterned PMN-PT films. In preliminary experiments towards this quantification, 1 μm thick pure-phase 70PMN-30PT was grown epitaxially on $SrRuO_3$ electroded $SrTiO_3$ substrates using pulsed laser deposition (growth parameters listed in Table 6-1). The films were then laterally patterned using a BCl_3/Cl_2 etch in a Tegal 6572 reactive ion etching tool (Tegal Corporation, Petaluma, CA) with a Ni hard mask. The RIE plasma was excited using 500W bias power in the MHz regime with chamber pressure maintained at 2 mTorr. The etch rate of PMN-PT was calculated to be 20 Å/sec with a 7:1 selectivity to $SrRuO_3$. The after-etch image of a 2 μm pattern etched in PMN-PT film is shown in Figure 6-1. Electrical characterization as summarized in Figure 6-2 shows minimal change in dielectric properties after etch.

Table 6-1: PMN-PT PLD growth parameters

Parameter	Value
Target to Substrate Distance	4.8 cm
Temperature	590°C
Pressure	60 mTorr
Targeted Laser Energy Density	1.8 J/cm² (180 mJ input)
Laser Frequency	15 Hz
Thickness	**1** μm
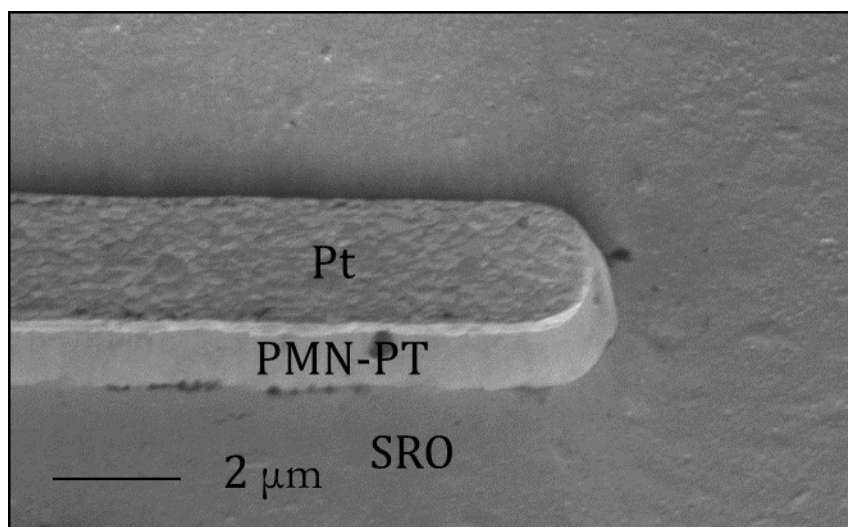
Figure 6-1: 2µm PMN-PT arm after etching with measured sidewall angle of ~80°
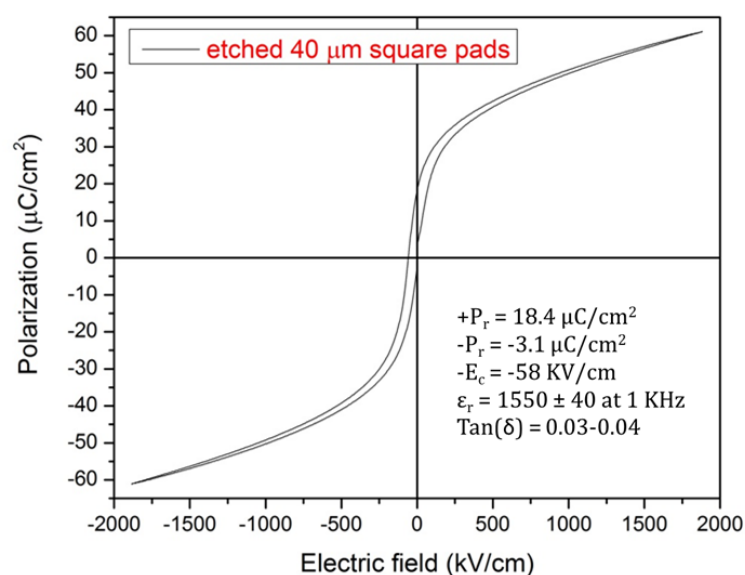
Figure 6-2 Hysteresis loop for etched PMN-PT patterned film.

Large signal d_{33} measurement was performed on varying feature sizes with an ac signal ranging from 0-3V (30 kV/cm) superimposed on a 3V dc signal. The average $d_{33,f}$ on a large clamped electrode was measured to be ~95±3 pm/V, while those on a 2 µm feature size was

measured to be 178 ±2 pm/V. As compared to intrinsic $d_{33,f}$ reported by Keech et al.[145] on thin

polycrystalline PMN-PT film characterized via in-situ nanobeam diffraction, these reported

numbers are small. This is attributed to substrate bending induced by the thicker PMN-PT films.

Further verification of this effect is proposed via use of stiff masking oxide layer on the

piezoelectric thin film structures to reduce contributions from bending in measured $d_{33,f}$ and

scanning in exposed areas as shown in Figure 6-4.. The thickness of the stiff oxide or nitride layer

can be calculated by measuring the substrate bending on PMN-PT film grown on STO substrate,

using the single beam laser interferometer. Next, the required film thickness can be calculated f

using finite element modeling employing Stoney's equation for given film stress.

It will be interesting to measure the $d_{33,f}$ on a released PMN-PT thin film cantilever

structure for the true unclamped value of the material (similar to PZT)[146,147] using the single beam

interferometer. This can be successfully achieved by designing a residual stress-free stack

(PE/electrode/oxide) with proper material design and geometry.
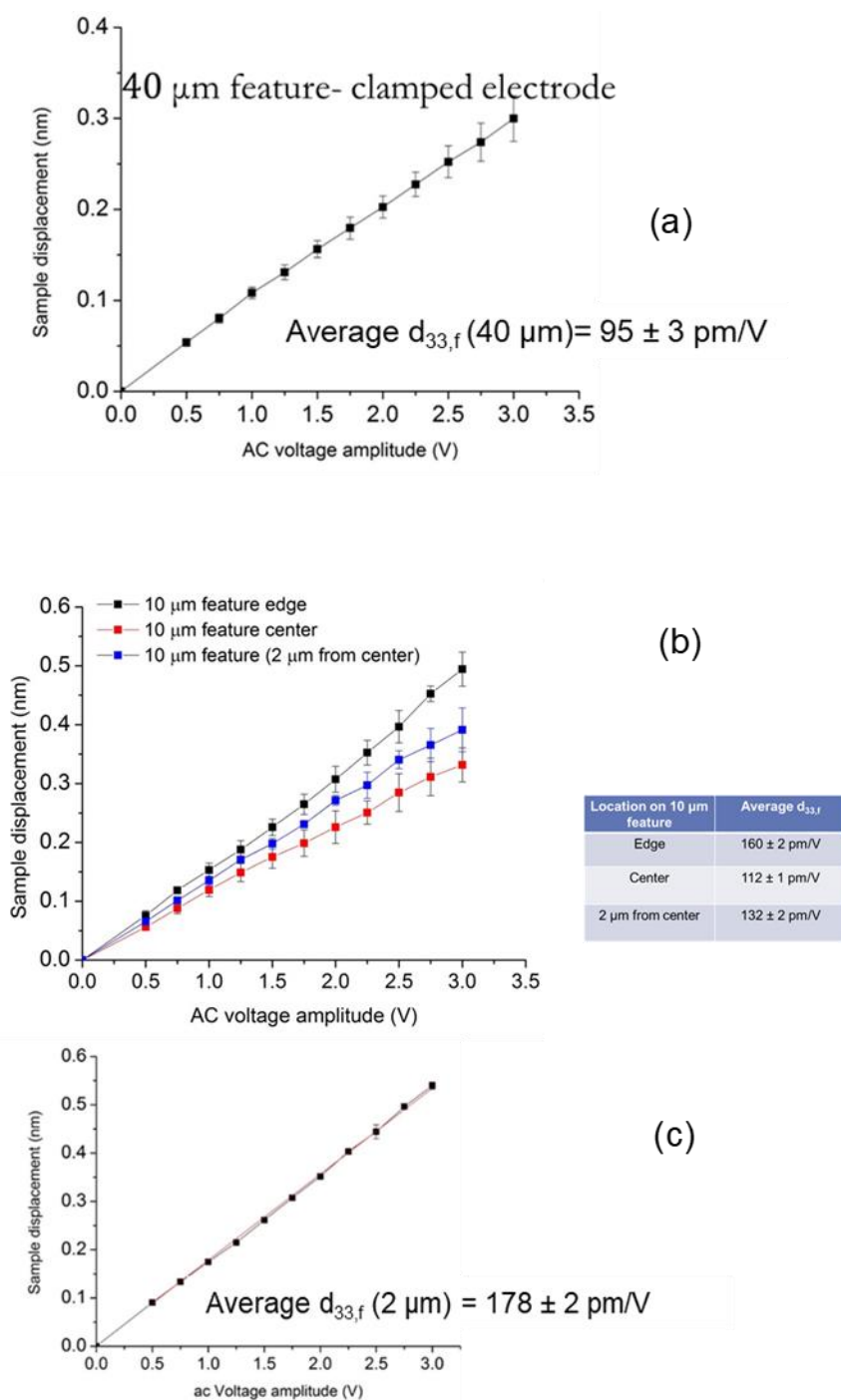
Figure 6-3: $d_{33,f}$ Quantification on patterned 70PMN-30PT film on (a) 40 μm fully clamped electrode pads (b) 10 μm arms (tabulated $d_{33,f}$ for different locations on the arm) (c) 2 μm arms

Scanning laser spot

Stiff oxide mask layer
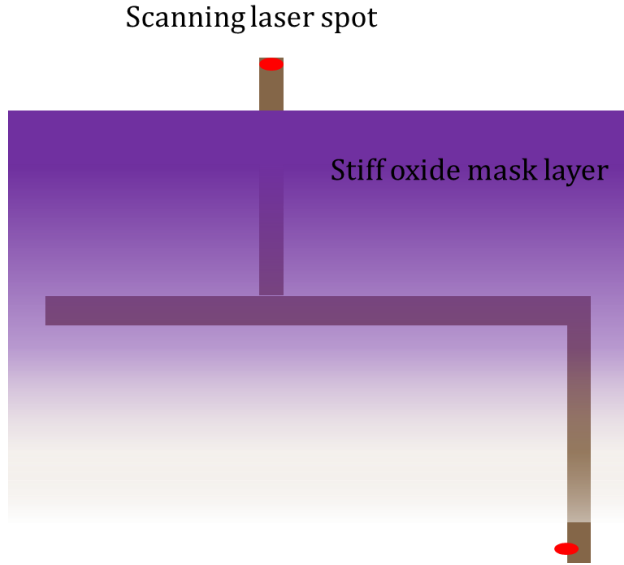
Figure 6-4 Schematic for proposed stiff oxide mask to reduce substrate bending.

6.2.2 Understanding the impact of ordering in relaxor thin films on flexoelectric properties using a spatially resolved d_{33} microscope

The suppression of relaxor characteristics by digitally ordering the superlattices in PMN could have broader implications, given recent findings in the area of flexoelectricity. Flexoelectricity defines the linear coupling between induced polarization or stress by applied strain or electric field gradients. Flexoelectric coefficients are found to be proportional to dielectric susceptibility, with the coupling factor theoretically calculated to vary between 1-10 V[148]. However experimental measurements on bulk relaxor system indicate that the flexoelectric coefficients in relaxor materials, near the transition temperature, are disproportionately large[148–151]. This disparity implies that another type of electro-mechanical coupling operates simultaneously in the material that possibly dominates over the flexoelectric charge.

It has been suggested that an extrinsic contribution to the flexoelectric effect could involve either the response of ferroelastic polar nanoregions to a strain gradient[150,152,153] or processing-induced strain gradients[154] due to chemical inhomogeneity and self-polarization. In bulk relaxor

BST, Garten[153] et al. measured residual ferroelectricity about 30°C above T_{max} using Rayleigh analysis and corroborated the onset of flexoelectric poling with irreversible contributions to the dielectric response within 10°C of T_{max}. Their work established that the application of a strain gradient on samples with PNR near transition temperature can induce flexoelectric poling, with anomalously large measured flexoelectric coefficients. Similarly, in 72PMN-28PT ceramics, Catalan[152] et al. observed hysteresis in the flexoelectric response upon heating and cooling, and increasing coupling factor at T> T* associated with the onset of anelastic softening, suggesting presence of PNR (T* was extrapolated at temperatures marking departure from Curie Weiss law) as shown in Figure 6-5. However, with higher %PT (reduced degree of relaxor), long range polarization appears at T_c, accompanied with lower flexoelectric coupling.
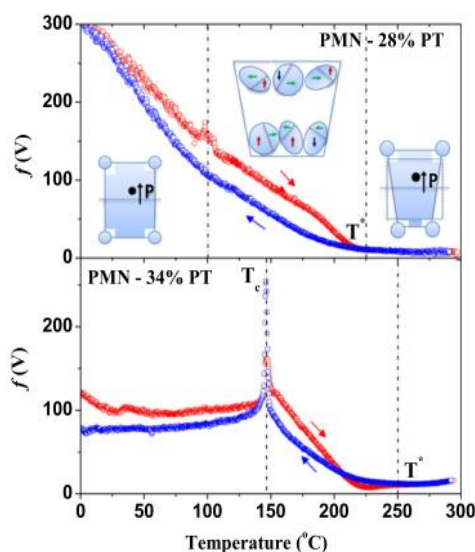
Figure 6.5: Flexoelectric coupling coefficient measured as a function of temperature on 72PMN-28PT and 66PMN-34PT (Figure from reference[152]).

Electric field gradient along z direction
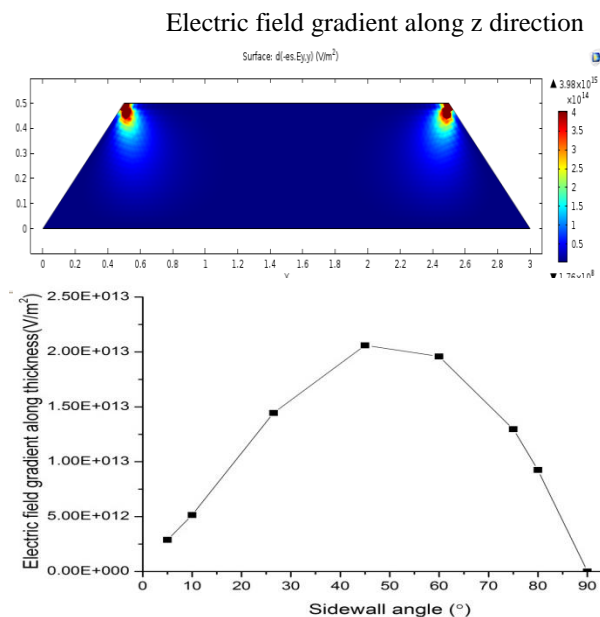
Figure 6.6: Finite element simulation in Comsol results with electric field gradient through thickness as a function of sidewall angle.

Growth of ordered PMN superlattice films may potentially impede the coexistence of polar nano regions by stabilizing a long-range-ordered ferroelectric phase. As a consequence, the

application of a strain or electric field gradient would not provide enhanced contribution through flexoelectric poling, enabling measurement of the intrinsic flexocoupling coefficient. This hypothesis could be experimentally validated by measuring the elastic strain induced in PMN under inhomogeneous electric fields closer to T_{Burns}. The out of plane displacement due to converse flexoelectric in epitaxial PMN films is given by Equation 4[155]:

$$\text{Flexoelectric displacement} = \frac{\mu_{33}*t}{c_{33}}\frac{dE_Z}{dz} \qquad \qquad \text{Equation 4}$$

where μ_{33} is the flexoelectric coefficients, t is the film thickness, c_{33} is the elastic compliance and $\frac{dE_Z}{dz}$ is the electric field gradient through thickness.

Gradients in electric field have been generated in bulk samples by designing a trapezoidal capacitor with sidewall angles for converse flexoelectric measurements[151,156–158] . This can be replicated in thin films by tailoring the dielectric etch chemistry. Preliminary finite element simulations using COMSOL[TM] in 500 nm thick PMN film (using bulk PMN ceramic material constants)[152] as shown in Figure 6-6, demonstrate maximum field gradients for sidewall angle of 45° for an applied voltage of 25V (in agreement with [157]). The magnitude of these gradient can generate sample displacement as large as 400 pm, which would be easily detected by the single beam laser interferometer. To enable measurements closer to T_{Burns}, a temperature-controlled stage would need to be incorporated to existing interferometer setup. Further finite element modeling is required to calculate the electric field gradient, using the measured film permittivity and applied field. Initial calculations for a 100 nm thick PMN films (with permittivity of 800) yield a flexo-displacement of 100 pm for a 1 V field, which can be detected by the interferometer. The measured magnitude of the flexoelectric displacement would provide information on the interplay between PNR alignment with flexoelectric poling under inhomogeneous fields,

indicating if this mechanism contributes to the flexoelectric response measured in these materials.

6.2.3 Ordering in BaMg$_{1/3}$Nb$_{2/3}$O$_3$ to improve Q:

Microwave resonators require materials having very low dielectric losses, thereby enabling increased selectivity and bandwidth. For the Ba based perovskite like BaMg$_{1/3}$Ta$_{2/3}$O$_3$ (BMT), BaMg$_{1/3}$Nb$_{2/3}$O$_3$ (BMN), BaZn$_{1/3}$Ta$_{2/3}$O$_3$ (BZT), BaZn$_{1/3}$Nb$_{2/3}$O$_3$ (BZN) etc., increasing the degree of ordering on the B-sublattice can induce order of magnitude changes in the dielectric quality factor (Q) and significantly reduce the dielectric losses at microwave frequencies[159–162]. In contrast to PMN, disordered BMN have a cubic structure (Pm-3m) but undergoes a structural phase transition on cooling to a trigonal (P-3m1) ordered state[163]. Ordered BMN has a 1:2 stoichiometric ordering of the Mg^{2+} and Nb^{5+} ions along the pseudocubic <111> direction[43]. Typically, ordering is achieved by extended annealing below the sintering temperature (T$_{order-disorder}$ ~ 1350-1400 °C)[164]. It would be of technological interest to understand the effect of increasing ordering in the BMN system on the dielectric loss and Q via the engineered layered growth approach. Initial film growth results on 100 and 111 STO substrates using single BMN target pulsed laser ablation (courtesy: Jieun Kim, UC Berkeley) have been summarized in Figure 6.7. Both the films were phase pure with minimal surface roughness. Further structural and electrical characterization needs to be done on single target and engineered BMN heterostructure films.
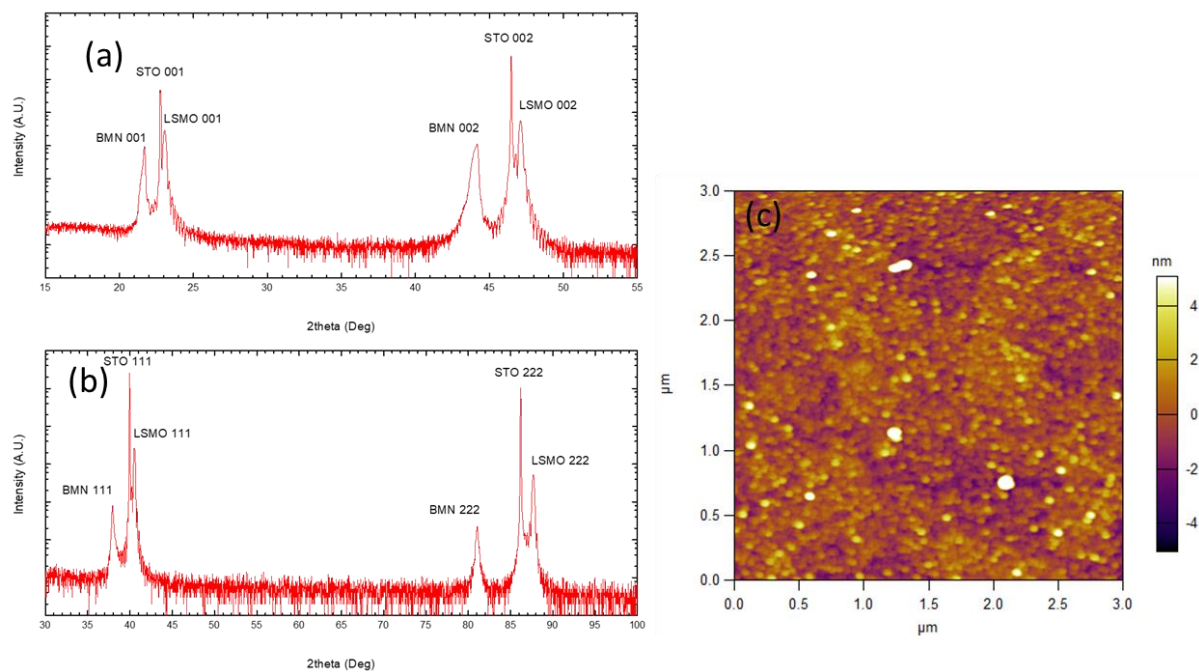
Figure 6.7: Growth of pure phase BMN from single target on (a) 001 STO (b) 111 STO (c) film surface roughness on 111 STO

Appendices

Appendix A: RHEED assisted growth of PbMg$_{2/3}$Nb$_{1/3}$O$_3$-PbNbO$_3$ heterostructure films

Heterostructure growth was attempted on a RHEED assisted PLD tool on SrRuO$_3$ bottom electrodes grown on treated (111) SrTiO3 substrates. The growth parameter for epitaxial SrRuO$_3$ thin film has been tabulated in Table A-1, with the RHEED pattern and corresponding roughness as a function of thickness shown in Figure A-1. Interestingly, the growth transitioned from 3-d to 2-d with increasing thickness.
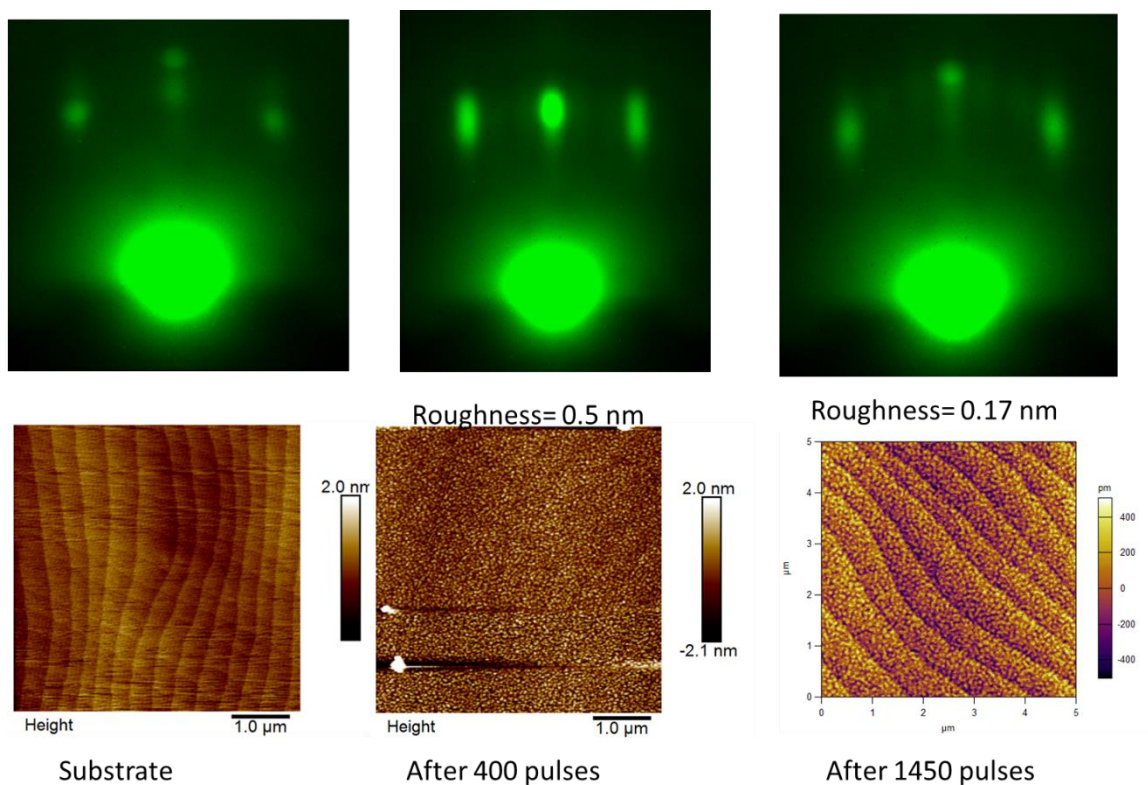
Figure A-1: RHEED patterns (top) along the <-110> for SrRuO$_3$ grown on 111 STO substrates with corresponding roughness data obtained from AFM (contact mode)

Table A-1: Growth parameters for SrRuO3 and PbMg$_{2/3}$Nb$_{1/3}$O$_3$ and PbNbO$_3$ individual layers

Parameter	SrRuO$_3$	PbMg$_{2/3}$Nb$_{1/3}$O$_3$/PbNbO$_3$
Temperature	700°C	630°C
Pressure (O$_2$)	100 mTorr	200 mTorr
Laser density	1.5 J/cm^2	0.9 J/cm^2
Laser frequency	5 Hz	3 Hz

PMN growth calibration involved initial film synthesis using the single Mg rich PMN target on layer by layer grown SrRuO3 using conditions tabulated in Table A-1. Two repeatable stable RHEED oscillations were observed as shown in Figure A-2, after which islanding occurred. Next the unit heterostructure growth was attempted, by calculating the number of pulses corresponding to unit cell of **PbMg$_{2/3}$Nb$_{1/3}$O$_3$** followed by ablation of the **PbNbO$_3$** target. As seen in Figure A-3, growth of the PbNbO$_3$ layer led to instant islanding in the film. Hence a timed based synthesis approach was adopted for film growth.
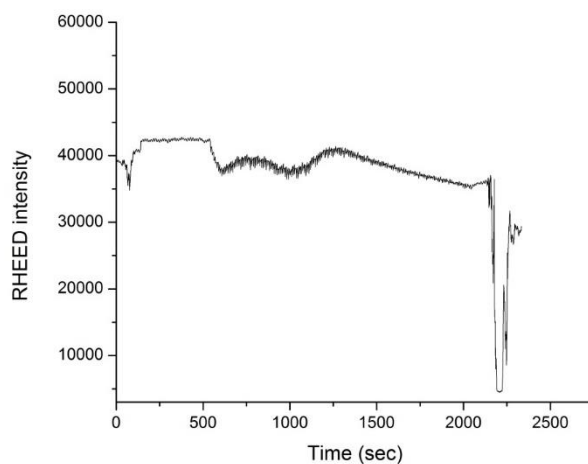
Figure A-2: RHEED oscillations corresponding to Mg rich PMN target

(a)

(b)
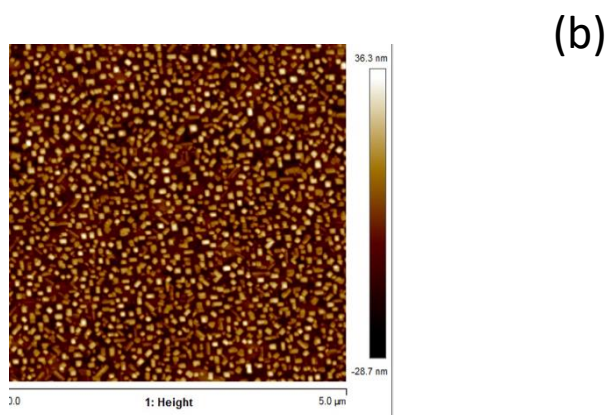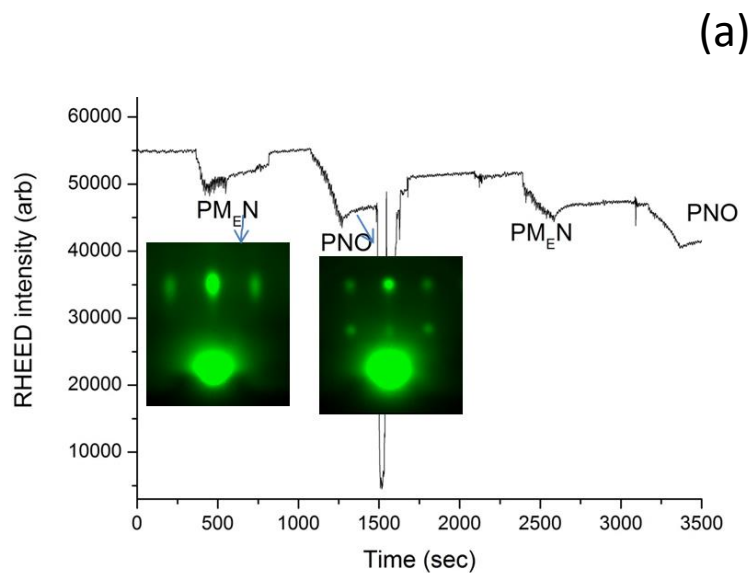
Figure A-3: (a) RHEED oscillations corresponding to pulsating Mg rich PMN target and PNO targets (b) AFM surface roughness data suggesting islanding.

Appendix B: Growth of heterostructure PMN thin films on different substrates

Two-target PMN heterostructure growth was also achieved on $DyScO_3$, $GdScO_3$ and $NdScO_3$ (101) oriented substrates obtained from CrysTec GmbH, Germany, using timed pulsed laser deposition to understand the effect of strain induced by the substrate. $Ba_{0.7}Sr_{0.3}RuO_3$ films (~30 nm thick) were epitaxially grown as the bottom electrode on the treated substrates by pulsed laser deposition, at 1023 K in an oxygen pressure of 200 mTorr, with a laser fluence of 1.3 J/cm^2 at a repetition rate of 3 Hz. Long-range ordered PMN film growth was achieved via subsequent pulsing of the $PbNbO_3$ and $PbMg_{2/3}Nb_{1/3}O_3$ layers from 1% La doped target batched with 20% excess Pb at 873 K in an oxygen pressure of 200 mTorr at a laser fluence of 1 J/cm^2 and a laser repetition rate of 3 Hz. The XRD patterns are shown in Figure B-1 and the scanning electron microscope cross-section images are presented in Figure B-2. As seen from the XRD image, the films grown on DSO (PMN thickness-75 nm) and GSO (PMN thickness-80 nm) substrates were relaxed, while the films grown on the NSO substrate (PMN thickness-60-65 nm) was under tensile strain (0.13 %). As seen from the SEM images, the surface roughness was high on all the non-STO substrates. Further growth optimization is required for smoother film growths.

Temperature dependent dielectric permittivity-loss (as a function of frequency) and dielectric Rayleigh characterization (as a function of ac field) results on the different substrates have been summarized in Figure B-3. Frequency dispersion persisted in all the films, with similar peak in the irreversible Rayleigh coefficient in the measured temperature range. As shown in Table B-1, there was a small shift in T_{max} and small shift in $T_{\alpha, max}$ peak in relaxed PMN heterostructure films on different substrates.
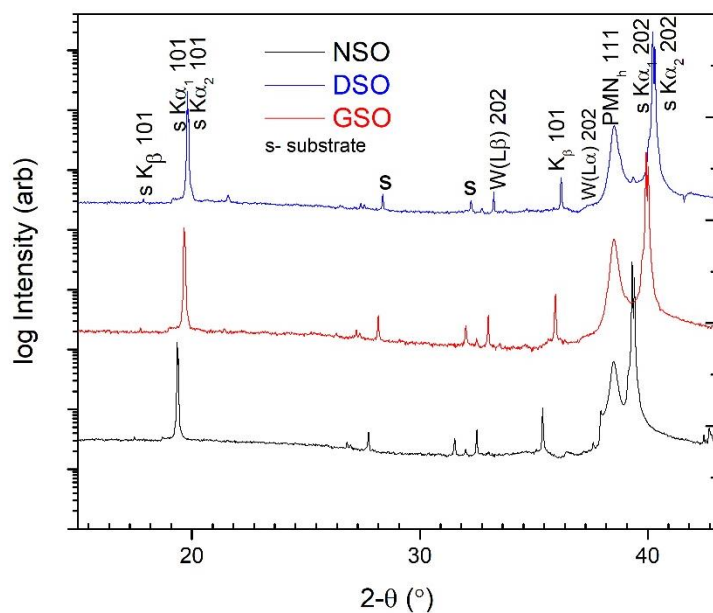
Figure B-1: XRD of the two target PMN heterostructure grown on different substrate
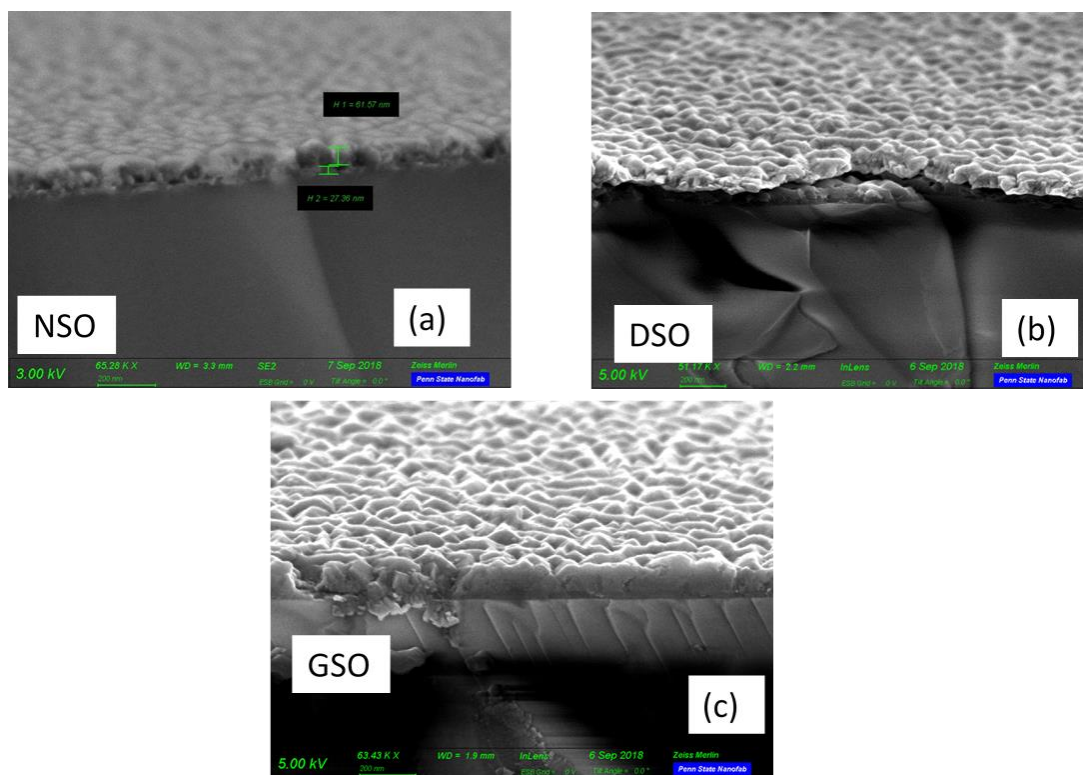
Figure B-2: Cross-section SEM images of the two target PMN heterostructure grown on different substrates
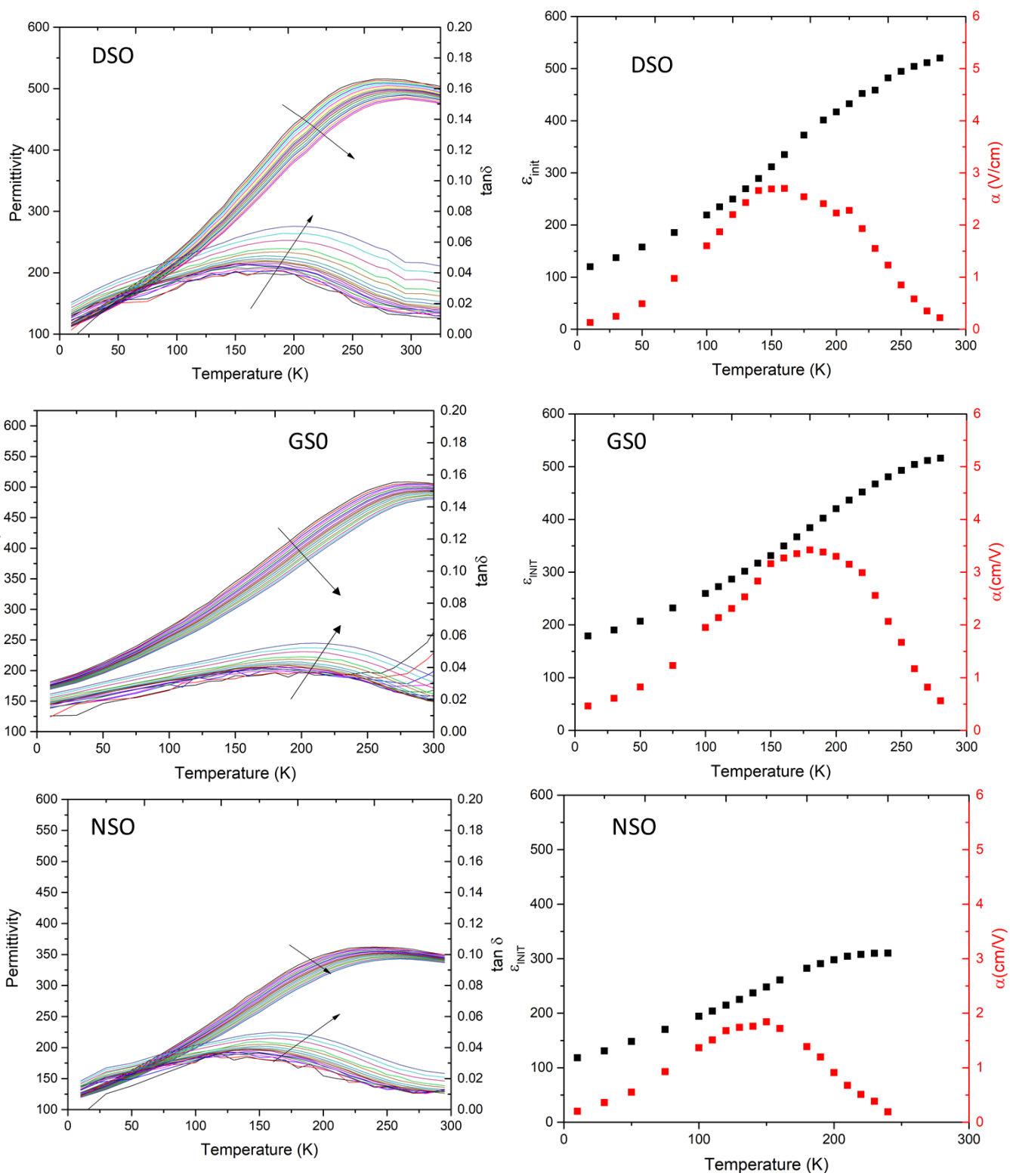
Figure B-3: C-D measurement (left) and Rayleigh measurement (right) for two target PMN films grown on different substrates

	STO (PMN thickness-100 nm)	**DSO** (PMN thickness-75 nm)	**GSO** (PMN thickness-80 nm)	**NSO** (PMN thickness-60-65 nm)
Tmax (at 1 kHz)	250 K	280 K	280 K	240 K
Tα peak	150 K	160 K	170 K	150 K

Table B-1: Summary of T_{max} and T_{α} for two target PMN heterostructure grown on different substrate

References

[1] S. Trolier-McKinstry and P. Muralt, "Thin film piezoelectrics for MEMS," J. Electroceramics, **12**, 7–17, (2004).

[2] F. Li, S. Zhang, D. Damjanovic, L.Q. Chen, and T. Shrout, "Local structural heterogenity and electromechanical responses of ferroelectrics: learning from relaxor ferroelectrics," Adv. Funct. Mater., **1801504**, 1–21, (2018).

[3] L.E. Cross, "Relaxor ferroelectrics: An overview," Ferroelectrics, **151**, [1], 305–320, (1994).

[4] A. Bokov and Z.-G. Ye, "Recent progress in relaxor ferroelectrics with perovskite structure," J. Mater. Sci., **41**, [1], 31–52, (2006).

[5] Z.G. Ye, "Relaxor ferroelectric complex perovskites: structure, properties and phase transitions," Key Eng. Mater., **155**–**156**, 81–122, (1998).

[6] M. Lejeune and J. Boilot, "PbMg$_{1/3}$Nb$_{2/3}$O$_3$ (PMN) multilayer capacitors," J. Phys., **47**, [C1], 895–899, (1986).

[7] P. Davies and M. Akbas, "Chemical order in PMN-related relaxors: structure, stability, modification, and impact on properties," J. Phys. Chem. Solids, **61**, [2], 159–166, (2000).

[8] P.M. Solomon, B.A. Bryce, M.A. Kuroda, R. Keech, S. Shetty, T.M. Shaw, M. Copel, L.-W. Hung, A.G. Schrott, C. Armstrong, M.S. Gordon, K.B. Reuter, T.N. Theis, W. Haensch, S.M. Rossnagel, H. Miyazoe, B.G. Elmegreen, X.-H. Liu, S. Trolier-McKinstry, G.J. Martyna, and D.M. Newns, "Pathway to the piezoelectronic transduction logic device," Nano Lett., **15**, [4], (2015).

[9] T.N. Theis and P.M. Solomon, "It's time to reinvent the transistor!," Science, **327**, [5973], 1600–1, (2010).

[10] D.M. Newns, B.G. Elmegreen, X.-H. Liu, and G.J. Martyna, "The piezoelectronic

transistor: A nanoactuator-based post-CMOS digital switch with high speed and low power," MRS Bull., **37**, [11], 1071–1076, (2012).

[11] R.R. Keech, Dimensional Scaling of Perovskite Ferroelectric Thin Films, Pennsylvania State University, 2016.

[12] S. Shetty, A. Damodaran, K. Wang, Y. Yakun, V. Gopalan, L. Martin, S. Trolier-McKinstry, and 1Department, "Relaxor Behavior in Ordered Lead Magnesium Niobate (PbMg1/3Nb2/3O3) Thin Films," Adv. Funct. Mater., **04**, 258–268, (2018).

[13] S. Shetty, J.I. Yang, J. Stitt, and S. Trolier-Mckinstry, "Quantitative and high spatial resolution d33 measurement of piezoelectric bulk and thin films," J. Appl. Phys., **118**, [17], (2015).

[14] G.A. Smolensky, "Physical phenomena in ferroelectrics with diffuse phase transition," J. Phys. Soc. Japan, **28**, 26–38, (1970).

[15] L. Cross, "Relaxor ferroelectrics," Ferroelectrics, **76**, [1], 241–267, (1987).

[16] A. Burggraaf and C. Stenger, "On diffuse phase transitions," Ferroelectrics, **20**, 185–187, (1978).

[17] V. Westphal, W. Kleemann, and M.D. Glinchuk, "Diffuse phase transitions and random field induced domain states of relaxor ferroelectric $PbMg_{1/3}Nb_{2/3}O_3$," Phys. Rev. Lett., **68**, [6], 847–850, (1992).

[18] N. Setter and L.E. Cross, "The contribution of structural disorder to diffuse phase transitions in ferroelectrics," J. Mater. Sci., **15**, [10], 2478–2482, (1980).

[19] G.A. Samara, "The relaxational properties of compositionally disordered ABO_3 perovskites," J. Phys. Condens. Matter, **15**, [9], 367–411, (2003).

[20] S.-E. Park and T.R. Shrout, "Ultrahigh strain and piezoelectric behavior in relaxor based ferroelectric single crystals," J. Appl. Phys., **82**, [4], 1804, (1997).

[21] F. Li, S. Zhang, T. Yang, Z. Xu, N. Zhang, G. Liu, J. Wang, J. Wang, Z. Cheng, Z.G.

Ye, J. Luo, T.R. Shrout, and L.Q. Chen, "The origin of ultrahigh piezoelectricity in relaxor-ferroelectric solid solution crystals," Nat. Commun., **7**, 1–9, (2016).

[22] F. Li, S. Zhang, Z. Xu, and L.Q. Chen, "The contributions of polar nanoregions to the dielectric and piezoelectric responses in domain-engineered relaxor-$PbTiO_3$ Crystals," Adv. Funct. Mater., **1700310**, 1–9, (2017).

[23] N. Setter and L.E. Cross, "Role of B-Site cation disorder in diffuse phase transition behavior of perovskite ferroelectrics.," J. Appl. Phys., **51**, [8], 4356–4360, (1980).

[24] P. Bonneau, P. Garnier, G. Calvarin, E. Husson, J.R. Gavarri, A.W. Hewat, and A. Morell, "X-ray and neutron diffraction studies of the diffuse phase transition in ceramics," J. Solid State Chem., **91**, [2], 350–361, (1991).

[25] P. Bonneau, P. Garnier, E. Husson, and A. Morell, "Structural study of PMN ceramics by X-ray diffraction between 297 and 1023 K," Mater. Res. Bull., **24**, [2], 201–206, (1989).

[26] N. De Mathan, E. Husson, G. Calvarin, and A. Morell, "Structural study of a poled PbMg1/3Nb2/3O3 ceramic at low temperature," Mat. Res. Bull., **26**, [11], 1167–1172, (1991).

[27] S. Hong, J. Woo, H. Shin, J.U. Jeon, Y.E. Pak, E.L. Colla, N. Setter, E. Kim, and K. No, "Principle of ferroelectric domain imaging using atomic force microscope," J. Appl. Phys., **89**, [2], 1377–1386, (2001).

[28] X. Zhao, W. Qu, X. Tan, A. Bokov, and Z.-G. Ye, "Electric field-induced phase transitions in (111)-, (110)-, and (100)-oriented $Pb(Mg_{1/3}Nb_{2/3})O_3$ single crystals," Phys. Rev. B, **75**, [10], 104106, (2007).

[29] E. V. Colla, E.Y. Koroleva, N.M. Okuneva, and S.B. Vakhrushev, "Long-time relaxation of the dielectric response in lead magnoniobate," Phys. Rev. Lett., **74**, [9], 1681–1684, (1995).

[30] D. Viehland, S.J. Jang, L.E. Cross, and M. Wuttig, "Freezing of the polarization fluctuations in lead magnesium niobate relaxors," J. Appl. Phys., **68**, [6], 2916–2921, (1990).

[31] A. Levstik, Z. Kutnjak, C. Filipič, and R. Pirc, "Glassy freezing in relaxor ferroelectric lead magnesium niobate," Phys. Rev. B, **57**, [18], 11204–11211, (1998).

[32] A. Glazounov and A.K. Tagantsev, "A "breathing" model for the polarization response of relaxor ferroelectrics," Ferroelectrics, **221**, [1], 57–66, (1999).

[33] A.E. Glazounov and A.K. Tagantsev, "Crossover in a non-analytical behaviour of dielectric non-linearity in PbMg1/3Nb2/3O3 relaxor ferroelectric," J. Phys. Condens. Matter, **10**, [39], 8863–8880, (1998).

[34] W. Kleemann, "The relaxor enigma — charge disorder and random fields in ferroelectrics," J. Mater. Sci., **41**, [1], 129–136, (2006).

[35] W. Kleemann, "Relaxor ferroelectrics: Cluster glass ground state via random fields and random bonds," Phys. Status Solidi Basic Res., **251**, [10], 1993–2002, (2014).

[36] C. Randall and A. Bhalla, "Nanostructural-property relations in complex lead perovskites," Jpn. J. Appl. Phys., **29**, [2], 327–333, (1990).

[37] C. Randall, D. Barber, R. Whatmore, and P. Groves, "A TEM study of ordering in the perovskite, Pb(Sc1/2Ta1/2)O3," J. Mater. Sci., **21**, [12], 4456–4462, (1986).

[38] M.A. Akbas and P.K. Davies, "Domain growth in Pb($Mg_{1/3}Ta_{2/3}$)O3 perovskite relaxor ferroelectric oxides," J. Am. Ceram. Soc., **80**, [11], 2933–2936, (1997).

[39] M.A. Akbas and P.K. Davies, "Thermally induced coarsening of the chemically ordered domains in PbMg1/3Nb2/3O3 (PMN)-based relaxors," J. Am. Ceram. Soc., **83**, [1], 119–123, (2000).

[40] P.K. Davies and M. Akbas, "Growth of the chemically ordered domains in PMN-type relaxor ferroelectrics," Ferroelectrics, **221**, [1], 27–36, (1999).

[41] P.K. Davies, L. Farber, M. Valant, and M.A. Akbas, "Cation ordering and dielectric properties of PMN-PSN relaxors," AIP Conf. Proc., **535**, 38–46, (2000).

[42] P.K. Davies and M. Akbas, "Controlling the chemical order in PMN-type relaxors,"

MRS Symp. Proc., **541**, 425–436, (1999).

[43] P.K. Davies, "Cation ordering in complex oxides," J. Solid State Chem., **4**, [1999], 467–471, (2000).

[44] F. Chu, N. Setter, and a. K. Tagantsev, "The spontaneous relaxor-ferroelectric transition of Pb(Sc 0.5Ta0.5)O3," J. Appl. Phys., **74**, [8], 5129–5134, (1993).

[45] D. Fu, H. Taniguchi, M. Itoh, S.Y. Koshihara, N. Yamamoto, and S. Mori, "Relaxor Pb(Mg1/3Nb2/3)O3: A ferroelectric with multiple inhomogeneities," Phys. Rev. Lett., **103**, [20], 2–5, (2009).

[46] Y. Yan, S.J. Pennycook, Z. Xu, and D. Viehland, "Determination of the ordered structures of $Pb(Mg_{1/3}Nb_{2/3}O_3$ and $BaMg_{1/3}Nb_{2/3}O_3$ by atomic-resolution Z-contrast imaging," Appl. Phys. Lett., **72**, [24], 3145, (1998).

[47] H.Z. Jin, J. Zhu, S. Miao, X.W. Zhang, and Z.Y. Cheng, "Ordered domains and polar clusters in lead magnesium niobate $Pb(Mg_{1/3}Nb_{2/3})O_3$," J. Appl. Phys., **89**, [9], 5048–5052, (2001).

[48] R.A. Cowley, S.N. Gvasaliya, S.G. Lushnikov, B. Roessli, and G.M. Rotaru, "Relaxing with relaxors: a review of relaxor ferroelectrics," Adv. Phys., **60**, [2], 229–327, (2011).

[49] F. Chu, I.M. Reaney, and N. Setter, "Role of defects in the ferroelectric relaxor lead scandium tantalate," J. Am. Ceram. Soc., **78**, [7], 1947–1952, (1995).

[50] I.W. Chen, P. Li, and Y. Wang, "Structural origin of relaxor perovskites," J. Phys. Chem. Solids, **57**, [10], 1525–1536, (1996).

[51] D. Viehland, S.J. Jang, L.E. Cross, and M. Wuttig, "Deviation from Curie-Weiss behaviour in relaxor ferroelectrics," Phys. Rev. B, **46**, [13], 8003, (1992).

[52] B.P. Burton, E. Cockayne, S. Tinte, and U. V Waghmare, "First-principles based simulations of relaxor ferroelectrics," Phase Transitions, **79**, [1], 91–121, (2006).

[53] S. Wakimoto, C. Stock, Z.-G. Ye, W. Chen, P.M. Gehring, and G. Shirane, "Mode-

coupling and polar nanoregions in the relaxor ferroelectric Pb(Mg$_{1/3}$Nb$_{2/3}$)O$_3$," Phys. Rev. B, **66**, 224102, (2002).

[54] A.K. Tagantsev and A.E. Glazounov, "Mechanism of polarization response in the ergodic phase of a relaxor ferroelectric," Phys. Rev. B, **57**, [1], 18–21, (1998).

[55] A. Glazounov and A.K. Tagantsev, "Phenomenological model of dynamic nonlinear response of relaxor ferroelectrics," Phys. Rev. Lett., **85**, [10], 2192–5, (2000).

[56] X. Zhang, C. Mellinger, E. V. Colla, M.B. Weissman, and D.D. Viehland, "Barkhausen noise probe of the ferroelectric transition in the relaxor PbMg$_{1/3}$Nb$_{2/3}$O$_3$-12%PbTiO$_3$," Phys. Rev. B, **95**, [14], 144203, (2017).

[57] R. Pirc and R. Blinc, "Spherical random-bond-random-field model of relaxor ferroelectrics," Phys. Rev. B, **60**, [19], 13470–13478, (1999).

[58] R. Pirc, R. Blinc, and V. Bobnar, "Dynamics of relaxor ferroelectrics," Phys. Rev. B - Condens. Matter Mater. Phys., **63**, [5], 1–9, (2001).

[59] W. Qu, X. Zhao, and X. Tan, "Evolution of nanodomains during the electric-field-induced relaxor to normal ferroelectric phase transition in a Sc-doped Pb (Mg13 Nb23) O3 ceramic," J. Appl. Phys., **102**, [8], 0–8, (2007).

[60] F. Li, D. Lin, Z. Chen, Z. Cheng, J. Wang, C.C. Li, Z. Xu, Q. Huang, X. Liao, L.Q. Chen, T.R. Shrout, and S. Zhang, "Ultrahigh piezoelectricity in ferroelectric ceramics by design," Nat. Mater., **17**, 349–354, (2018).

[61] B. Dkhil, J.M. Kiat, G. Calvarin, G. Baldinozzi, S.B. Vakhrushev, and E. Suard, "Local and long range polar order in the relaxor-ferroelectric compounds PbMg$_{1/3}$Nb$_{2/3}$O$_3$ and PbMg$_{0.3}$Nb$_{0.6}$Ti$_{0.1}$O$_3$," Phys. Rev. B - Condens. Matter Mater. Phys., **65**, [2], 1–8, (2002).

[62] S.-E. Park and T. Shrout, "Characteristics of relaxor-based piezoelectric single crystals for ultrasonic transducers," IEEE Trans. Ultrason. Ferroelectr. Freq. Control, **44**, [5], 1140–1147, (1997).

[63] A. Hilton, C. Randall, D. Barber, and T. Shrout, "TEM studies of Pb(Mg$_{1/3}$ Nb$_{2/3}$)O 3 - PbTiO$_3$ ferroelectric relaxors," Ferroelectrics, **93**, [1], 379–386, (1989).

[64] D. V. Taylor and D. Damjanovic, "Domain wall pinning contribution to the nonlinear dielectric permittivity in Pb(Zr, Ti)O[sub 3] thin films," Appl. Phys. Lett., **73**, [14], 2045, (1998).

[65] D. V Taylor and D. Damjanovic, "Evidence of domain wall contribution to the dielectric permittivity in PZT thin films at sub-switching fields," **82**, [4], 1973–1975, (1997).

[66] N. Bassiri-Gharb, I. Fujii, E. Hong, S. Trolier-McKinstry, D. V. Taylor, and D. Damjanovic, "Domain wall contributions to the properties of piezoelectric thin films," J. Electroceramics, **19**, [1], 49–67, (2007).

[67] S. Trolier-McKinstry, N. Bassiri Gharb, and D. Damjanovic, "Piezoelectric nonlinearity due to motion of 180° domain walls in ferroelectric materials at subcoercive fields: A dynamic poling model," Appl. Phys. Lett., **88**, [20], 202901, (2006).

[68] V. Bobnar, Z. Kutnjak, R. Pirc, R. Blinc, and A. Levstik, "Crossover from glassy to inhomogeneous-ferroelectric nonlinear dielectric response in relaxor ferroelectrics," Phys. Rev. Lett., **84**, [25], 5892–5895, (2000).

[69] W. Kleemann, S. Miga, J. Dec, and J. Zhai, "Crossover from ferroelectric to relaxor and cluster glass in BaTi 1-xZrxO3 (x = 0.25-0.35) studied by non-linear permittivity," Appl. Phys. Lett., **102**, [23], 0–4, (2013).

[70] J. Dec, S. Miga, W. Kleemann, and B. Dkhil, "Nonlinear dielectric properties of PMN relaxor crystals within Landau-Ginzburg-Devonshire approximation," Ferroelectrics, **363**, [1], 141–149, (2008).

[71] J. Dec, S. Miga, and W. Kleemann, "Ferroelectric Phase Transitions Viewed Via Nonlinear Dielectric Response," Ferroelectrics, **417**, [1], 82–92, (2017).

[72] D. Damjanovic, "Ferroelectric , dielectric and piezoelectric properties of ferroelectric thin films and ceramics," Rep. Prog. Phys., **61**, 1267–1324, (1998).

[73] D. Damjanovic and M. Demartin, "Contribution of the irreversible displacement of domain walls to the piezoelectric effect in barium titanate and lead zirconate titanate ceramics," J. Phys. Condens. Matter, **9**, 4943–53, (1997).

[74] D. Damjanovic, *Hysteresis in Piezoelectric and Ferroelectric Materials* (2006).

[75] D.M. Marincel, "The influence of crystal defects on domain wall motion in thin film PZT," Ph.D Diss., (2014).

[76] D. Damjanovic and M. Demartin, "The Rayleigh law in piezoelectric ceramics," J. Phys. D. Appl. Phys., **29**, [7], 2057–2060, (1996).

[77] D. V. Taylor and D. Damjanovic, "Domain wall pinning contribution to the nonlinear dielectric permittivity in $Pb(Zr, Ti)O_3$ thin films," Appl. Phys. Lett., **73**, [14], 2045, (1998).

[78] M. Saad, P. Baxter, J. Mcaneney, A. Lookman, L. Sinnamon, P. Evans, A. Schilling, T. Adams, X. Zhu, R. Pollard, R. Bowman, J. Gregg, D. Jung, F. Morrison, and J. Scott, "Investigating the effects of reduced size on the properties of ferroelectrics," IEEE Trans. Ultrason. Ferroelectr. Freq. Control, **53**, [12], 2208–2225, (2006).

[79] T.M. Shaw, S. Trolier-McKinstry, and P.C. McIntyre, "The properties of ferroelectric films at small dimension," Annu. Rev. Mater. Sci., **30**, 263–298, (2000).

[80] E.L. Colla, S. Hong, D. V. Taylor, A.K. Tagantsev, N. Setter, and K. No, "Direct observation of region by region suppression of the switchable polarization (fatigue) in $Pb(Zr,Ti)O_3$ thin film capacitors with Pt electrodes," Appl. Phys. Lett., **72**, [21], 2763, (1998).

[81] F. Griggio and S. Trolier-McKinstry, "Grain size dependence of properties in lead nickel niobate-lead zirconate titanate films," J. Appl. Phys., **107**, [2], 024105, (2010).

[82] K.-T. Kim, M.-G. Kang, and C.-I. Kim, "Study on the etching damage characteristics of PZT thin films after etching in Cl-based plasma," Microelectron. Eng., **71**, [3–4], 294–300, (2004).

[83] G.E. Menk, S.B. Desu, W. Pan, and D.P. Vijay, "Dry etching issues in the integration

of ferroelectric thin film capacitors," MRS Symp. Proc., **433**, 189–200, (1996).

[84] W. Pan, C.L. Thio, and S.B. Desu, "Reactive ion etching damage to the electrical properties of ferroelectric thin films," J. Mater. Res., **13**, [02], 362–367, (2011).

[85] U. Egger, K. Tomioka, G. Stojakovic, Y. Taniguchi, R. Bruchhaus, H. Zhuang, H. Kanaya, G. Beitel, and S. Sugimoto, "High temperature plasma etching of PZT capacitor stacks for high density FERAMs," Mat. Res. Soc. Symp. Proc., **748**, 1–6, (2003).

[86] P. Werbaneth, J. Almerico, L. Jerde, S. Marks, and B. Wachtmann, "Pt/PZT/Pt and Pt/barrier stack etches for MEMS devices in a dual frequency high density plasma reactor," 13th Annu. IEEE/SEMI Adv. Semicond. Manuf. Conf., 177–183, (2002).

[87] V. Nagarajan, S.P. Alpay, C.S. Ganpule, B.K. Nagaraj, S. Aggarwal, E.D. Williams, A.L. Roytburd, and R. Ramesh, "Role of substrate on the dielectric and piezoelectric behavior of epitaxial lead magnesium niobate-lead titanate relaxor thin films," Appl. Phys. Lett., **77**, [3], 438, (2000).

[88] M.D. Nguyen, M. Dekkers, E. Houwman, R. Steenwelle, X. Wan, A. Roelofs, T. Schmitz-Kempen, and G. Rijnders, "Misfit strain dependence of ferroelectric and piezoelectric properties of clamped (001) epitaxial $Pb(Zr_{0.52},Ti_{0.48})O_3$ thin films," Appl. Phys. Lett., **99**, [25], 252904, (2011).

[89] V. Nagarajan, A. Roytburd, A. Stanishevsky, S. Prasertchoung, T. Zhao, L. Chen, J. Melngailis, O. Auciello, and R. Ramesh, "Dynamics of ferroelastic domains in ferroelectric thin films.," Nat. Mater., **2**, [1], 43–7, (2003).

[90] V. Nagarajan, "Scaling of the piezoelectric response in ferroelectric nanostructures: An effective clamping stress model," Appl. Phys. Lett., **87**, [24], 242905, (2005).

[91] S. Bühlmann, B. Dwir, J. Baborowski, and P. Muralt, "Size effect in mesoscopic epitaxial ferroelectric structures: Increase of piezoelectric response with decreasing feature size," Appl. Phys. Lett., **80**, [17], 3195, (2002).

[92] R. Keech, S. Shetty, M. Kuroda, X. Hu Liu, G.J. Martyna, D.M. Newns, and S. Trolier-McKinstry, "Lateral scaling of Pb(Mg1/3Nb2/3)O3-PbTiO3 thin films for piezoelectric logic applications," J. Appl. Phys., **115**, [23], 234106, (2014).

[93] A. Bernal, A. Tselev, S. Kalinin, and N. Bassiri-Gharb, "Effects of lateral and substrate constraint on the piezoresponse of ferroelectric nanostructures," Appl. Phys. Lett., **101**, [11], 112901, (2012).

[94] F. Griggio, S. Jesse, A. Kumar, O. Ovchinnikov, H. Kim, T.N. Jackson, D. Damjanovic, S. V. Kalinin, and S. Trolier-McKinstry, "Substrate Clamping Effects on Irreversible Domain Wall Dynamics in Lead Zirconate Titanate Thin Films," Phys. Rev. Lett., **108**, [15], 157604, (2012).

[95] M. Wallace, R.L. Johnson-Wilke, G. Esteves, C.M. Fancher, R.H.T. Wilke, J.L. Jones, and S. Trolier-McKinstry, "In situ measurement of increased ferroelectric/ferroelastic domain wall motion in declamped tetragonal lead zirconate titanate thin films," J. Appl. Phys., **117**, 054103, (2015).

[96] D. Fu, H. Taniguchi, M. Itoh, and S. Mori, *Pb(Mg$_{1/3}$Nb$_{2/3}$)O$_3$ (PMN) Relaxor: Dipole Glass or Nano-Domain Ferroelectric?*, InTech, (2012).

[97] M. Yoshida, S. Mori, N. Yamamoto, Y. Uesu, and J.M. Kiat, "Transmission electron microscope observation of relaxor ferroelectric," J. Korean Phys. Soc., **32**, 993–995, (1998).

[98] P. Hirsch, A. Howie, R. Nicholson, D. Pashley, and M. Whelan, *Electron Microscopy of Thin Crystals* (1965).

[99] E. Garboczi, K. Snyder, J. Douglas, and M. Thorpe, "Geometrical percolation threshold of overlapping ellipsoids," Phys. Rev. E, **52**, [1], 819–828, (1995).

[100] I.-K. Jeong, T.W. Darling, J.K. Lee, T. Proffen, R.H. Heffner, J.S. Park, K.S. Hong, W. Dmowski, and T. Egami, "Direct observation of the formation of polar nanoregions in Pb(Mg$_{1/3}$ Nb $_{2/3}$)O$_3$ Using neutron pair distribution function analysis," Phys. Rev. Lett., **94**, [14],

147602, (2005).

[101] K. Lefki and G.J.M. Dormans, "Measurement of piezoelectric coefficients of ferroelectric thin films," J. Appl. Phys., **76**, [3], 1764, (1994).

[102] M.J. Cabral, S. Zhang, E.C. Dickey, and J.M. LeBeau, "Gradient chemical order in the relaxor Pb(Mg$_{1/3}$ Nb$_{2/3}$)O$_3$," Appl. Phys. Lett., **112**, [8], 082901, (2018).

[103] A.K. Tagantsev and A.E. Glazounov, "Mechanism of polariztion response and dielectric non linearity of PMN relaxor ferroelectric," Phase Transitions, **65**, [1–4], 117–139, (1998).

[104] X. Zhao, "Development of long range cation order and its impact on dielectric properties in Pb(Mg$_{1/3}$Nb$_{2/3}$)O$_3$ based relaxor ferroelectrics," Ph.D Diss., Iowa State University (2008).

[105] E. V. Colla, N. Jurik, Y. Liu, M. Delgado, M. Weissman, D.D. Viehland, and Z. Ye, " Kinetics and thermodynamics of the ferroelectric transitions in PbMg$_{1/3}$Nb$_{2/3}$O$_3$ and PbMg$_{1/3}$Nb$_{2/3}$O$_3$-12% PbTiO$_3$ crystals," Journal of Applied Physics 113, 184104 (2013.)

[106] E. V. Colla, D. Vigil, J. Timmerwilke, M.B. Weissman, D.D. Viehland, and B. Dkhil, "Stability of glassy and ferroelectric states in the relaxors PbMg$_{1/3}$Nb$_{2/3}$O$_3$ and PbMg$_{1/3}$Nb$_{2/3}$O$_3$ -12% PbTiO$_3$," Phys. Rev. B - Condens. Matter Mater. Phys., **75**, [21], 1–6, (2007).

[107] S. Hashemizadeh and D. Damjanovic, "Nonlinear dynamics of polar regions in paraelectric phase of (Ba$_{1-x}$,Sr$_x$)TiO$_3$ ceramics," Appl. Phys. Lett., **110**, [19], 192905, (2017).

[108] R. Pirc, R. Blinc, and Z. Kutnjak, "Nonlinear dielectric response of relaxor ferroelectrics," Phys. Rev. B, **65**, 1–7, (2002).

[109] S.S.N. Bharadwaja, E. Hong, S.J. Zhang, L.E. Cross, and S. Trolier-McKinstry, "Nonlinear dielectric response in (1−x)Pb(Zn$_{1/3}$Nb$_{2/3}$)O$_3$-xPbTiO$_3$ (x=0.045 and 0.08) single crystals," J. Appl. Phys., **101**, [10], 104102, (2007).

[110] J. Dec, W. Kleemann, S. Miga, C. Filipic, A. Levstik, R. Pirc, T. Granzow, and R.

Pankrath, "Probing polar nanoregions in $Sr_{0.61} Ba_{0.39} Nb_2 O_6$ via second-harmonic dielectric response," Phys. Rev. B, 3–6, (2003).

[111] K. Lefki and G.J.M. Dormans, "Measurement of piezoelectric coefficients of ferroelectric thin films," J. Appl. Phys., **76**, [3], 1764, (1994).

[112] A.L. Kholkin, C. Wütchrich, D. V. Taylor, and N. Setter, "Interferometric measurements of electric field-induced displacements in piezoelectric thin films," Rev. Sci. Instrum., **67**, [5], 1935, (1996).

[113] L. Chen, J.-H. Li, J. Slutsker, J. Ouyang, and A. Roytburd, "Contribution of substrate to converse piezoelectric response of constrained thin films," J. Mater. Res., **19**, [10], 2853–2858, (2011).

[114] S. Lepadatu, M. Stewart, and M.G. Cain, "Quantification of electromechanical coupling measured with piezoresponse force microscopy," J. Appl. Phys., **116**, [6], 066806, (2014).

[115] M. Stewart, S. Lepadatu, L.N. McCartney, M.G. Cain, L. Wright, J. Crain, D.M. Newns, and G.J. Martyna, "Electrode size and boundary condition independent measurement of the effective piezoelectric coefficient of thin films," APL Mater., **3**, [2], 026103, (2015).

[116] S. Sivaramakrishnan, P. Mardilovich, A. Mason, A. Roelofs, T. Schmitz-Kempen, and S. Tiedke, "Electrode size dependence of piezoelectric response of lead zirconate titanate thin films measured by double beam laser interferometry," Appl. Phys. Lett., **103**, [13], 132904, (2013).

[117] P. Gerber, A. Roelofs, C. Kügeler, U. Böttger, R. Waser, and K. Prume, "Effects of the top-electrode size on the piezoelectric properties (d_{33} and S) of lead zirconate titanate thin films," J. Appl. Phys., **96**, [5], 2800, (2004).

[118] Q.M. Zhang, W.Y. Pan, and L.E. Cross, "Laser interferometer for the study of piezoelectric and electrostrictive strains," J. Appl. Phys., **63**, [8], 2492, (1988).

[119] J.E. Graebner, B.P. Barber, P.L. Gammel, D.S. Greywall, and S. Gopani, "Dynamic visualization of subangstrom high-frequency surface vibrations," Appl. Phys. Lett., **78**, [2], 159, (2001).

[120] W.Y. Pan and L.E. Cross, "A sensitive double beam laser interferometer for studying high-frequency piezoelectric and electrostrictive strains," Rev. Sci. Instrum., **60**, [8], 2701, (1989).

[121] J.-F. Li, P. Moses, and D. Viehland, "Simple, high-resolution interferometer for the measurement of frequency-dependent complex piezoelectric responses in ferroelectric ceramics," Rev. Sci. Instrum., **66**, [1], 215, (1995).

[122] Z. Huang and R.W. Whatmore, "A double-beam common path laser interferometer for the measurement of electric field-induced strains of piezoelectric thin films," Rev. Sci. Instrum., **76**, [12], 123906, (2005).

[123] M.G. Cain, M. Stewart, and M. Downs, in *NSTI-Nanotech* (2006), pp. 670–673.

[124] C. Chao, Z. Wang, W. Zhu, and O. Tan, "Scanning homodyne interferometer for characterization of piezoelectric films and microelectromechanical systems devices," Rev. Sci. Instrum., **76**, [6], 063906, (2005).

[125] Z. Huang, Q. Zhang, S. Corkovic, R. Dorey, F. Duval, G. Leighton, R. Wright, P. Kirby, and R.W. Whatmore, "Piezoelectric PZT films for MEMS and their characterization by interferometry," J. Electroceramics, **17**, [2–4], 549–556, (2006).

[126] R. Herdier, D. Jenkins, E. Dogheche, D. Rèmiens, and M. Sulc, "Laser Doppler vibrometry for evaluating the piezoelectric coefficient d_{33} on thin film," Rev. Sci. Instrum., **77**, [9], 093905, (2006).

[127] A. Kholkin, S. Kalinin, A. Roelofs, and A. Gruverman, in *Scanning Probe Microsc. Electr. Electromechanical Phenom. Nanoscale* (Springer Science+Business Media, New York, 2007).

[128] O. Kuffer, I. Maggio-Aprile, J.-M. Triscone, O. Fischer, and C. Renner, "Piezoelectric response of epitaxial $Pb(Zr_{0.2}Ti_{0.8})O_3$ films measured by scanning tunneling microscopy," Appl. Phys. Lett., **77**, [11], 1701, (2000).

[129] F. Xu, F. Chu, and S. Trolier-McKinstry, "Longitudinal piezoelectric coefficient measurement for bulk ceramics and thin films using pneumatic pressure rig," J. Appl. Phys., **86**, [1], 588, (1999).

[130] J. Lazar, O. Číp, M. Čížek, J. Hrabina, and Z. Buchta, "Suppression of air refractive index variations in high-resolution interferometry.," Sensors, **11**, [8], 7644–55, (2011).

[131] G. Peggs and A. Yacoot, "A review of recent work in sub-nanometre displacement measurement using optical and X-ray interferometry," Phil. Trans. R. Soc. Lond. A, **360**, 953–968, (2002).

[132] T. Jungk, Á. Hoffmann, and E. Soergel, "Influence of the inhomogeneous field at the tip on quantitative piezoresponse force microscopy," Appl. Phys. A, **86**, [3], 353–355, (2006).

[133] T. Jungk, Á. Hoffmann, and E. Soergel, "Challenges for the determination of piezoelectric constants with piezoresponse force microscopy," Appl. Phys. Lett., **91**, [2007], 8–11, (2007).

[134] S. Kalinin, A. Rar, and S. Jesse, "A decade of piezoresponse force microscopy: progress, challenges, and opportunities," IEEE Trans. Ultrason. Ferroelectr. Freq. Control, **53**, [12], 2226–2252, (2006).

[135] G. Zavala, J.H. Fendler, and S. TrolierMcKinstry, "Characterization of ferroelectric lead zirconate titanate films by scanning force microscopy," J. Appl. Phys., **81**, [11], 7480–7491, (1997).

[136] E. Soergel, "Piezoresponse force microscopy (PFM)," J. Phys. D. Appl. Phys., **44**, [46], 464003, (2011).

[137] S. Jesse, A.P. Baddorf, and S. V Kalinin, "Dynamic behaviour in piezoresponse force

microscopy," Nanotechnology, **17**, [6], 1615–1628, (2006).

138 S. Jesse, A. Kumar, S. V Kalinin, A. Gannepali, and R. Proksch, "Band excitation scanning probe microscopies : traveling through the Fourier Space," **Asylum Res**, [Application note 16], 2–5, (2010).

139 F. Mammano and J.F. Ashmore, "A laser interferometer for sub-nanometre measurements in the cochlea," J. Neurosci. Methods, **60**, [1–2], 89–94, (1995).

140 L. Deck and P. de Groot, "High-speed noncontact profiler based on scanning white-light interferometry.," Appl. Opt., **33**, [31], 7334–8, (1994).

141 A. Safari and E.K. Akdogan, editors , *Piezoelectric Transducers and Acoustic Materials for Transducer Applications* (Springer Science+Business Media, 2007).

142 R.L. Johnson-wilke, R.H.T. Wilke, M. Wallace, A. Rajashekhar, G. Esteves, Z. Merritt, J.L. Jones, and S. Trolier-mckinstry, "Ferroelectric / Ferroelastic domain wall motion in dense and porous tetragonal lead zirconate titanate films," IEEE Trans. Ultrason. Ferroelectr. Freq. Control, **62**, [1], 46–55, (2015).

143 F. Chu, F. Xu, J. Shepard, and S. Trolier-McKinstry, in *Mater. Res. Soc. Symp. Proc. 493,* (1998), pp. 409–414.

144 S.H. Baek, J. Park, D.M. Kim, V. Aksyuk, R.R. Das, S.D. Bu, D. Felker, J. Lettieri, V. Vaithyanathan, S.S.N. Bharadwaja, N. Bassiri-Gharb, Y.B. Chen, H.P. Sun, C.M. Folkman, H.W. Jang, D.J. Kreft, S.K. Streiffer, R. Ramesh, X.Q. Pan, S. Trolier-McKinstry, D.G. Schlom, M.S. Rzchowski, R.H. Blick, and C.B. Eom, "Giant piezoelectricity on Si for hyperactive MEMS.," Science, **334**, [6058], 958–61, (2011).

145 R. Keech, L. Ye, J.L. Bosse, G. Esteves, J. Guerrier, J.L. Jones, M.A. Kuroda, B.D. Huey, and S. Trolier-McKinstry, "Declamped piezoelectric coefficients in patterned 70/30 lead magnesium niobate–lead titanate thin films," Adv. Funct. Mater., **27**, [9], (2017).

146 M. Wallace, R. Johnson-Wilke, G. Esteves, C. Fancher, R. Wilke, J. Jones, and S.

Trolier-McKinstry, "In situ measurement of increased ferreoelectric/ferroelastic domain wall motion in declamped tetragonal lead zirconate titanate thin films," To be published, (2015).

[147] F. Griggio, S. Jesse, a. Kumar, O. Ovchinnikov, H. Kim, T.N. Jackson, D. Damjanovic, S. V. Kalinin, and S. Trolier-McKinstry, "Substrate Clamping Effects on Irreversible Domain Wall Dynamics in Lead Zirconate Titanate Thin Films," Phys. Rev. Lett., **108**, [15], 157604, (2012).

[148] P. Zubko, G. Catalan, and A.K. Tagantsev, "Flexoelectric effect in solids," Annu. Rev. Mater. Res., **43**, [1], 387–421, (2013).

[149] W. Ma and L.E. Cross, "Flexoelectric polarization of barium strontium titanate in the paraelectric state," Appl. Phys. Lett., **81**, [18], 3440–3442, (2002).

[150] W. Ma and L.E. Cross, "Large flexoelectric polarization in ceramic lead magnesium niobate," Appl. Phys. Lett., **79**, [26], 4420, (2001).

[151] J.Y. Fu, W. Zhu, N. Li, and L.E. Cross, "Experimental studies of the converse flexoelectric effect induced by inhomogeneous electric field in a barium strontium titanate composition," J. Appl. Phys., **100**, [2006], 024112, (2006).

[152] J. Narvaez and G. Catalan, "Origin of the enhanced flexoelectricity of relaxor ferroelectrics," Appl. Phys. Lett., **104**, [16], 162903, (2014).

[153] L.M. Garten and S. Trolier-McKinstry, "Enhanced flexoelectricity through residual ferroelectricity in barium strontium titanate," J. Appl. Phys., **117**, [9], 094102, (2015).

[154] A. Biancoli, C.M. Fancher, J.L. Jones, and D. Damjanovic, "Breaking of macroscopic centric symmetry in paraelectric phases of ferroelectric materials and implications for flexoelectricity," Nat. Mater., **14**, [2], 224–229, (2014).

[155] J.Y. Fu, W. Zhu, N. Li, and L.E. Cross, "Experimental studies of the converse flexoelectric effect induced by inhomogeneous electric field in a barium strontium titanate composition," J. Appl. Phys., **100**, [2], 024112, (2006).

[156] J.Y. Fu and L.E. Cross, "Separate control of direct and converse piezoelectric effects in flexoelectric piezoelectric composites," Appl. Phys. Lett., **91**, [2007], 89–92, (2007).

[157] S. Baskaran, S. Thiruvannamalai, H. Heo, H.J. Lee, S.M. Francis, N. Ramachandran, and J.Y. Fu, "Converse piezoelectric responses in nonpiezoelectric materials implemented via asymmetric configurations of electrodes," J. Appl. Phys., **108**, [6], 064116, (2010).

[158] L. Shu, W. Huang, S. Ryung Kwon, Z. Wang, F. Li, X. Wei, S. Zhang, M. Lanagan, X. Yao, and X. Jiang, "Converse flexoelectric coefficient f_{1212} in bulk $Ba_{0.67}Sr_{0.33}TiO_3$," Appl. Phys. Lett., **104**, [23], 232902, (2014).

[159] S.B. Desu and H.M. O'Bryan, "Microwave Loss Quality of $BaZn_{1/3}Ta_{2/3}O_3$ Ceramics," J. Am. Ceram. Soc., **68**, [10], 546–551, (1985).

[160] P.K. Davies, J. Tong, and T. Negas, "Effect of Ordering-Induced Domain Boundaries on Low-Loss $Ba(Zn_{1/3}Ta_{2/3})O_3$-$BaZrO_3$ Perovskite Microwave Dielectrics," J. Am. Ceram. Soc., **80**, [7], 1727–1740, (1997).

[161] H. Hughes, D.M. Iddles, and I.M. Reaney, "Niobate-based microwave dielectrics suitable for third generation mobile phone base stations," Appl. Phys. Lett., **79**, [18], 2952–2954, (2001).

[162] A. Dias and R.L. Moreira, "Far-infrared spectroscopy in ordered and disordered $BaMg_{1/3}Nb_{2/3}O_3$ microwave ceramics," J. Appl. Phys., **94**, [5], 3414–3421, (2003).

[163] R.L. Moreira, F.M. Matinaga, and A. Dias, "Raman-spectroscopic evaluation of the long-range order in $Ba(B'_{1/3}B''_{2/3})O_3$ ceramics," Appl. Phys. Lett., **78**, [4], 428–430, (2001).

[164] B. Burton and E. Cockayne, "Why $Pb(B,B')O_3$ perovskites disorder at lower temperatures than $Ba(B,B')O_3$ perovskites," Phys. Rev. B, **60**, [18], R12542–R12545, (1999).

VITA

Smitha Shetty

Smitha Shetty was born in India on December 30, 1981. She got her undergraduate degree in Electrical Engineering from the University of Mumbai in India in 2003. She received two Master's degree in Electrical and Computer Engineering from University of South Florida (2005) and Carnegie Mellon University (2007). She spent four years in a start-up technology company working on the process development and characterization of pyroelectric FPGA infrared detectors. She decided to go back to school for her doctorate degree in Materials Science and Engineering in 2012 under the guidance of Prof. Susan Trolier-McKinstry. Dr. Shetty received her Ph.D. in Spring 2019.